Investigation of Countercurrent Helium-air Flows in Air-ingress Accidents for VHTRs

Reactor Concepts RD&D

Dr. Xiaodong Sun

The Ohio State University

In collaboration with:

Idaho National Laboratory

Madeline Feltus, Federal POC
Chang Oh, Technical POC

NEUP | Nuclear Energy
University Programs

U.S. Department of Energy

List of Tables

List of Figures

4

Project Objective:

The primary objective of this proposed research is to develop an extensive experimental database for the air-ingress phenomenon, which will help better understand the phenomenon as well as provide experimental data for the validation of computational fluid dynamics (CFD) analyses that are currently being performed at the collaborator's organization. This research is intended to be a separate-effects experimental study. However, a careful scaling analysis will first be performed prior to designing a scaled-down test facility in order to closely tie this research with the real application. The gas turbine-modular helium reactor (GT-MHR) 600 MWth developed by General Atomics, Inc. will be used as a reference design in this study. In the test matrix of the experiments, the temperature and pressure of the helium, and break size, location, shape, and orientation will be varied to simulate deferent scenarios and to identify potential mitigation strategies.

Background:

The project started on October 1, 2009. During the first quarter of the project, we began a scaling analysis for the air-ingress phenomenon under LOCA scenarios. We also initiated the process of collecting design information of the GT-MHR, including the geometry and dimensions of key components. A quality assurance plan was also being developed based upon the requirements.

Status:

Task 1.1: Perform the scaling study (Ohio State Responsible).

Task Status: Completed

Refer to Progress Report #5 for the details.

Task 1.2: Design the test facility (Ohio State Responsible)
Task Status: Completed

The details of the design are included in this report after this Status section.

Task 1.3: Develop quality assurance (QA) program (Ohio State Responsible)

Task Status: Completed

Task 1.4: Construct the test facilities

Task Status: The test facility design has been completed. We have contacted vendors and received quotations for the major test facility components. We are in the process of evaluating the quotations and acquiring major components.

Report (October 1, 2009 to September 30, 2013)

1. Small-scale experiments for better understanding density-driven flow

Air-Water Experiment

The air-ingress phenomena in a VHTR are very complex. We have therefore decided to perform some small-scale experiments prior to designing and constructing the actual test facility. Also considering that the hot duct break may take different sizes, shapes, and orientations in the actual applications, we are planning to investigate the effects of the different "break plate" and "break slits" on the air-ingress phenomena, as shown in

Figure 1. To closely examine the "break plate" and "break slits", a 1/30th reduced length scale model of GT-MHR demonstration setup was constructed. Figure 2 shows a schematic of the setup. This experiment is the first step to obtain a better understanding of flow patterns that could occur during a cross-vessel break accident. The reactor core was highly simplified. This set up can test the effects of different types of cross-vessel break and creep by changing the flange that houses the break plate or slit.

The set-up has a gas inlet at the top to inject gas to pressurize the facility if needed. The dimensions of scaled down set-up are listed in Table 1

Table 1. Dimensions of reactor prototype and scaled down set-up

	Prototype (m)	1/30 length scaled (in)	Available (in)
Vessel ID	7.2	9.449	9.5
Barrel OD	6.31	8.281	8.0
Cold Duct ID	2.29	3.005	3.0
Hot Duct ID	1.43	1.877	1.75
Vessel Height	23.7	38.88	38.88
Core Height + Lower Plenum	13.4	17.56	17.56
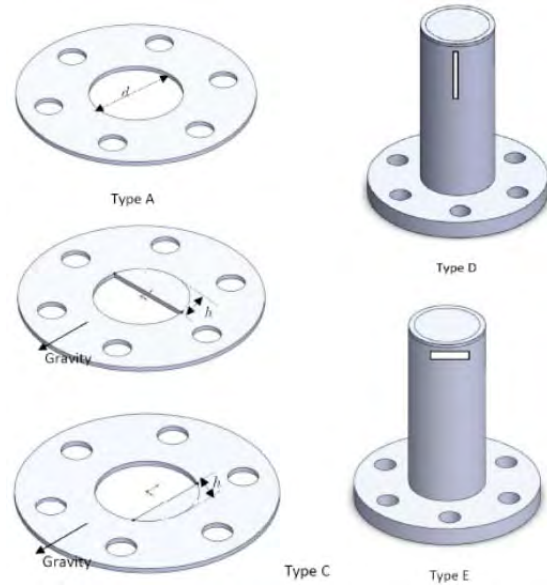
Figure 1. Schematic of different "break plates" and "break slits"

Air and water are used as working fluids. Figure 3 shows some high-speed video images when a double-ended guillotine break of the cross vessel is simulated. Figure 4 shows additional images when a Type D or Type E slit shown in Fig. 1 of 0.3" by 0.8" is used at different azimuthal location of the cross vessel. When the break location was rotated with 45° intervals, intermittent flow started for Type D slit at the 135 degree and Type E at the 45 degree. The speed of water ingress into the core vessel from the outside pipe break is slow and the water accumulated on the lower head, thus it might not cause serious problem to the lower plenum supporting columns.
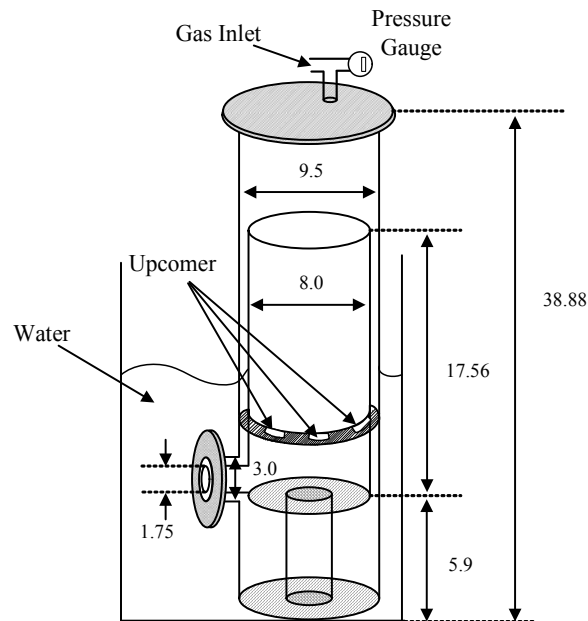
Figure 2. Scaled-down demonstration set-up
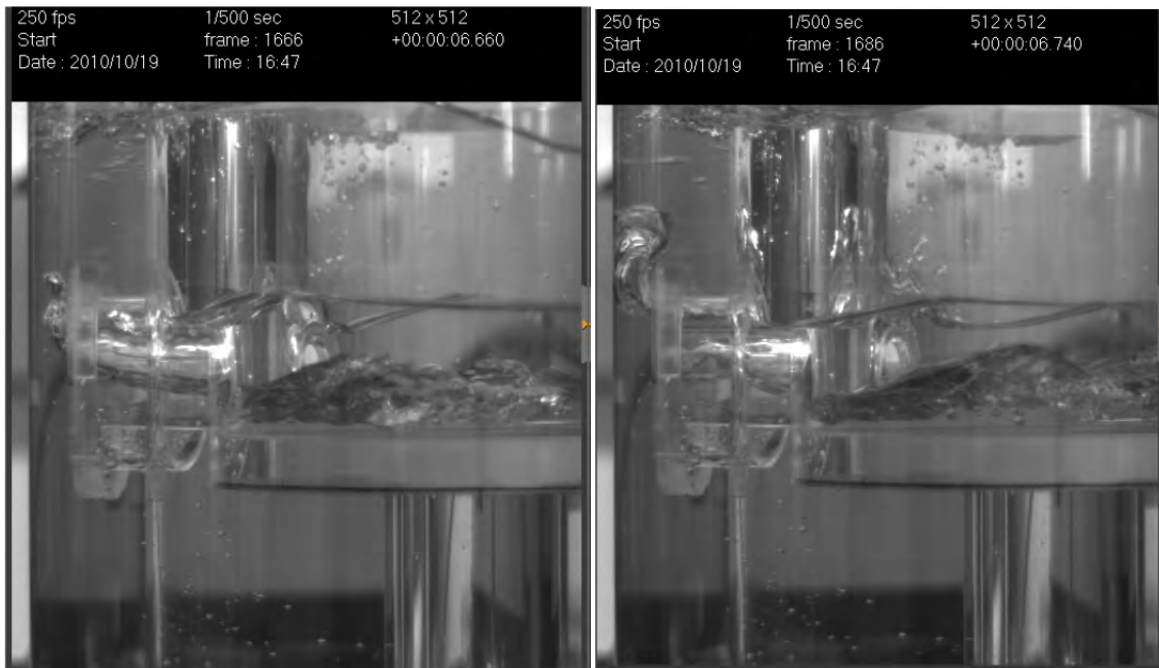
(a) 6.66 sec   (b) 6.74 sec

(c) 6.776 sec   (d) 6.938 sec

Figure 3. Images of the water "ingress" into the core using air and water as working fluids simulating the double-ended guillotine break of the cross vessel
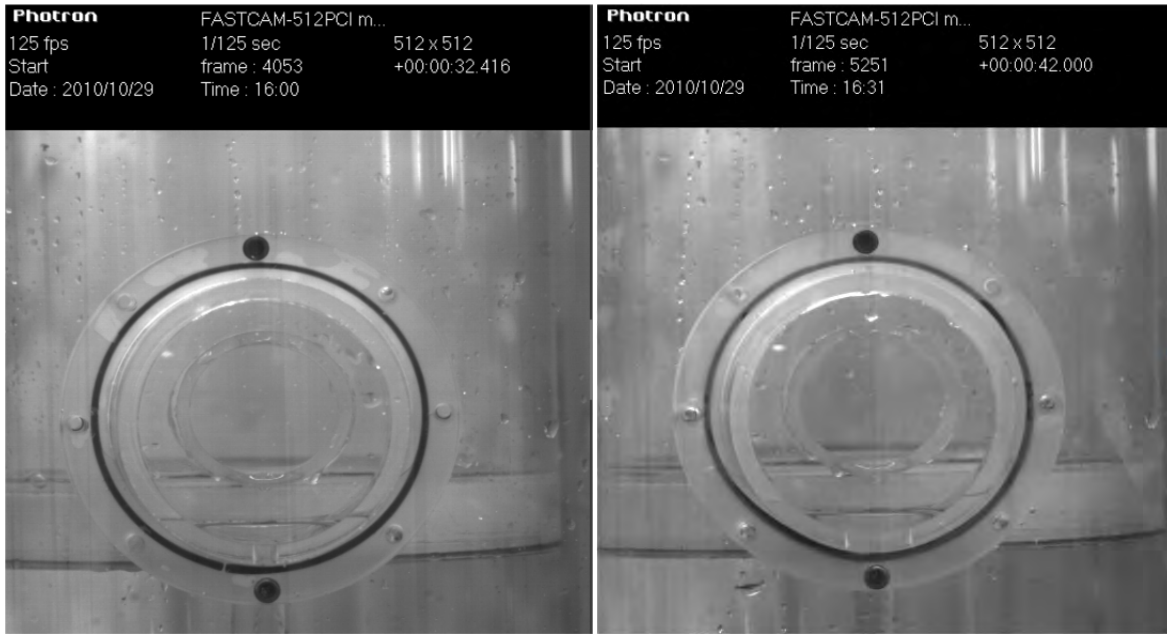
(a) Type D at 0° (bottom)   (b) Type E at 0° (bottom)
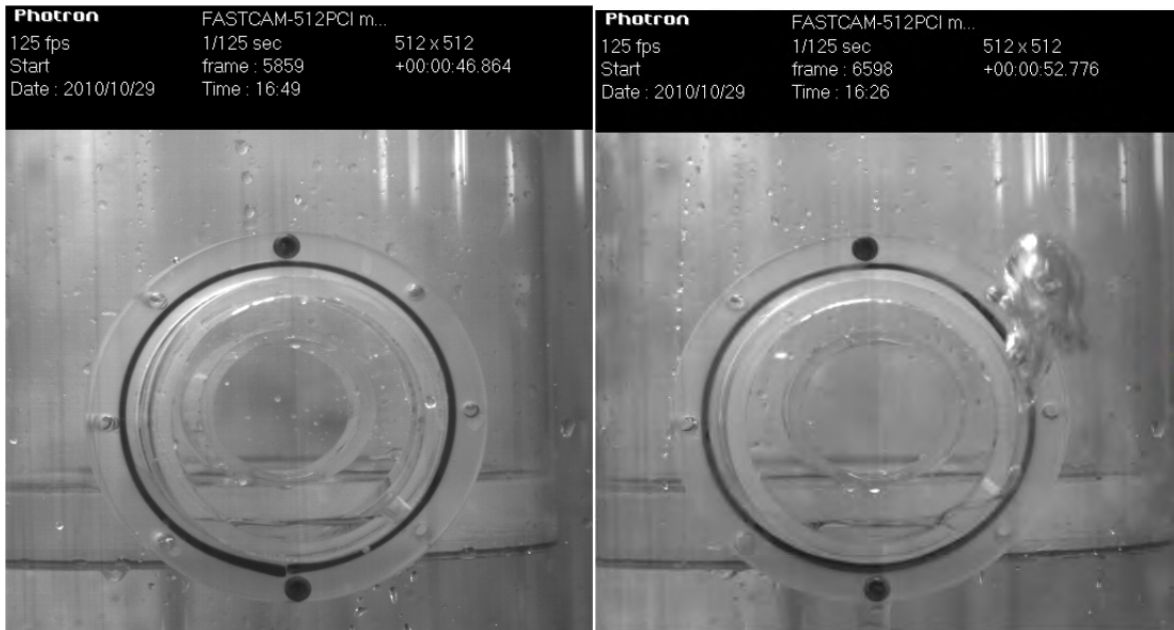
(c) Type D at 45°   (d) Type E at 45°

Figure 4. Images of the water "ingress" into the core using air and water as working fluids simulating a small break on the cross-vessel wall
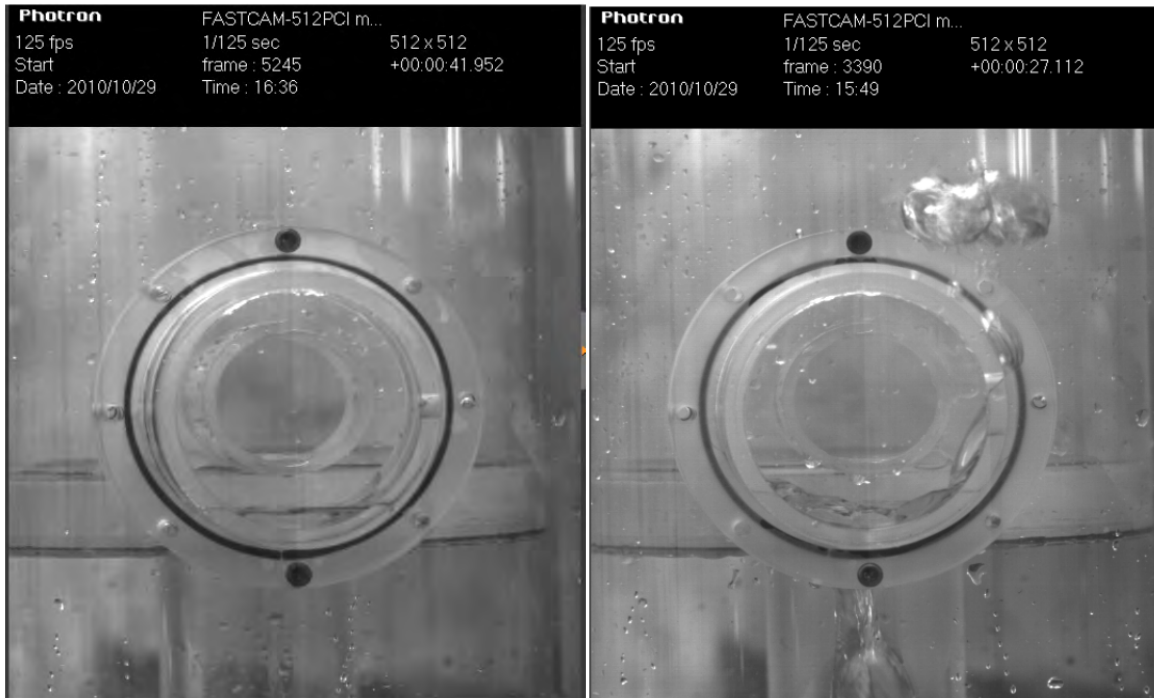
(e) Type D at 90°   (f) Type E at 90°
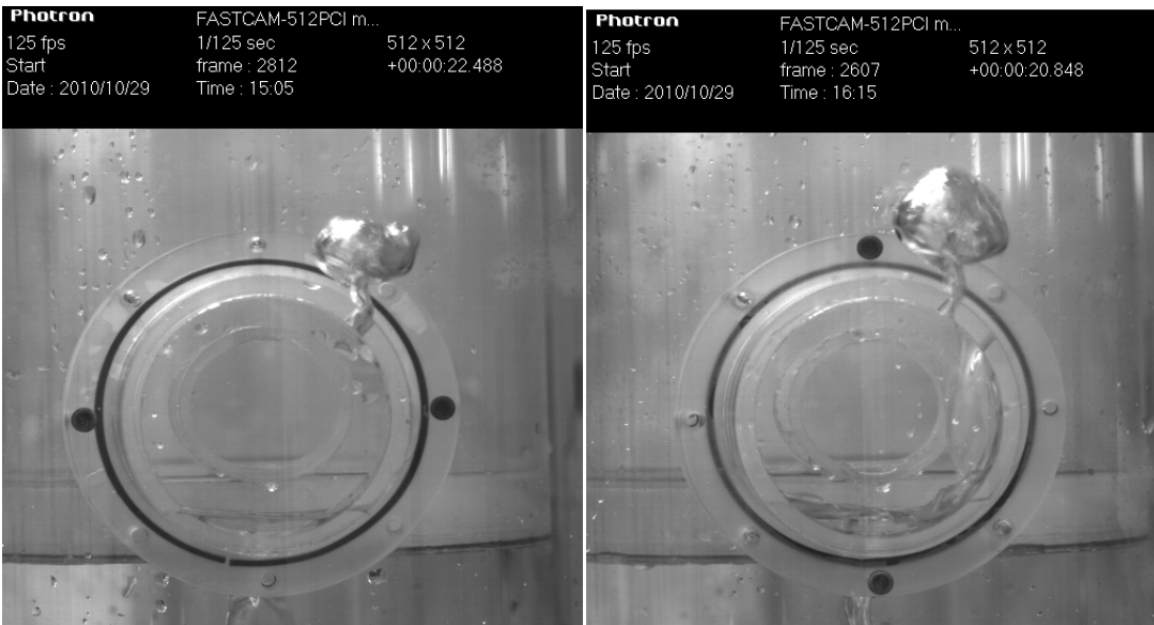
(g) Type D at 135°   (h) Type E at 135°

Figure 4. Images of the water "ingress" into the core using air and water as working fluids simulating a small break on the cross-vessel wall (Continued)
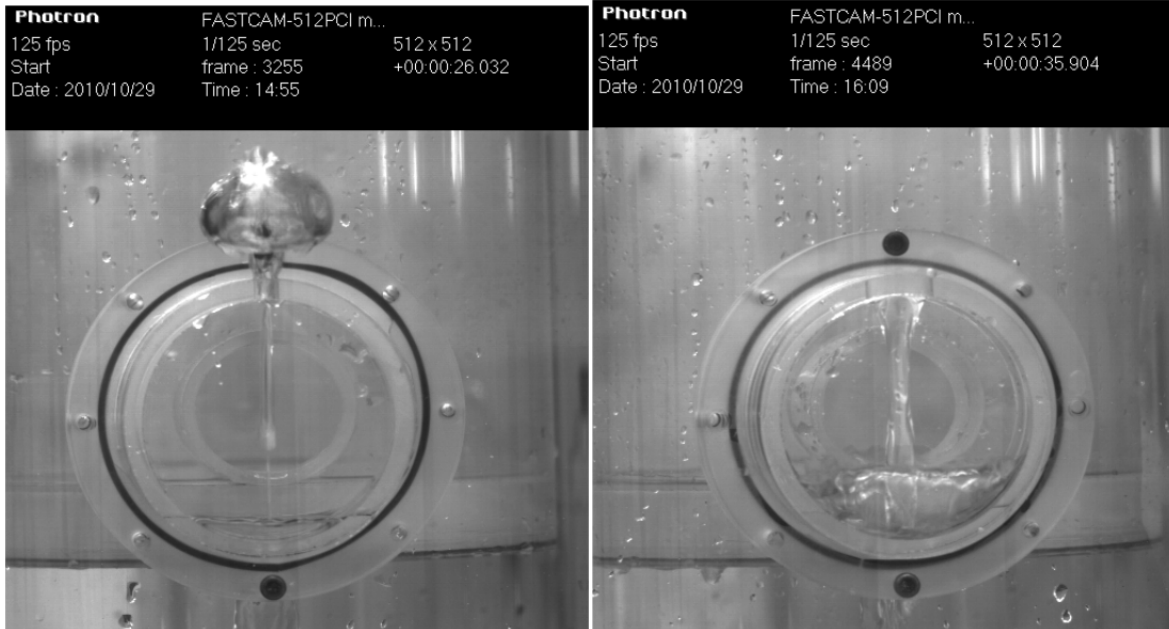
(i) Type D at 180°   (j) Type E at 180°

Figure 4. Images of the water "ingress" into the core using air and water as working fluids simulating a small break on the cross-vessel wall (Continued)

In addition, an experiment was performed to simulate a double-ended guillotine break on the hot-duct. This is to show the counter-current flow after the helium has left the lower core plenum. A candle was placed in the middle of the inner tube (simulating the core) and smoke from the candle was used to see the air circulation direction. It was found out that the smoke (hot air) leaked out through the top portion of the break pipe and the outside cold air enters into the inner vessel through the bottom portion of the break pipe. This indeed qualitatively confirms the natural circulation cycle from the break to the lower plenum and to the break again, which is consistent with the findings by one of the co-PIs, Dr. Chang Oh of INL[1,2]

Figure 5. Image of the air flows when a heat source is placed near the lower plenum (view from the outside of the double-ended guillotine break plane)

Air-Helium Experiment

For the better understanding of the density-driven flow and the feasibility test of applying a Particle Imaging Velocimetry (PIV) system to the future OSU high-temperature air-ingress test facility, air-helium experiments were performed for flow visualization using a Planar Laser-Induced Fluorescence (PLIF) or PIV system. In the experiments, helium gas with seeding particles was used to fill the experimental apparatus. The seeding particles (vegetable oil) were generated with an aerosol generator with a mean size of about 1 micrometer. The test facility components are shown in Figure 6.

The theoretical air ingress front velocity 0.46 m/s at the hot duct was calculated for the Reynolds number assumption with following equation 1[3,4,5].

$$U_F = \left[\frac{gh\left(\rho_{air} - \rho_{He}\right)}{\rho_{air} + \rho_{He}} \right]^{1/2}$$
[1]
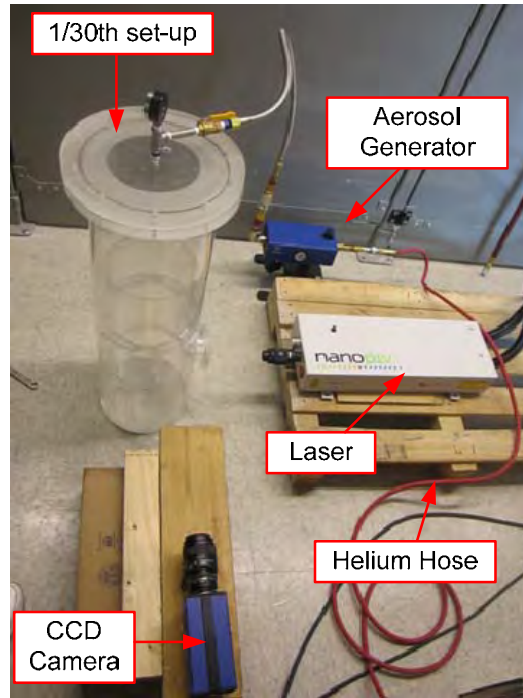
Figure 6. Test facility components

(a) Pipe outlet

(b) Lower plenum and cross pipe
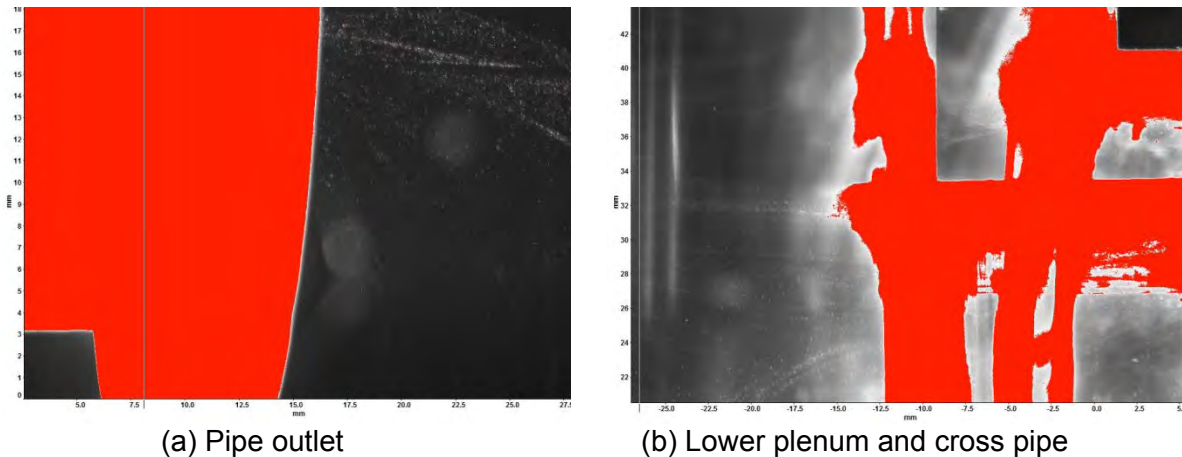
Figure 7. Aerosol particle measurement with PIV system

Figure 7 shows the results of the particle measurement with the PIV system. In the figure, the test set-up regions were appeared red and could not measure the aerosol particles effectively in the cross pipe regions. This is due to the reflections of laser from the curvature and transparency of acrylic pipes. From this measurement, air-ingress velocity was not measured with the acrylic pipe. However, particles are measured at the outside pipe and low curvature region. These results give confidence that the PIV system could be applied to the OSU high-temperature air-ingress test facility, which uses plat quartz windows and metallic pipes. Therefore, instead of using particle measurements to measure density driven flow, simple shadowography was used for the velocity measurement for the better understanding of density driven flow.
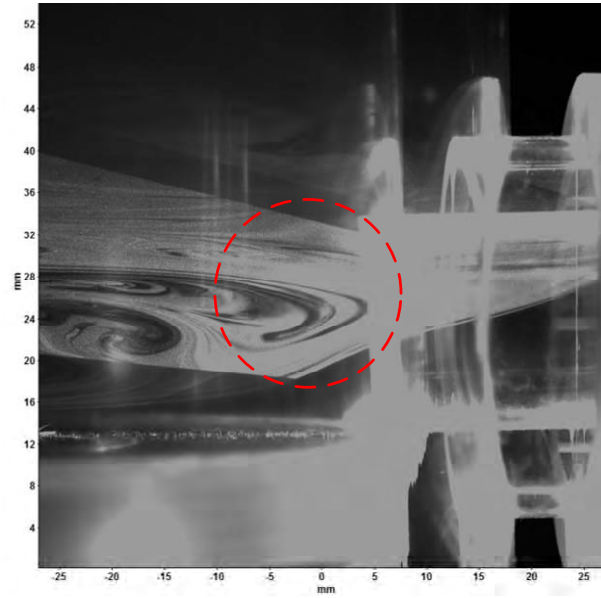
Figure 8. Helium and aerosol cloud movement at the lower plenum
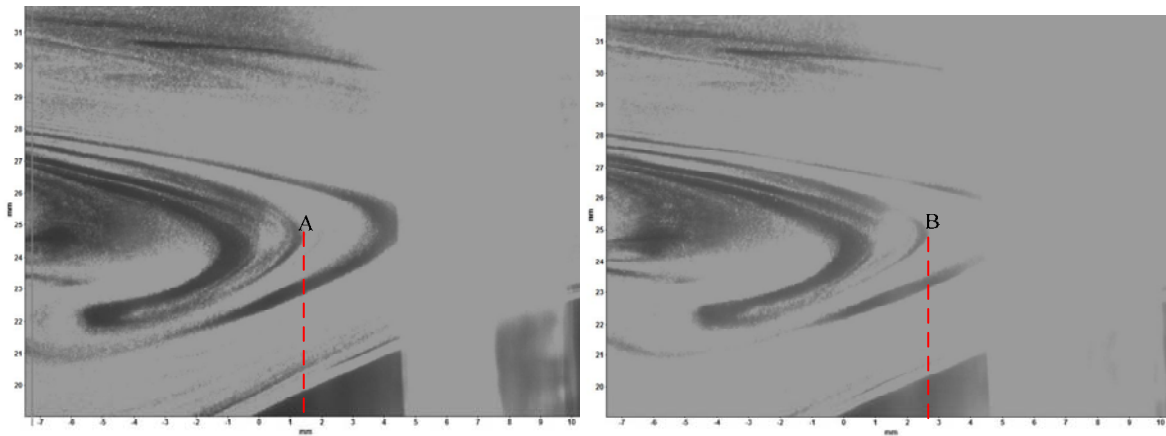
Figure 9. Displacement of Helium (seeding particles) in 3 milliseconds

Figure 8 shows the aerosol clouds with the PIV system, while Figure 9 shows the displacement between points A and B is the 1.3 mm over a time period of 3 milliseconds. From this experiment, the helium gas flow velocity is measured to be 0.433 m/s. This is in good agreement with the air ingress velocity from Benjamin's theory.

Computational fluid dynamics (CFD) calculations for a density driven flow were used to benchmark the experiment. The five segments used for the OSU scaling analysis for the hot duct-hot exit plenum is shown in Figure 10. Due to the limited time and resources, calculation was focused on the zone 1.
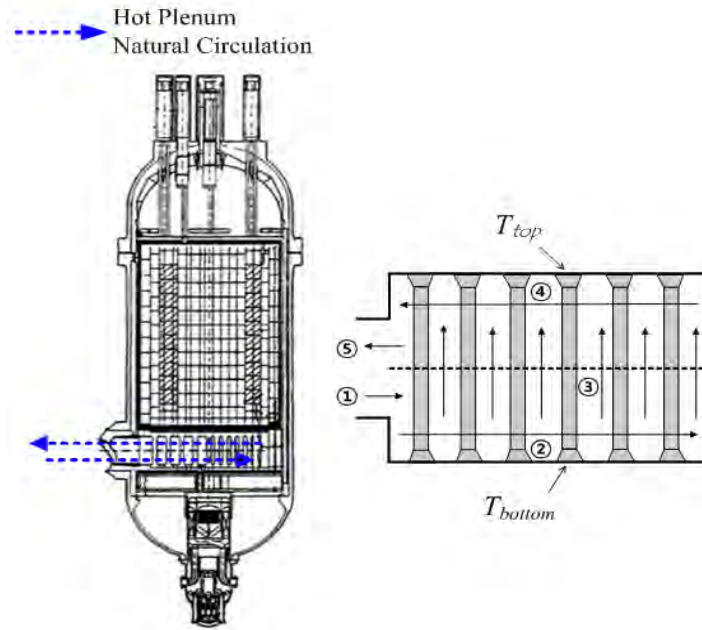
Figure 10. Ingress to hot plenum (blue) and enlarged view of hot duct-hot plenum system
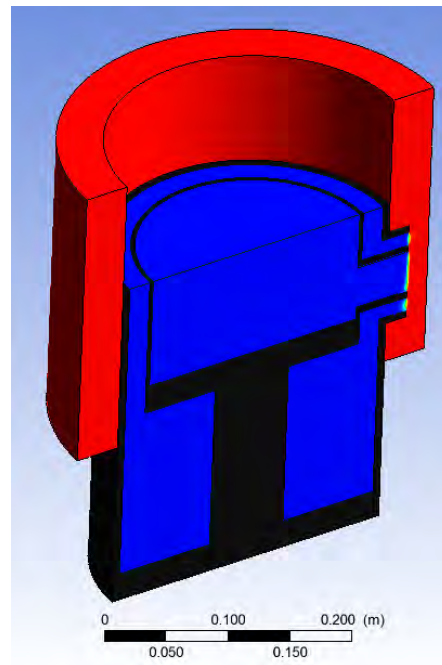
Figure 11. Geometry of CFD model

Figure 11 shows the geometry of the CFD model. The outside of the red region is air and inside blue is filled with helium at the initial state. From the previous calculations, this part does not considerably affect the density driven flow into the lower plenum top part of the set-up, and lower part of air were removed from this calculation to reduce the computational time.
The Fluent specification and model used in this calculation are listed as follows:

- Solver
  - Solver : Pressure-Based
  - Time : Transient
  - Pressure Velocity coupling: PISO
  - Transient Formulation : First Order Implicit

- Discretization
  - Pressure : PRESTO!
  - Momentum : 2nd order upwind
  - Species : 2nd order upwind
  - Energy : 2nd order upwind

- Laminar flow

- Species transport model
  - Mixture material: Mixturetemplate
  - 2 species: Air and Helium
  - Density : Ideal-gas
  - Specific heat : mixing-law
  - Thermal conductivity : Ideal-gas-mixing-law
  - Viscosity : Ideal-gas-mixing-law
  - Mass Diffusivity : Kinetic theory

Figure 12 shows the air ingress through the pipe break. The results show good agrement that the density driven flow depth is about half of the channel depth. 90% of the air flows under the hot duct centerline.

Figure 13 shows the air mass fraction reaches a vaule of 0.9 in 0.2 second at the lower plenum enterance. The velocity from the CFD calculation is 0.31 m/s. This result is a little different from the PIV measument and the theoretical result. Therefore, further grid sensityvity study and physical model studies are required.
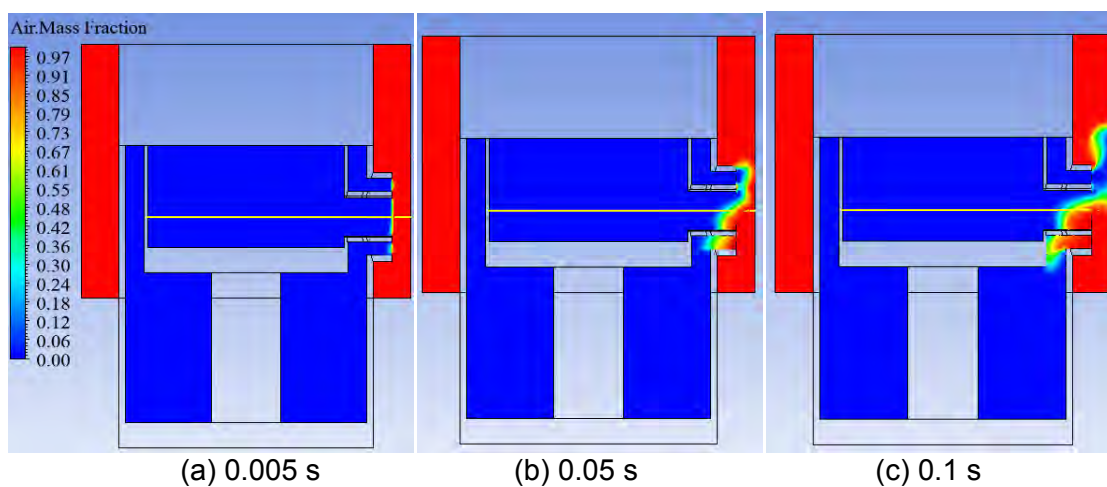
(a) 0.005 s   (b) 0.05 s   (c) 0.1 s

Figure 12. Fluent simulation for the density driven air-ingress

(d) 0.15 s   (e) 0.2 s

Centerline of hot duct
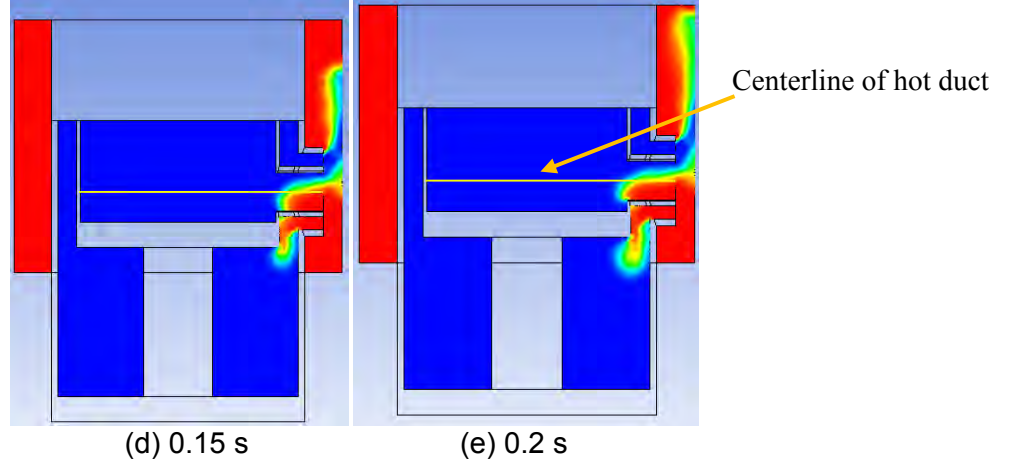
Figure 12. Fluent simulation for the density driven air-ingress (Continued)
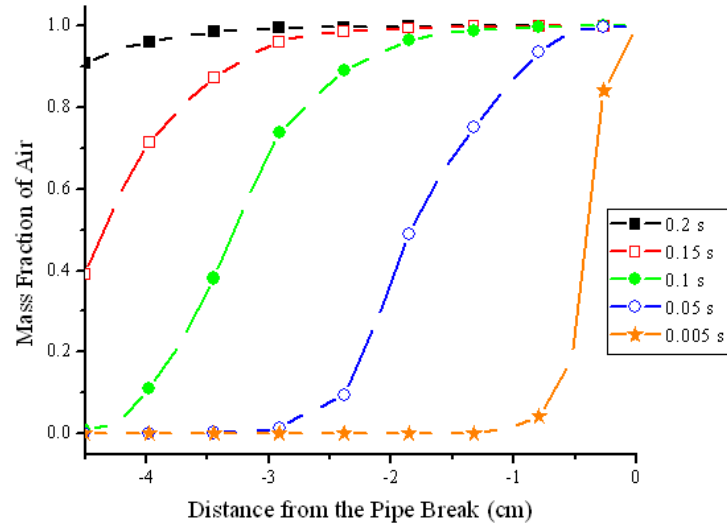
Figure 13. Mass fraction at the lower part of hot duct pipe

From the previous PIV experiment, velocity information is obtained. However, PIV system only can give the particle velocity information. Therefore, a PLIF system is required to calculate the air-ingress flow rate. PLIF technique provides two-dimensional distributions of a large range of flow field parameters. PLIF has been successfully used to measure gaseous and liquid species concentrations, velocities, densities, pressure, and temperature.

Acetone is used as the tracer molecule in this PLIF system. Acetone is advantageous for mixing measurements because of its linear relationship between the fluorescence intensity, vapor acetone concentration and laser power in an isobaric and isothermal environment. Equation 2 shows the overall fluorescence signal from acetone[6,8].

$$S_f = \frac{E}{hc/\lambda} \eta_{opt} dV_c \left[\frac{\chi_{acetone} P}{kT} \right] \sigma(\lambda, T) \phi(\lambda, T, P, \sum \chi_i)$$ [2]

21

E	Laser Fluence [J/cm^2]
hc/λ	Energy [J] of a photon at the excitation wavelength
η_{opt}	Overall efficiency of the collection optics
dVc	Collection volume [cm^3]
$\chi_{acetone}$	Mole fraction of acetone
P	Pressure
K	Boltzmann constant
T	Temperature
σ	Molecular absorption cross section of the tracer [cm^2]
Ø	Fluorescence quantum yield

It absorbs 255 ~320 nm wave length, and fluorescence 350 ~ 550 nm. The absorption peaks at 260-290 nm and the fluorescence peaks at 435 nm and 480 nm. The absorption spectrum and fluorescence spectrum do not overlap. Thus the incident laser can be filtered out easily and only excited light can be measured. The fluorescence frequencies are low-wavelength visible light that can be detected by a CCD camera. Figure 14 shows the dual pulsed Nd:YAG laser and Figure 15 shows the laser paths of 532nm and 266nm.

Figure 14. Nd:YAG Laser

a) 532 nm output
Output Energy 4~205 mJ

b) 266 nm output
Output Energy 0.5~384 mJ
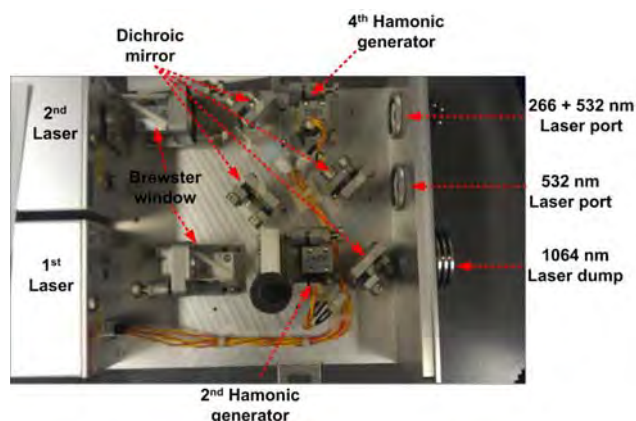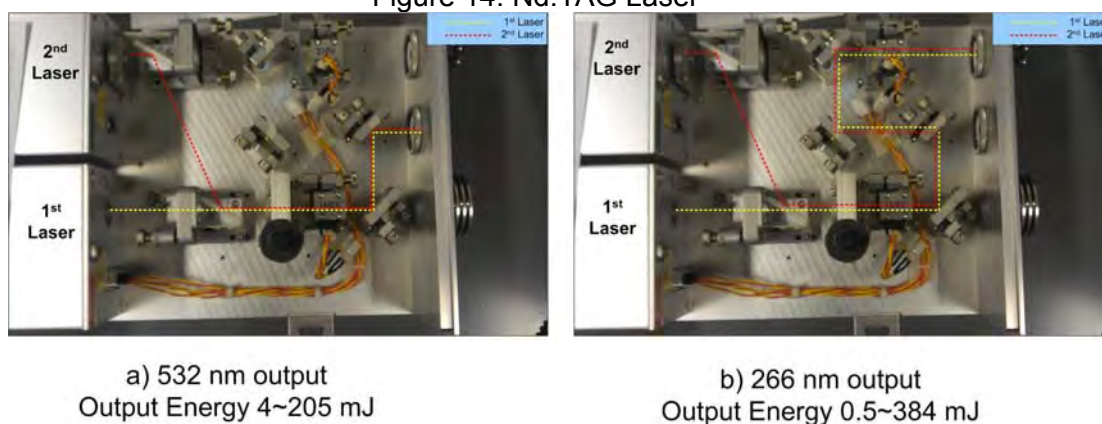
Figure 15. Harmonic generator configurations

First, the 1st and 2nd laser pass through the Brewster window. This window reflects some s-polarized light but no P-polarized light. S-polarized means perpendicular to the window and P-polarized is horizontal to the window as shown in the Figure 16. By aligning the 1st laser horizontally and 2nd laser vertically, both laser signals pass through the 2nd harmonic generator. The 2nd harmonic generator is used to convert the fundamental Nd:YAG wavelength of 1064 nm to the second harmonic at 532 nm. The dichromic mirror is specialized to efficiently reflect the desired frequency as shown in Figure 17. The dichromic mirror in our laser system only reflects 532 nm green lasers. Therefore, the dichromic mirrors are used to route the laser through the 4th harmonic generator to make 266 nm laser. The maximum output powers are 205 mJ for a 532nm output and 38.4 mJ for a 266nm output with a maximum frequency of 15 Hz.
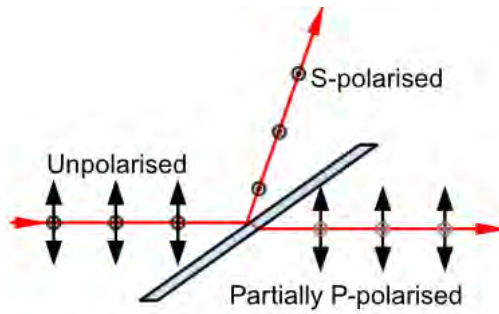
Figure 16. Brewster window
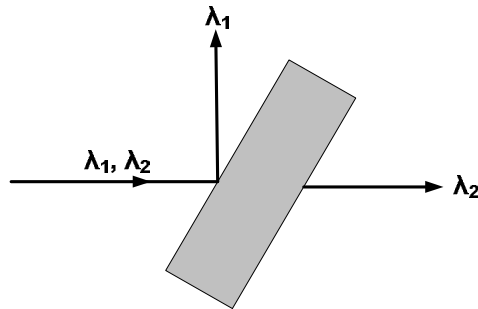
Figure 17. Dichromic Mirrors

We are planning to use the PIV method for the velocity measurements and PLIF for the air concentration measurements. PIV measures velocity by tracking the displacement of particles in two consecutive images, measurement errors will, therefore, be introduced due to the difference in densities between the fluid and seed particles. Using appropriate seeding particles will improve the quality of the data. We will use a PIV system with oil droplets acting as the seeding particles for low-temperature tests and titanium dioxide particles for high-temperature tests. The variable that indicates how fast the particles respond to the change of the fluid condition is relaxation time, which is defined by Eq. (3). It is related to the diameter (d) and density of the particles (ρ) and the fluid dynamic viscosity (μ). The relaxation time of the 1-μm diameter oil droplets and 20-nm diameter titanium dioxide particles are 2.39E-6 and 0.028E-10 second, respectively. Smaller relaxation time means quicker response to the fluid motion.

$$\tau = \frac{\rho d^2}{18\mu} \qquad\qquad [3]$$

The titanium dioxide particles have faster response time and would be stable in high-temperature test environments, but are carcinogenic to humans through inhalation. Therefore, special attention is needed to safely and properly use titanium dioxide particles.

We are planning to use PLIF with acetone acting as the seeding particle to make concentration measurements. Acetone absorbs 266-nm laser and has peak emissions at 435 and 480 nm wavelength. As shown in Figure 18, fused silica has a better transmittance than quartz almost over the entire light wavelength region. Fused silica has an almost 100% transmittance for 532-nm wavelength light (for PIV), 266-nm laser sheet, and 350~550-nm fluorescent signal from acetone for PLIF. In our experiments, commercial grade fused quartz will be used, which has an over 90% transmittance.

For the velocity measurements using PIV, the light intensity in the images is not critical. So, the optical distortion, due to the use of quartz, does not affect the velocity measurement. For the concentration measurements using PLIF, we are planning to perform a calibration for the quartz window by using a quartz cuvette filling with acetone droplets.

In addition, we are measuring the acetone fluorescence signal. Therefore, the 266 nm should be blocked with a filter. The transmittance curve of the fluorescence signal band pass filter is shown in Figure 19. It blocks 266 nm laser signals effectively; however, it blocks the 489 nm fluorescence peak as well. Because our measurement is under transient conditions, each flow measurement has to be analyzed with one laser shot. Thus, an external signal intensifier is used.
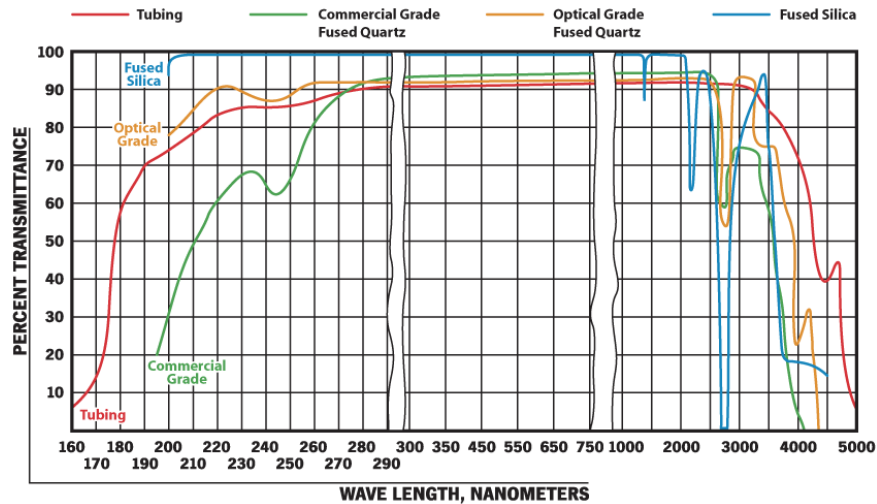
Figure 18. Transmittance curve of window material
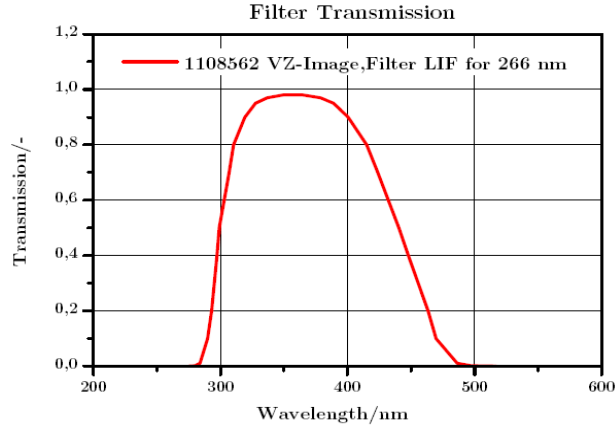
Figure 19. Transmittance curve of LIF filter for 266nm laser

From Eq. (2), the fluorescence signal at constant pressure and constant temperature, the fluorescence signal is proportional to acetone concentration. The linearity of fluorescence from the laser energy per unit mole fraction at atmospheric pressure, normalized to the room-temperature value can be shown is the Figure 20. Thus, PLIF system can be applied for the isothermal and isobaric air ingress test. However, more research is required in order to apply it to a high temperature, high pressure experiment.
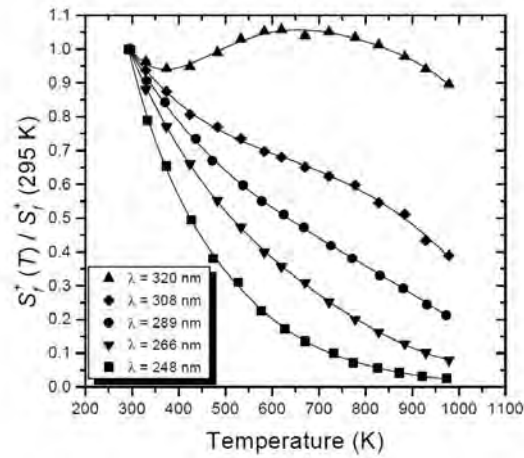
Figure 20. Temperature dependence per laser energy of acetone fluorescence

2. Scaling Analysis on Reactor System[9]

From the continuity equation, the mass flow rate at every cross-section for the ith segment along the loop is constant in Figure 10. Mathematically, we have equation 4

$$\dot{m} = \dot{m}_i \qquad [4]$$

where $\dot{m}$ is the mass flow rate and $\dot{m}_i$ is the mass flow rate in the ith segment. The integrated loop momentum equation is written as follows:

$$\frac{d\dot{m}}{dt}\sum_i \frac{l_i}{a_i} = (\rho_C - \rho_H)gH - \frac{\dot{m}^2}{\rho_r a_r^2}\sum_i \frac{1}{2}(\frac{fl}{d_h} + K)_i (\frac{a_r}{a_i})^2 \qquad [5]$$

where l_i and a_i are the length and the cross-sectional area of the ith segment, respectively. ρ_c, ρ_H and g are the cold-side density, the hot-side density and the acceleration due to gravity, respectively. H, ρ_r and a_r are the vertical distance between the thermal centers of the hot and cold side, the density of the reference segment and the cross-sectional area of the reference segment, respectively. f, d_h and K are Darcy friction factor, the hydraulic diameter and the minor loss coefficient of the ith segment, respectively.

The loop momentum equation can be made dimensionless by normalizing the terms relative to their initial conditions or boundary conditions. This is denoted by the subscript "o". That is,

$$\dot{m}^+ = \frac{\dot{m}}{\dot{m}_o} = \frac{\dot{m}}{\rho_r a_r w_o} \qquad [6]$$

$$\rho_H^+ = \frac{\rho_H}{(\rho_C - \rho_H)_o} \qquad [7]$$

$$\rho_C^+ = \frac{\rho_C}{(\rho_C - \rho_H)_o} \qquad [8]$$

$$\left[\sum_i \frac{1}{2}(\frac{fl}{d_h} + K)_i (\frac{a_r}{a_i})^2\right]^+ = \frac{\sum_i \frac{1}{2}(\frac{fl}{d_h} + K)_i (\frac{a_r}{a_i})^2}{\left[\sum_i \frac{1}{2}(\frac{fl}{d_h} + K)_i (\frac{a_r}{a_i})^2\right]_o} \qquad [9]$$

Substituting these ratios into the governing equation yields the following dimensionless equation:

$$\frac{d\dot{m}^+}{dt^+} = \Pi_L \left[\frac{(\rho_C^+ - \rho_H^+)H^+}{\Pi_{Fr}} - (\dot{m}^+)^2 \Pi_F \left[\sum_i \frac{1}{2}(\frac{fl}{d_h} + K)_i (\frac{a_r}{a_i})^2 \right]^+ \right]$$ [10]

$$H^+ = \frac{H}{H_o}$$ [11]

The non-dimensional equation time scale is as follows:

$$t^+ = \frac{t}{\tau} = \frac{tw_o}{H_o}$$ [12]

where, w_o and H_o are the velocity of the reference section at the onset of natural circulation and the geometric height of the reference section, respectively. The non-dimensional groups are defined wherein the length or geometric scale, the non-dimensional Froude number and the friction number are given as follows:

$$\Pi_L = \frac{H_o}{a_r \sum_i \frac{l_i}{a_i}}$$ [13]

$$\Pi_{Fr} = \frac{\rho_r w_o^2}{(\rho_C - \rho_H)_o g H_o}$$ [14]

$$\Pi_F = \left[\sum_i \frac{1}{2}(\frac{fl}{d_h} + K)_i (\frac{a_r}{a_i})^2 \right]_o$$ [15]

Applying of Scaling Analysis to VHTR

To investigate the behavior of each of these Pi terms in the VHTR, the reactor vessel was divided into six control volumes or segments. The six segments of the reactor that comprise the loop are listed in order from where the air/helium mixture enters the hot duct of the vessel: 1. hot duct, 2. hot plenum, 3. core, 4. upper plenum, 5. upcomer and 6. cold duct in Figure 21. After examining probable experimental facility sizes as a function of scaling, a 1/8th scale was decided upon. a list of the key dimensions of the pressure vessel are given in Table 2
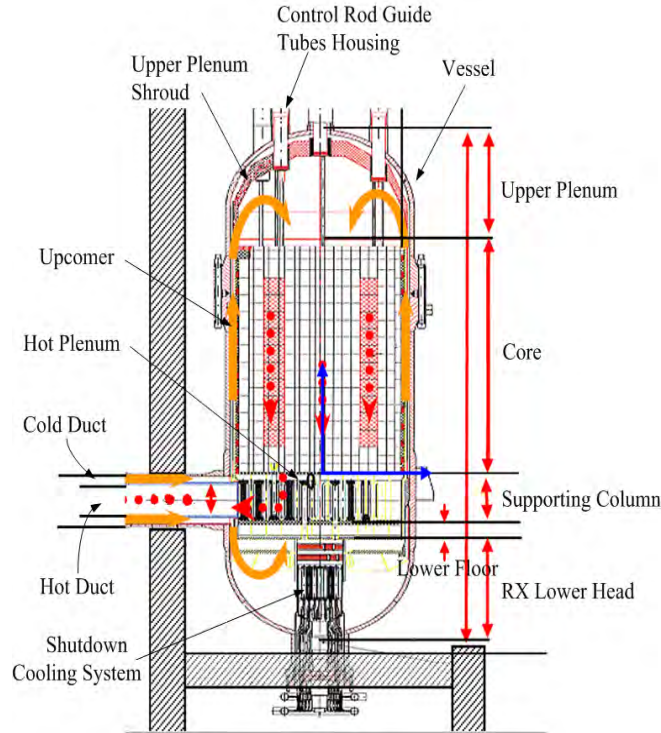
Figure 21. The gas-turbine modular helium reactor with key parameters indicated[14]

Table 2. List of key dimensions for VHTR pressure vessel

Parameters	Prototype	1/8th
Vessel Height (m)	23.7	2.963
Vessel I.D. (m)	7.8	0.975
Vessel O.D. (m)	8.4	1.050
Core Height (m)	11	1.375
Active Core Height (m)	7.8	0.975
"Donut" (m)	3.53	0.441
Support Column Height (m)	2.84	0.355
Cold Duct I.D. (m)	2.29	0.286
Hot duct I.D. (m)	1.43	0.179
Support Column Diameter (m)	0.212	0.027
Support Column Pitch (m)	0.36	0.045
Control Rod Guide Tubes Housing Diameter (m)	0.52	0.065
SCS Height (m)	3.52	0.415
SCS Diameter (m)	2.08	0.260
Upcomer Hydraulic Diameter (m)	0.243	

The first Pi term relates to the geometric scaling. If both the length scale and the radius scale are both 1/8th of the prototype dimensions, then the first Pi term is conserved as one moves from the prototype to the 1/8th scale.

The second Pi term is the Froude number. The Froude number is conserved in calculating the support column diameter and pitch for the scaled-down facility. A discussion of this procedure can be found in Arcilesi et al.[17] For all the simulations performed, the Froude number is on the order of 10^{-3}.

The third Pi term listed above is associated with the pressure loss through the entire reactor loop. The prototypic reactor parameters were used to calculate this term for each segment and a percentage of the total loss was calculated for each section. The percentage associated with each section is shown in Table 3, which indicates that the majority of the Pi term is associated with the core. It is important to note that a $1/8^{th}$ scale system also conserves these percentages almost identically.

Table 3. Pressure loss distribution during global circulation
(Hot Duct Velocity is 0.01 m/s)

Segments	Prototype	1/8th Scale
Hot Duct	0.0016%	0.0016%
Hot Plenum	0.0003%	0.0003%
Core	99.6414%	99.6416%
Upper Plenum	0.0000%	0.0000%
Upcomer	0.3522%	0.3520%
Cold Duct	0.0045%	0.0045%

Density-Driven Air Ingress versus Hot Plenum Natural Circulation

In order to understand how quickly the air ingress will transition from the first stage of density driven air ingress to the second stage of hot plenum natural circulation, a natural convection flow, one needs to understand the heat source, which is the graphite support columns located in the hot exit plenum. In studying the heat transfer properties of the support columns, we derived some temperature profiles for certain limiting cases. Using a one-dimensional, steady-state analysis assuming constant thermo-physical properties, a temperature profile was derived for a single IG-110 graphite support column. In case 1, Dirichlet boundary condition was prescribed where T_{top}= 850°C and T_{bottom}= 490°C. In case 2, a Robin boundary condition was prescribed where T_{top} = 850°C and q''_{bottom} = 0. In case 3, the wall temperature of the support column was assumed to be constant at T = 850°C. For cases 1-3, an analysis was performed for two different fluid compositions: 100% helium (He) and 100% nitrogen (N_2). The analysis was performed for two different containment temperatures. The averages of the three cases for the four different scenarios are summarized in Table 4.

Since the Biot number (hL_c/k), where $L_c \equiv V/A_s$ is less than 0.1 for the cases above, the error associated with using the lumped capacitance method is negligible. Therefore, the thermal time constant, which describes how quickly the temperature of the support column approaches the temperature of the surroundings, is given by $\tau_{thermal} = \rho V c /(h A_s)$, where ρ, V, c and A_s are the density, volume, specific heat and surface area of the support column, respectively. The large time scales in Table II indicate that the heat transfer from the support columns to the air/helium mixture is occurring very slowly. Similar calculations were performed for the scaled-down

experimental setup, wherein the support columns are constructed of IG-11 (an unpurified form of IG-110). These values are tabulated in Table 4.

Table 4. Heat transfer characteristics of support column for four different scenarios at prototype dimensions

Cases	Avg. Heat Transfer Coefficient (W/m^2-K)	Biot Number (hL$_c$/k)	Thermal Time Constant (s)
100% He, T$_\infty$ = 25°C	8.80	0.0049	15,640
100% He, T$_\infty$ = 170°C	7.80	0.0045	18,650
100% N$_2$, T$_\infty$ = 25°C	5.96	0.0034	23,890
100% N$_2$, T$_\infty$ = 170°C	4.93	0.0029	30,450
Average	6.87	0.0039	22,160

To gain a more complete understanding of the transition between density-driven air ingress and hot plenum natural circulation, the characteristic time scale for each phenomenon needs to be calculated and compared. In calculating a time scale for the density-driven air ingress, a method was used similar to that found in Oh & Kim[10]. Following that procedure, a time scale for the stratified flow was calculated to be 16.07 s. Helium temperature in this case was 850°C while the outside air temperature was 25°C. A similar calculation was done for a 1/8th scaled-down facility using the same density ratio (same temperatures). A time scale for this facility was found to be 5.68 s. It is three times slow than CFD calculation. As shown in the Figure 22, air fills the hot plenum and changes the direction to top as air plume hit the back vessel in the figure of 2.5 s. It's time difference comes from the assumption of scaling analysis: 1. the area of hot plenum path is half of the vessel, 2. the speed of air plume is at the center of the vessel. In Figure 22, the incoming air plume does not fill the half of the vessel. In addition, as air propagate at the hot plenum, the air spreads out and it slows down the speed. Thus, its larger path area and slow speed make the scaling analysis get 3 times slow time scale than CFD calculation.
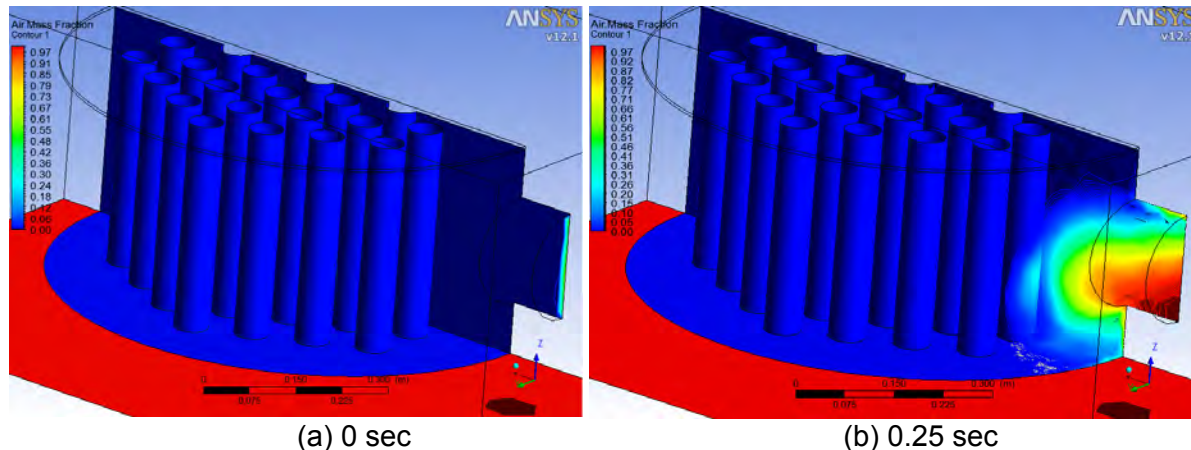
(a) 0 sec   (b) 0.25 sec
Figure 22. Fluent calculation of air mass fraction for a 1/8th scaled-down facility
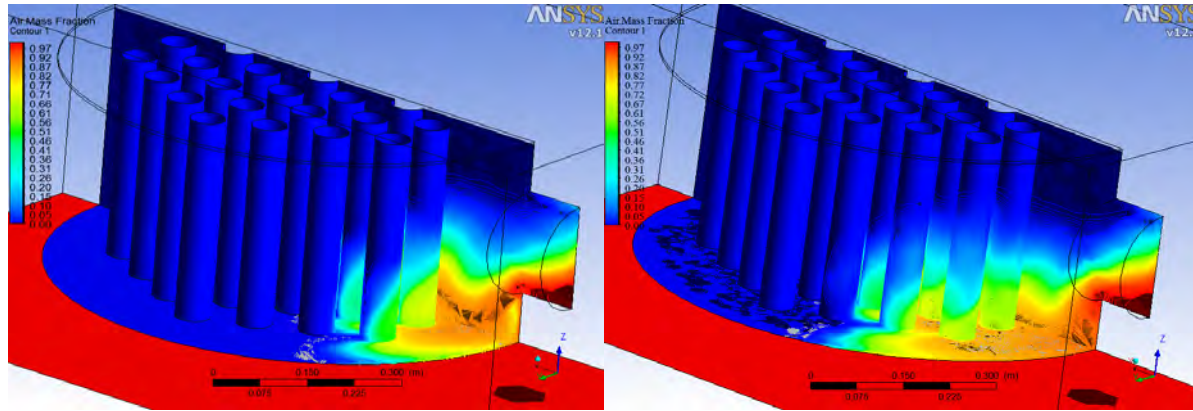
(c) 0.5 sec

(d) 0.75 sec
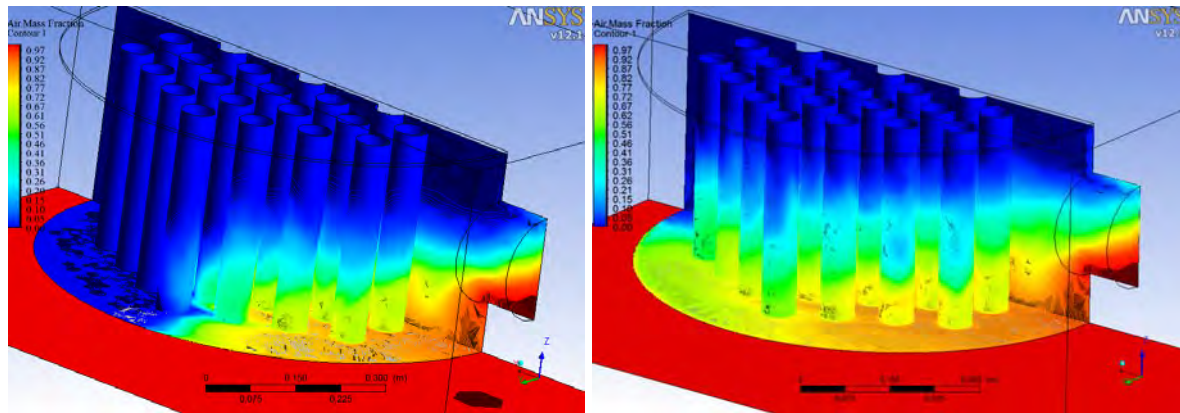
(e) 1 sec

(f) 1.5 sec
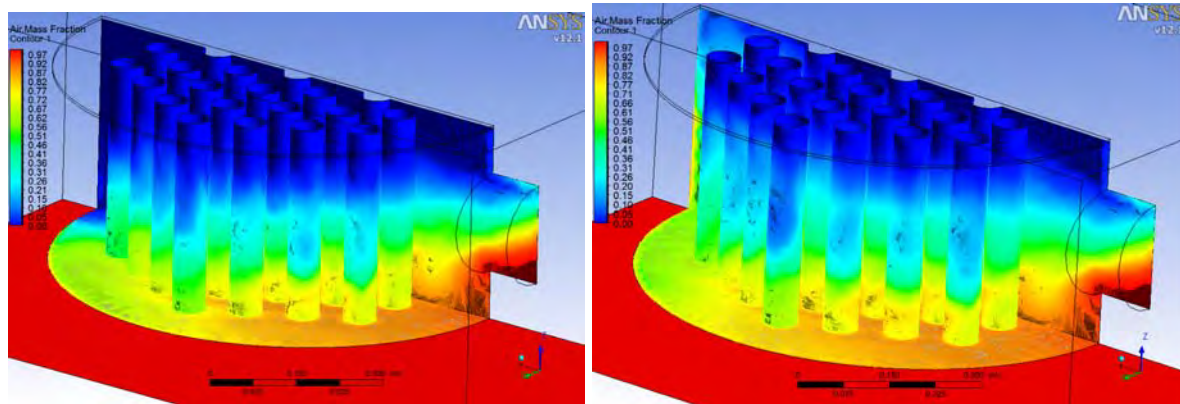
(g) 2 sec

(h) 2.5 sec

Figure 22. Fluent calculation of air mass fraction for a 1/8th scaled-down facility (Continued)

In addition, the thermal time constants for both the prototype and the scaled-down geometry are given in Tables 4 and 5, respectively. The average thermal time constants for these geometries are 22,160s and 4,450s. Therefore, the prototype-to-test facility thermal time constant ratio is 4.98.

These calculations for the scaled-down test facility (model) were done using support columns made of IG-11 graphite instead of IG-110 graphite. Total time scales were calculated using the following formula: $1/\tau = 1/\tau_{thermal} + 1/\tau_{gc}$, resulting in total time scales of 16.06 s for the prototype and 5.67 s for the scaled-down facility. In the literature[11], it has been predicted that the time to onset of natural circulation is 100 s in the prototype system. Assuming that this holds, it follows that the onset of natural circulation will be approximately 35 s in the scaled-down facility. Hence, with the current design, $\tau_p = 2.83\tau_m$, where subscripts "p" and "m" denote prototype and model, respectively. This analysis also illustrates that the time scale for natural convection flow is much longer than the time scale for the first stage density-driven air ingress. This should allow for the observation of the two distinct phases discussed: density-driven air ingress and hot plenum natural circulation flow.

Table 5. Heat transfer characteristics of support column for four different scenarios at scaled-down dimensions

Cases	Avg. Heat Transfer Coefficient (W/m^2-K)	Biot Number (hL_c/k)	Thermal Time Constant (s)
100% He, T_∞ = 25°C	15.49	0.0025	2,775
100% He, T_∞ = 170°C	14.01	0.0023	3,115
100% N$_2$, T_∞ = 25°C	7.71	0.0013	5,650
100% N$_2$, T_∞ = 170°C	7.03	0.0012	6,250
Average	11.06	0.0018	4,450

Hydraulic Similarity in the Hot Plenum

In looking to find hydraulic similarity for the air ingress natural circulation in the hot plenum, a model was created to find the best support column diameter and pitch for the test facility to mimic the pressure loss distribution of a hot duct-hot exit plenum system. The model assumes that the test facility's height, support column height, hot duct diameter and plenum diameter are a 1/8th scale of the prototype dimensions. Furthermore, the hot duct length is assumed to be 0.1 m. In the event of a hot duct break at the edge of the power conversion unit (PCU), the scaled-down length is 0.3575 m (which is equal to 1/8 of 2.86 m). Therefore, in this model, the hot duct length is approximately 28% of the scaled-down hot duct length. Other dimensions such as support column diameter and pitch are scaled by different factors.

The model, which is used to find the support column diameter and pitch in the test facility, divides the circulation flow path in the hot duct-hot exit plenum system into five segments or control volumes. The first segment is the bottom half of the hot duct. The second segment is the bottom half of the hot exit plenum. The third segment is the gas rising from the bottom to the of the hot exit plenum. The fourth segment is the top half of the hot exit plenum. The fifth segment is top half of the hot duct. The hot duct-hot exit plenum system with its corresponding five control volumes is shown in Figure 10.

The first and fifth control volumes correspond to the bottom and top half of the hot duct, respectively. In these two segments, the friction loss is the only pressure loss taken into consideration. The interface of segment (1) and segment (5) is treated as an additional

32

boundary due to a *quasi* no-slip boundary condition. This subtle detail becomes important when calculating the hydraulic diameter of these segments. Mathematically, the friction loss coefficient is computed as follows:

$$K_{friction} = f \frac{l}{D_h}$$ [16]

where
$$f = \begin{cases} \dfrac{64}{\mathrm{Re}}, & 0 < \mathrm{Re} < 2308.1487 \\ 3.03 \times 10^{-12} \, \mathrm{Re}^3 - 3.67 \times 10^{-8} \, \mathrm{Re}^2 + 1.46 \times 10^{-4} \, \mathrm{Re} - 0.151, & 2308.1487 \leq \mathrm{Re} < 4210.0770 \\ \dfrac{0.3164}{\mathrm{Re}^{0.25}}, & 4210.0770 \leq \mathrm{Re} < 51094.3686 \\ \dfrac{0.184}{\mathrm{Re}^{0.2}}, & \mathrm{Re} \geq 51094.3686 \end{cases}$$

The piecewise function for the friction factor is continuous. The friction factor correlation for the laminar-to-turbulent transition regime can be found in J.P Abraham et al.[18]

As the fluid passes from segment (1) to segment (2), the pressure loss due to expansion is taken into account. The calculation of the expansion loss coefficient utilizes the ratio of the cross-sectional area of segment (1) and the maximum cross-sectional area of segment (2). This results in a larger expansion loss coefficient than the real geometry would produce. The calculation done here assumes that the fluid empties directly into the largest cross-sectional area of the plenum which is obviously not the case. In reality, the fluid empties more gradually from the bottom half of the duct as it approaches the maximum cross-sectional area of the plenum. The expansion loss coefficient is based on the equations and correlation given by Idelchik[21] (pp. 160) and vary with respect to the Reynolds number.

The second and fourth control volumes correspond to the bottom and top half of the hot exit plenum, respectively. In these segments, there is a staggered array of bare rods that fill the entire control volume. Therefore, the only form of pressure loss that is accounted for in these segments is the friction pressure loss[19] due to the flow normal to the triangular array of bare rods. It should be noted that this model assumes that all the fluid passes along the entire length of the plenum. This results in an overestimate of the friction pressure loss. In reality, only a fraction of the fluid will pass along the entire length of the plenum. Moreover, due to the nature of the friction correlations available, this model assumes that bottom of the plenum is a square or rectangular shape as opposed to a circle which is in the prototype geometry. This assumption also leads to an overestimate of the friction pressure loss. Mathematically, the friction loss coefficient is expressed as follows:

$$K_{tri} = fNZ$$ [17]

where, f is the friction factor based on a correlation given in Todreas[19]; N is the number of tube rows in the direction of flow; Z is a correction factor depending on the array arrangement (correlation given in Todreas[19])

33

As the fluid passes from segment (4) to segment (5), the pressure loss due to sudden contraction is taken into account. The calculation of the contraction loss coefficient utilizes the ratio of the cross-sectional area of segment (5) and the maximum cross-sectional area of segment (4). This results in a larger contraction loss coefficient than the real geometry would produce. By similar reasoning given previously, the calculation done for this model assumes that the fluid empties directly from the largest cross-sectional area of the plenum into the top half of the hot duct which is not the case. In reality, the fluid is funnelled gradually into the top half of the hot duct from the maximum cross-sectional area of the top half of the hot exit plenum. However, since the same model is applied to both the prototype geometry as well as the scaled-down geometry, the overestimate in pressure loss can be neglected. The contraction loss coefficient is based on the equations and correlation given by Idelchik[21] (pp. 168) and vary with respect to the Reynolds number.

The third control volume corresponds to the vertical motion of the fluid from the bottom of the hot exit plenum to its top. In this segment, the friction loss is the only pressure loss taken into consideration. This friction loss is due to the fluid flow along the support columns.

To find the support column diameter and pitch, six limiting cases are considered. Table 6 shows the six single-species cases that are considered.

Table 6. Single-species cases considered in model

Case	Species Composition	Hot Temperature (°C)	Cold Temperature (°C)	Average Temperature (°C)
1	100% Helium	850	25	437.5
2			170	510
3			500	675
4	100% Air		25	437.5
5			170	510
6			500	675

For each case, segments (1) and (2) are at the cold temperature. Segments (4) and (5) are at the hot temperature and segment (3) is at the average temperature. The pressure for all five segments is atmospheric pressure. Since there is a temperature difference within the system, there exists a density difference or a driving force for natural circulation. Mathematically, the driving force is expressed as

$$\Delta P_d = (\rho_c - \rho_h)gh \qquad [18]$$

where ρ_c and ρ_h are the densities for the cold and hot temperature, respectively; g is the acceleration of gravity and h is the height of the plenum. Therefore, for a given case, there is a set driving force for natural circulation in the system.

Having established the natural circulation driving force for the system, the velocity is iterated until the resistance pressure drop, ΔP_{res}, is nearly equal to driving force, i.e. $|\Delta P_d - \Delta P_{res}| < 10^{-6}$. Mathematically, the resistance pressure drop is expressed as

$$\Delta P_{res} = \frac{1}{2} \sum_{i=1}^{5} K_{T,i} \rho_i v_i^2 \qquad \text{[19]}$$

where $K_{T,i}$ is the total loss coefficient for i^{th} segment ; ρ_i, v_i is the density of the fluid and the fluid velocity for the ith segment, respectively. It should be noted that the model assumes that the amount of mass within the entire system does not change with time. Therefore, the mass flow rate remains constant from segment to segment. Using this fact along with the density and flow area of each segment, the velocity for a given control volume can be found.

Once this procedure has been followed for the prototypical geometry for a given set of temperatures, there is a unique non-dimensional Froude number that is recorded. The non-dimensional Froude number is defined as

$$\Pi_{Fr} = \frac{\rho_r v_r^2}{(\rho_c - \rho_h)gh} = \frac{\rho_3 v_3^2}{(\rho_c - \rho_h)gh} \qquad \text{[20]}$$

Now, with the scaled-down geometry, that is, the plenum diameter, the plenum height, the support column height and hot duct diameter at 1/8th scale and the hot duct length reduced to 0.1 m, the velocity is adjusted to preserve the non-dimensional Froude number for a given case. This means that the velocity is reduced by a factor of $\sqrt{8}$ in order to preserve the non-dimensional Froude number. Since an adjustment of both the fluid velocity as well as the test facility geometry has taken place, the driving force is no longer equal to the resistance pressure drop. The two quantities can be equated by scaling down the support column pitch and diameter by the same factor. The scaling factor is iterated until $\left| \Delta P_d - \Delta P_{res} \right| < 10^{-6}$.

Results

These simulations were completed for nine different cases. Cases (1) – (6), given in the previous section (Table 6), are single species simulations (either Air or He). Cases (7) – (9) are mixed species simulations. Again, all simulations were performed at atmospheric pressure for all segments. Table 7 below shows the species composition and temperature by segment.

Table 7. Species composition and temperatures for each segment for cases (7) – (9)

Segments	(1) and (2)	(3)	(4) and (5)
Species Composition	80% Air/20% Helium	50% Air/50% Helium	20% Air/80% Helium
Case #	Temperature (°C)		
7	25	437.5	850
8	170	510	850
9	500	675	850

Fluid density and dynamic viscosity for the mixed species compositions are calculated according to the following equations. The mixture density is determined from the ideal gas laws as a linear combination of the mole fraction of the components (1: air; 2: helium).

$$\rho_{mix} = \rho_1 x_1 + \rho_2 x_2 \tag{21}$$

where x_1 and x_2 are the mole fractions of the individual components in the mixture. The dynamic viscosity of the mixture is determined by the following set of equations.

$$\mu_{mix} = \mu_1 \left(1 + \frac{x_2}{x_1}\Phi_{12}\right)^{-1} + \mu_2 \left(1 + \frac{x_1}{x_2}\Phi_{21}\right)^{-1} \tag{22}$$

where

$$\Phi_{ij} = \left[1 + \left(\frac{\mu_i}{\mu_j}\right)^{1/2}\left(\frac{M_j}{M_i}\right)^{1/4}\right]^2 \left[8\left(1 + \frac{M_j}{M_i}\right)\right]^{1/2} \qquad i \neq j \tag{23}$$

These relations can be found in Banerjee and Andrews[12].
By maintaining the non-dimensional Froude number similarity and adjusting the support column pitch and diameter to balance the circulation driving force with the pressure drop, a set of support column pitches and diameters is collected. Each case has a unique pitch and diameter that ensures that these conditions are satisfied. These values are tabulated in   Table 8 for each case along with the arithmetic average for the nine values.

Table 8 : Resultant support column pitches and diameters for cases (1) – (9)

Case Number	Support Column Pitch (cm)	Support Column Diameter (cm)
1	11.8	6.9
2	15.2	8.9
3	23.4	13.8
4	7.2	4.2
5	7.1	4.2
6	10.0	5.9
7	6.6	3.9
8	6.2	3.7
9	6.5	3.8
Average	10.4	5.7
Adjusted Average	8.8	5.2

Therefore, from the tabulated values, the support column pitch and diameter for the scaled down test facility to ensure hydraulic similarity is 10.4 cm and 5.7 cm, respectively. Moreover, if Case 3 is removed from consideration, the averages drops to 8.8 cm and 5.2 cm. It should be noted that the pitch and diameter were scaled by the same factor. Hence, the pitch-to-diameter ratio in the scaled-down test facility is equal to the pitch-to-diameter ratio in the prototype.

From the scaling analysis, another key non-dimensional Pi term is the resistance number. The resistance number is defined as follows:

$$\Pi_F = \sum_i \frac{1}{2}\left(\frac{fl}{D_h} + K\right)_i \left(\frac{a_r}{a_i}\right)^2 \tag{24}$$

36

For the nine cases given above, the relative accuracy with respect to the resistance number of the prototype is given i.e. $R=\dfrac{\left(\Pi_{F}\right)_{m}}{\left(\Pi_{F}\right)_{p}}$.

Table 9. Similarity Ratio of resistance number for each case

	Similarity Ratio (R)
Case 1	0.991
Case 2	0.998
Case 3	1.046
Case 4	0.969
Case 5	0.980
Case 6	1.017
Case 7	1.055
Case 8	1.040
Case 9	1.008
Average	1.012
Adjusted Average	1.007

This shows that there is good agreement between the resistance number of the prototype and the resistance number of the scaled-down facility.

Heat Transfer Similarity

In order to understand how quickly the air ingress will transition from the first stage of density driven air ingress to the second stage of hot plenum natural circulation, a natural convection flow, one needs to understand the heat source which is the graphite support columns located in the hot exit plenum. In studying the heat transfer properties of the support columns, some temperature profiles were derived for certain limiting cases. Using a one-dimensional, steady-state analysis assuming constant thermo-physical properties, a temperature profile was derived for a single IG-110 graphite support column. Some previous calculations have been updated in this section. In case 1, Dirichlet boundary condition was prescribed where T_{top} = 850°C and T_{bottom} = 490°C. In case 2, a Robin boundary condition was prescribed where T_{top} = 850°C and q''_{bottom} = 0. In case 3, the wall temperature of the support column was assumed to be constant at T = 850°C. A parametric study was performed to calculate the heat transfer coefficient due to natural convection, the Biot number, the transient conduction time constant and the boundary layer thickness at the top of the support column. The average values of the three cases for the four heat transfer characteristics were calculated with error bars that extend one standard deviation in each direction. They were calculated for different far-field temperatures (from 20 - 500°C) and for different species compositions (from 0 – 100% Air in 10% mole fraction increments). The heat transfer coefficient was calculated based on the following correlations[20]:

$$Nu = \begin{cases} 0.59(Ra)^{1/4}, 10^{4} < Ra < 10^{9} \\ 0.10(Ra)^{1/3}, 10^{9} < Ra < 10^{13} \end{cases} \qquad [25]$$

Figure 23 through Figure 33 show the heat transfer coefficients for the prototype and scaled-down geometries at different far-field temperatures and species compositions. The Biot

numbers calculated are on the order of 10^{-3} and, in some cases, 10^{-4}. The transient conduction time constants are on the order of 10^4 for the prototype geometry and 10^3 for the scaled-down geometry.

Figure 23 and Figure 24 show that despite using three different boundary conditions (cases 1 – 3), varying the species composition (0 – 100% He) and parameterizing over the far-field temperature (20 - 500°C), and changing the geometry (prototype and scaled-down), the heat transfer coefficient remains within a range of $3 – 16$ W/(m^2*K). Therefore, no matter what species compositions and far-field temperatures are presented during the course of an experiment, the same basic heat transfer characteristics will remain.
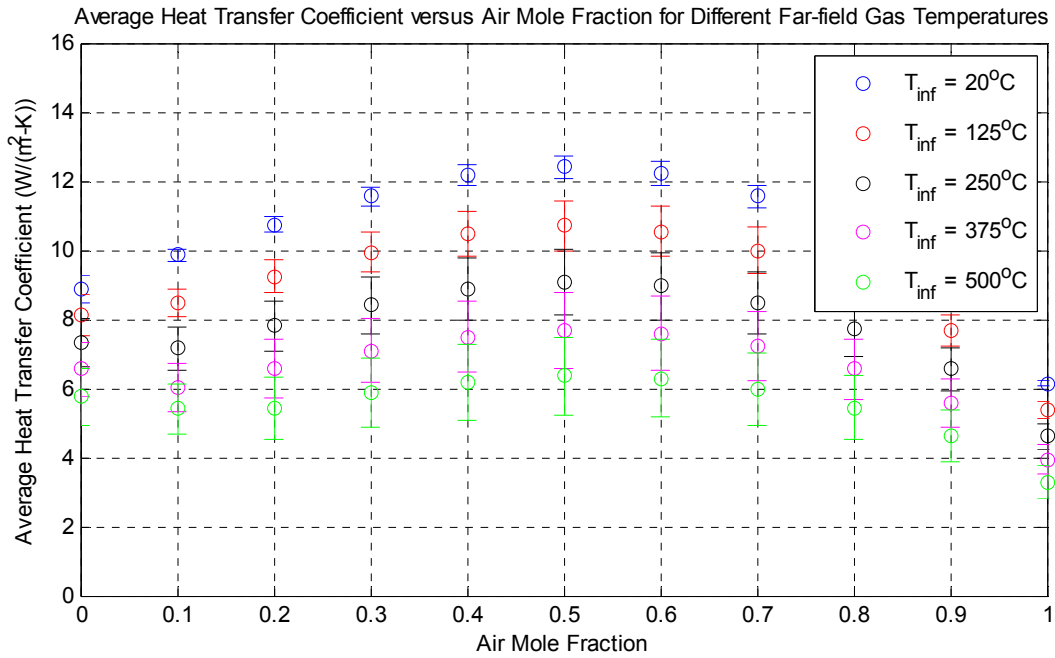
Figure 23. Average heat transfer coefficient for prototype geometry
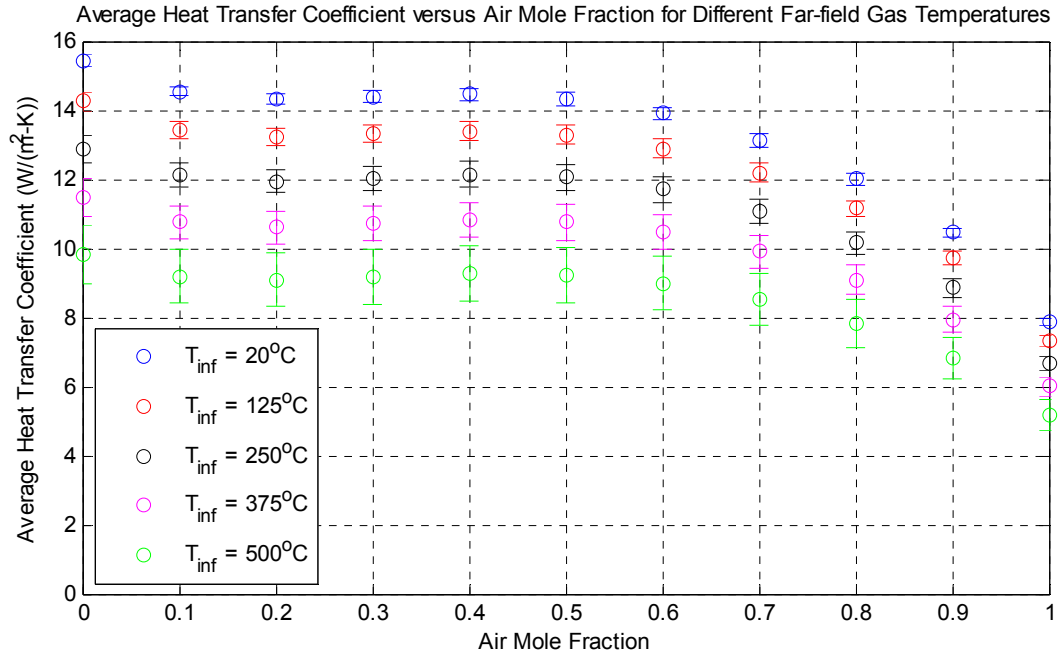
Figure 24. Average heat transfer coefficient for scaled-down geometry
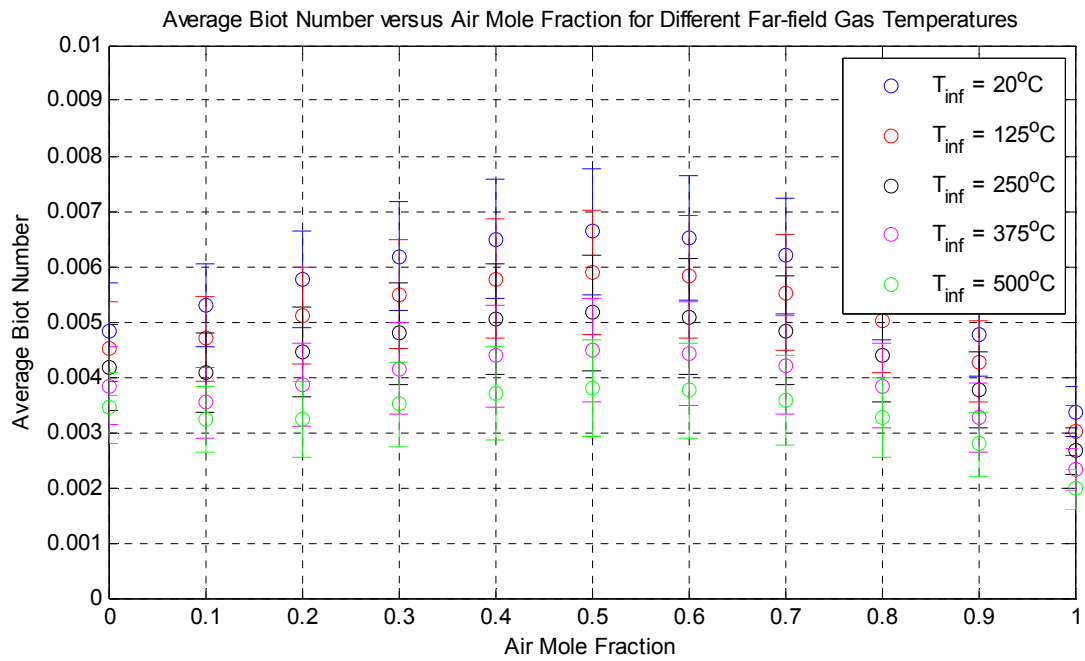
Figure 25. Average Biot number for prototype geometry
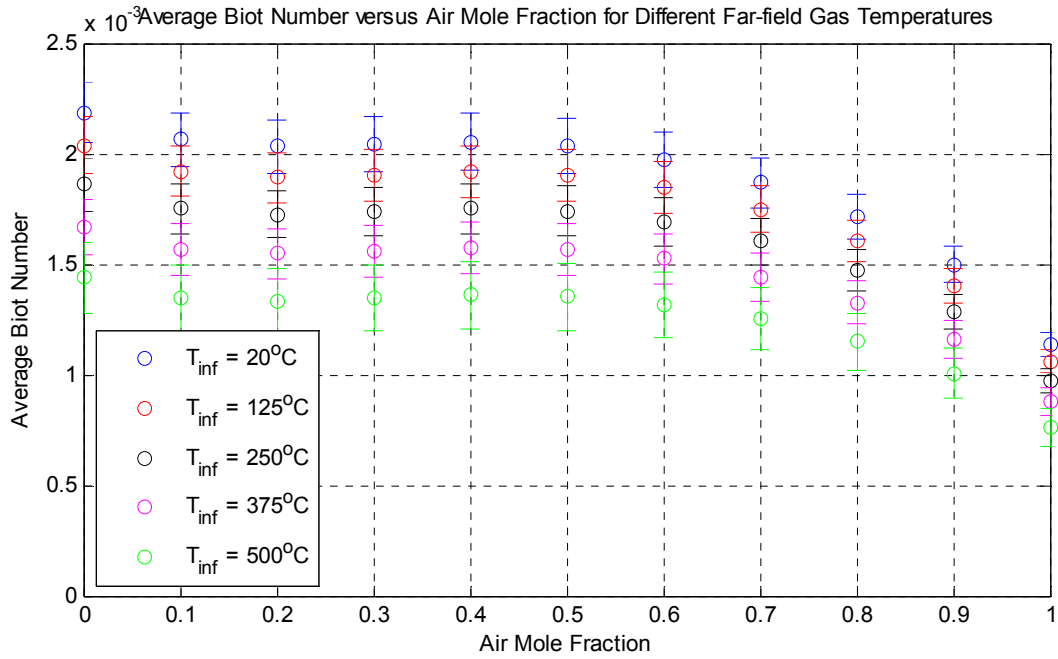
Figure 26. Average Biot number for scaled-down geometry
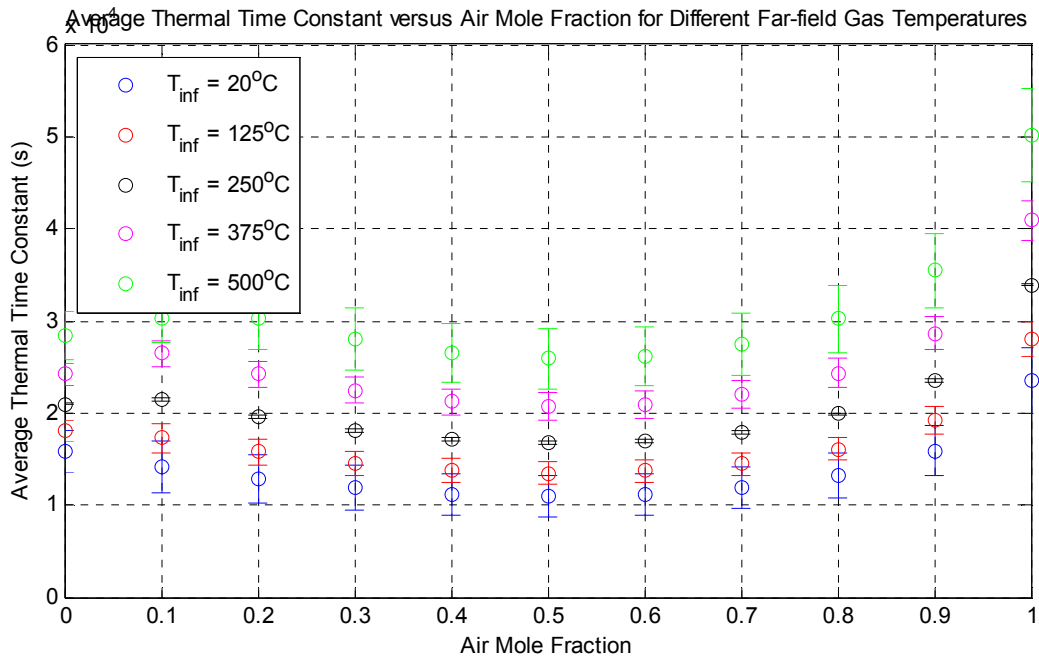
Figure 27. Average thermal time constant for prototype geometry
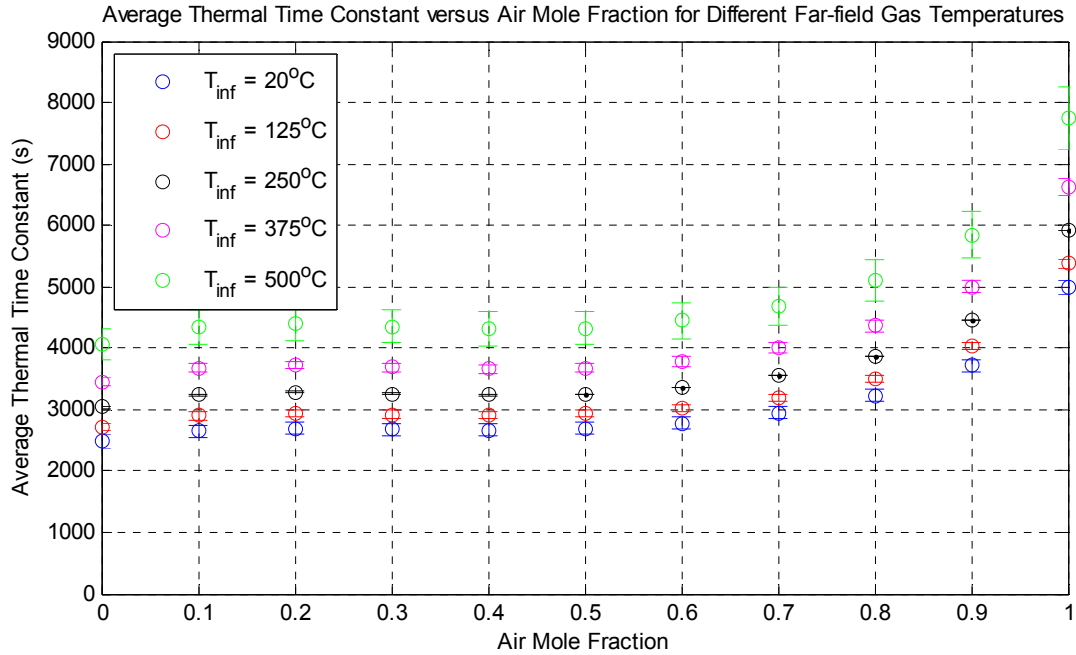
Figure 28. Average thermal time constant for scaled-down geometry

Figure 29 and Figure 30 show how the natural circulation boundary layer thickness at the top of the support column behaves as a function of the far-field temperature for different species compositions.
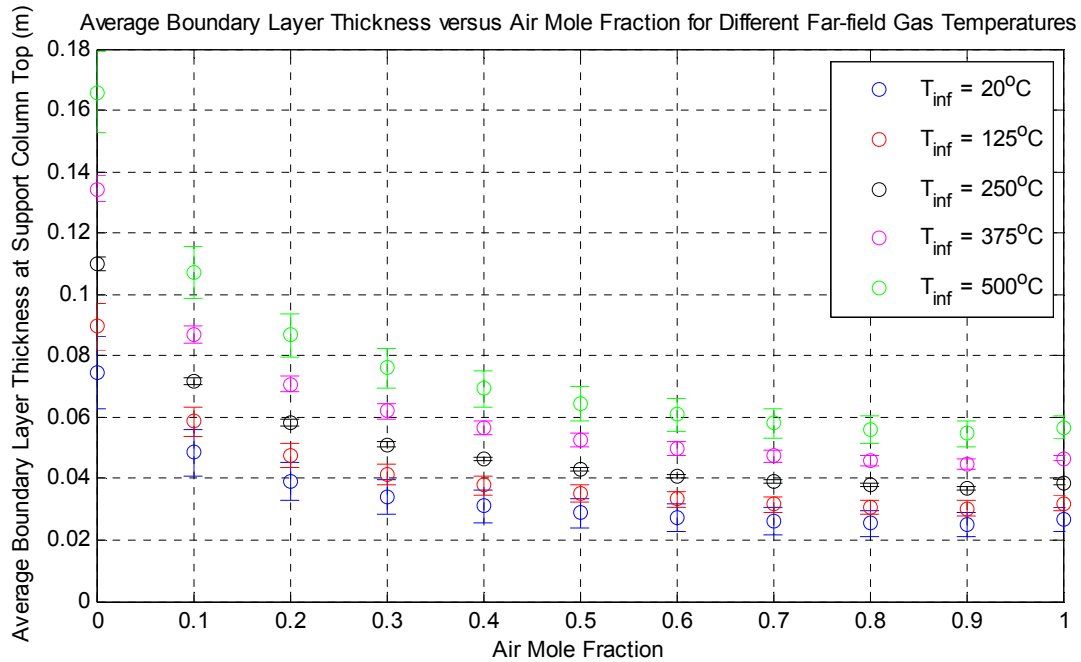
Figure 29. Average boundary layer thickness for prototype geometry
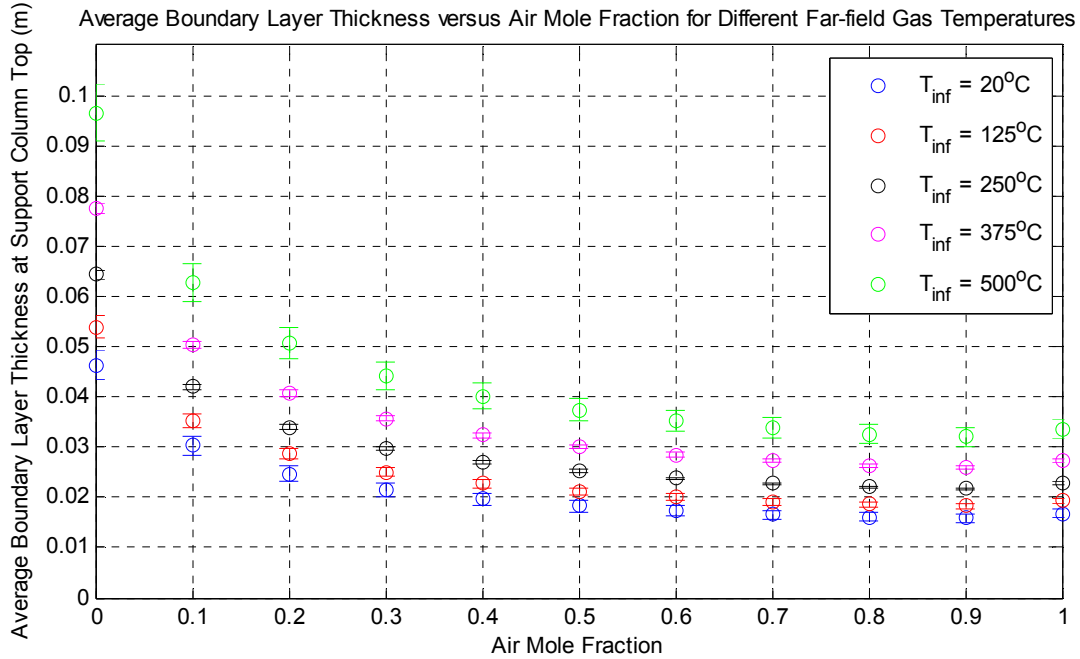
Figure 30. Average boundary layer thickness for scaled-down geometry

With the small Biot numbers (as seen in Figure 25 and Figure 26), the lumped capacitance approximation is valid. However, to confirm this approximation and to also establish the heater power in the scaled-down facility so that the natural circulation phenomenology is maintained, a code was written to produce radial temperature profiles for (i) a prototypic support column, (ii) a scaled-down support column, and (iii) a scaled-down heater-rod system. A scaled-down heater-rod system is a practical and viable design in that a high rod wall temperature (750°C) can be achieved without exceeding the maximum heater sheath temperature (1120°C) of a Watlow® MULTICELL^{TM} heater. A one-dimensional, steady-state calculation shows that a rod wall temperature of 750°C can be achieved while the heater is exerting 1000W. Under these conditions, the calculation also shows that the surface temperature of the heater is approximately 900°C. This surface temperature is well below the aforementioned maximum heater sheath temperature. Figure 31-Figure 33 are radial temperature distributions. On each figure, there are multiple distributions which correspond to different non-dimensional times (t/τ) in the transient. The non-dimensional times are 0, 0.05, 0.10, 0.25, 0.5, 1.0, 1.5, 2.0, 2.5, and 3.0. The non-dimensional time of 0 corresponds to a flat temperature distribution and a non-dimensional time of 3 corresponds to the line with the lowest temperature at a given position. The time scale, τ, for the prototype is 16.1 s and the time scale for the scaled-down facility is 5.7 s.

The code utilizes a finite-difference discretization and an explicit time-marching method. Constant thermo-physical properties are assumed for this calculation. Density is taken to be 1770 kg/m^3. Specific heat capacity is taken to be 1720 J/(kg-K). Thermal conductivity is taken to be 85 W/(m-K). These values correspond to an IG-110 graphite temperature of 750°C.[13] The governing equation is a single spatial dimension (radial variable) transient heat diffusion equation for cylindrical coordinates. The initial condition is 750°C on the entire circle (or, for case (iii), on the entire annulus). For cases (i) and (ii), the boundary conditions are the symmetry boundary condition at the origin or center of the circle and a Newton cooling boundary condition at the edge of the circle. For case (iii), a constant heat flux boundary

condition was imposed on the inner radius which is equal to the heat flux output of the heater. On the outer radius, a Newton cooling boundary condition was imposed. Mathematically,

Governing Equation

$$\rho c_p \frac{\partial T}{\partial t} = \frac{1}{r}\frac{\partial}{\partial r}\left(kr\frac{\partial T}{\partial r}\right); r_1 \le r \le_2; t \ge 0 \qquad [26]$$

where r_1, r_2 is the inner and outer radius of the column, respectively. For case (i), r_1=0 and r_2=0.106 m. For case (ii), r_1=0 and r_2=0.0275 m. For cases (iii), r_1=0.0125 and r_2=0.0275 m.

Initial Condition

$$T(r, t=0) = 750°C; r_1 \le r \le r_2 \qquad [27]$$

Boundary Conditions

Cases (i) and (ii):

Boundary Condition #1:

$$\left.\frac{\partial T}{\partial r}\right|_{r=0} = 0 \qquad [28]$$

Boundary Condition #2:

$$-k_s \left.\frac{\partial T}{\partial r}\right|_{r=r_2} = h(T(r=r_2, t) - T_\infty) \qquad [29]$$

Case (iii):

Boundary Condition #1:

$$-k_s \left.\frac{\partial T}{\partial r}\right|_{r=r1} = q''_{heater} \qquad [30]$$

where q''_{heater} is the heat flux of the Watlow® MULTICELL™ heater.

Boundary Condition #2:

$$-k_s \left.\frac{\partial T}{\partial r}\right|_{r=r_2} = h(T(r=r_2, t) - T_\infty) \qquad [31]$$

Below are the temperature profiles.

Temperature v. Radial Position (Prototype Support Column; T_{inf}=25°C; h=12.7 W/(m²*K); τ=16.1 s)
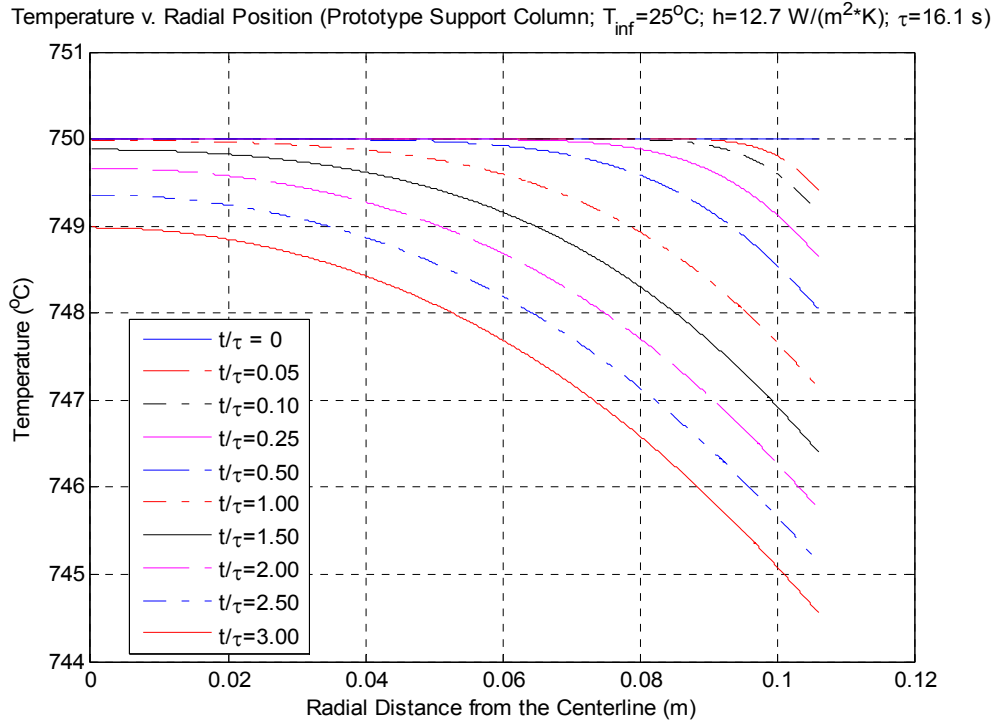
Figure 31. Radial temperature profile for prototype geometry at different times (t/τ)

Temperature v. Radial Position (Scaled-down Support Column; T_{inf}=25°C; h=15.6 W/(m²*K); τ=5.7 s)
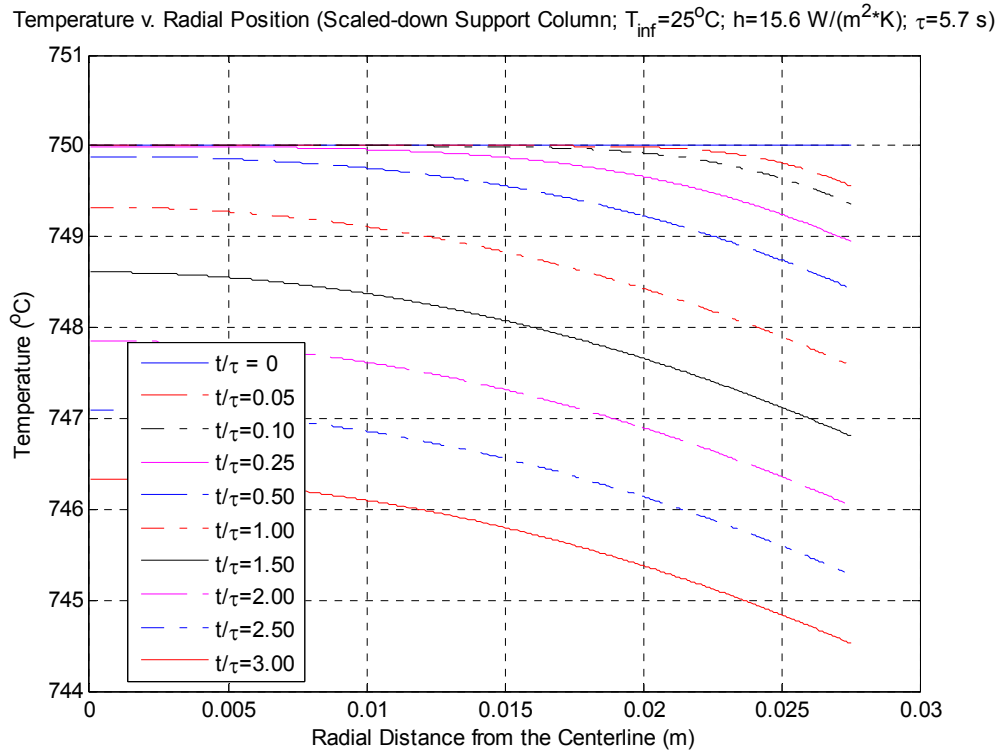
Figure 32. Radial temperature profile for scaled-down geometry at different times (t/τ)
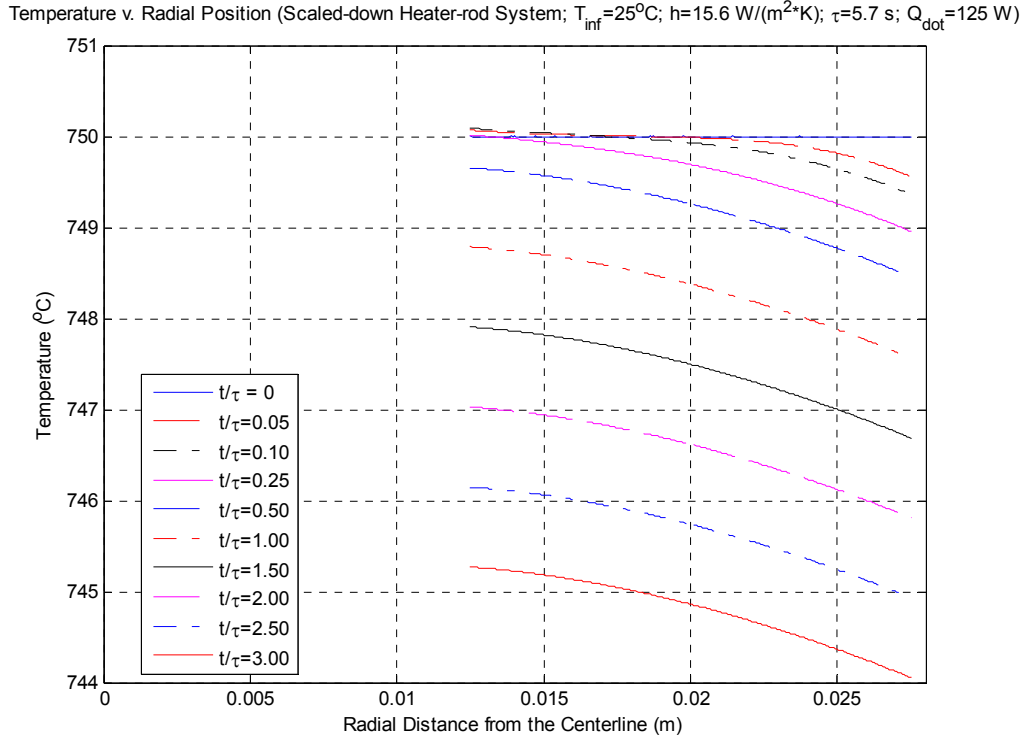
Figure 33. Radial temperature profile for heater-rod scaled-down system at different times (t/τ)

There is good agreement among Figure 31-Figure 33.   Thus, the natural circulation phenomenology will be preserved according to these calculations. The temperature profile varies negligibly over the radius of the rod/annulus. Therefore, the lumped capacitance method is a good approximation. Also, a heater power of 125 W creates a temperature profile through the annular portion of the scaled-down rod-heater system (Figure 31) similar to that shown in the scaled-down support column (Figure 32) and the prototypic support column (Figure 33). Therefore, there exists a heater power that can be utilized during the course of an experiment such that similar temperature profiles can be achieved among the three different support column geometries. Thereby, the natural circulation phenomenology of the prototype is preserved, during the course of an experiment on the scaled-down facility.

Expected Mass Flow Rate (CFD Results)

One-dimensional, steady-state analyses with nine different cases were performed cases to determine the support column diameter and pitch so that a hydraulic similarity can be established between the prototype and the scaled-down facility. This case study varied the temperature and mole fraction of the air-helium mixture at each segment. Fluid properties for segments (1) and (2) are calculated at the atmospheric pressure and cold temperature. Fluid properties for segments (4) and (5) are calculated at the atmospheric pressure and the high temperature. Properties for the segment (3) are at the atmospheric pressure and an average of the hot and cold temperature. The Reynolds numbers in the
Table 10 shows the flows at the hot plenum and the cross vessel may fluctuate between laminar and turbulent flow, but most flows are in the laminar flow regime. Based on the results, three-dimentional (3D) CFD calculations were performed with one-half of the experimental facility as shown in Figure 34. The total numbers of meshes of this model are approximately 1 million and the meshes are exclusively polyhedral meshes.

45

Table 10. Reynolds number for cases (1) – (9) at each segment

Case #	Hot Temperature (°C)	Cold Temperature (°C)	Species Coposition	Reynolds Number at Segment #				
				1	2	3	4	5
1		25		1.190E+03	1.251E+02	3.474E+01	4.952E+01	4.714E+02
2		170	100% He	6.038E+02	8.155E+01	2.780E+01	4.244E+01	3.142E+02
3		500		1.345E+02	2.887E+01	1.269E+01	2.217E+01	1.064E+02
4		25		1.168E+04	7.451E+02	2.031E+02	3.011E+02	4.720E+03
5	850	170	100% Air	5.564E+03	3.535E+02	1.220E+02	1.928E+02	3.034E+03
6		500		1.620E+03	1.446E+02	6.462E+01	1.150E+02	1.288E+03
7		25	80% Air, 20% He segment 1,2	4.627E+04	2.736E+03	1.402E+03	1.054E+03	1.721E+03
8		170	80% Air, 20% He segment 3	2.065E+04	1.938E+03	1.231E+03	9.907E+01	1.056E+03
9		500	80% Air, 20% He segment 4,5	9.657E+03	5.576E+02	4.615E+02	4.249E+02	7.358E+03

To better understand the density-driven flow and hot plenum natural circulation two cases were run in the calculation: an isothermal case and a non-isothermal case. For the isothermal calculation, the inside helium gas and outside air temperatures were both set as 300 K. For the non-isothermal calculation, the inside and outside gas temperatures were set as 1,023 and 300 K, respectively. Both cases assumed that the air-ingress process would start once the inside and outside pressures are equalized. Thus, the initial pressure was set to 1 atm.

Due to the limitation of laminar-turbulent transition in CFD calculation, laminar and turbulent model are calculated separately and the experimental results are expected to between the laminar and turbulent computational calculations, but closer to laminar calculation. Initially, the facility was filled with only helium while the outside of the facility is only air. Although the outside of the facility should be an air-helium mixture in the real accident because of the helium depressurization, 100% air was set in order to give a more severe condition by yielding a larger density difference. Energy and species (air/helium) transport equations were used and a second-order upwind differencing scheme was employed.
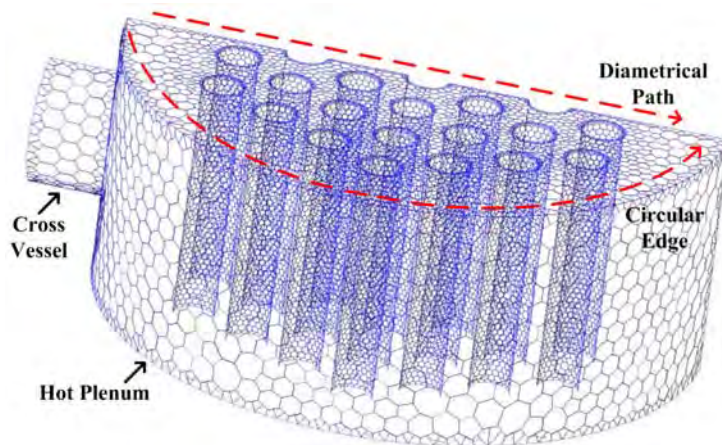
Figure 34. 3D Geometry of Air-ingress Experiment Facility

The initial stage of the air-ingress phenomenon is driven by the density difference between the outside air and inside helium. Figure 35 shows the air mass fraction of the isothermal case. When air enters into the facility, the top of the plume is approximately half of the height of the cross vessel, which appears to be consistent with the theoretical model. It clearly shows the density-driven flow at the initial moments of the air-ingress. Once the air reaches to the bottom

of the hot plenum, the air plume spreads out due to the round shape of hot plenum bottom. Even though the diametrical path is a shorter length than the outside circular edge, the graphite supporting columns introduce resistance to the flow. Thus, the flow through diametrical path and outside circular edge reaches to the other side of the cross-vessel at approximately the same time. In addition, the height of the initial plume through hot plenum is not one-half of the height of the facility as previously expected

(a) 0.25 sec

(b) 0.5 sec

(c) 1.0 sec

(d) 2.0 sec
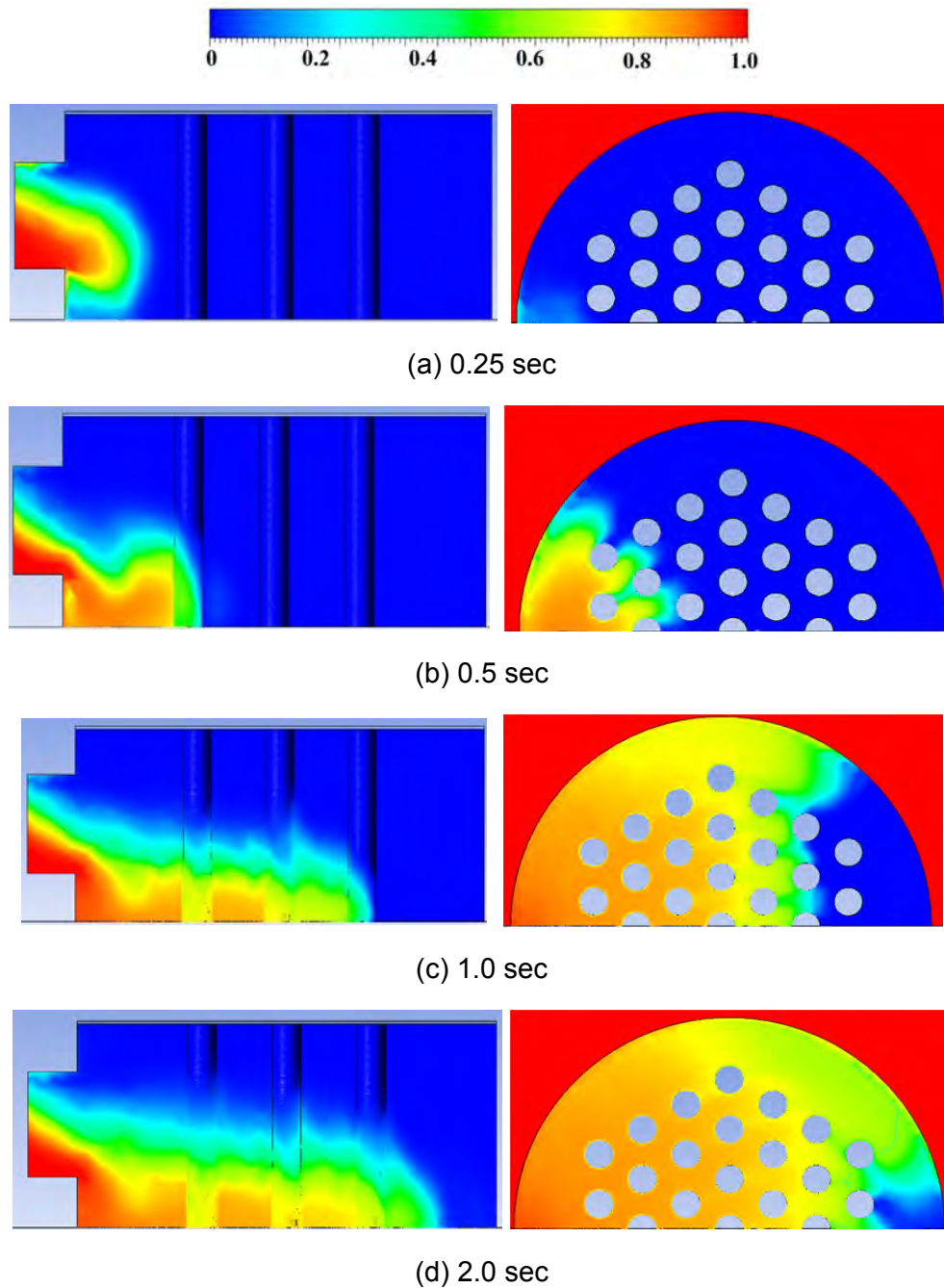
Figure 35. Air mass fraction – side view (left) and lower view (right)

The amount of air in the facility and mixture velocity at the cross vessel with respect to time are presented in Figure 36 and Figure 37, respectively. The saturated amount of air difference detween isothermal and non-isothermal case is due to gas density difference in the hot plenum. While isothermal case maintains constant temperature, non-isothermal case heats the incoming gas mixture. For the non-isothermal case, the amount of air in the hot plenum is saturated at approximately 40 seconds. However, the incoming mixture velocity through the cross vessl is maintained. On the other hand, the intrusion velocity of the isothermal case decreases with respect to time. This may suggest that the air-ingress mechanism is changing from the density-driven air ingress phenomenon to hot plenum natural circulation. As shown in Figure 38, the density difference is maintained between inside and outside facility for the non-isothermal case even though the air mass in the hot plenum is saturated. Thus, continuous air-helium mixture flow can be measured for the non-isothermal case. While the flow of the isothermal case is decreased as air fills the inside experimental facility.
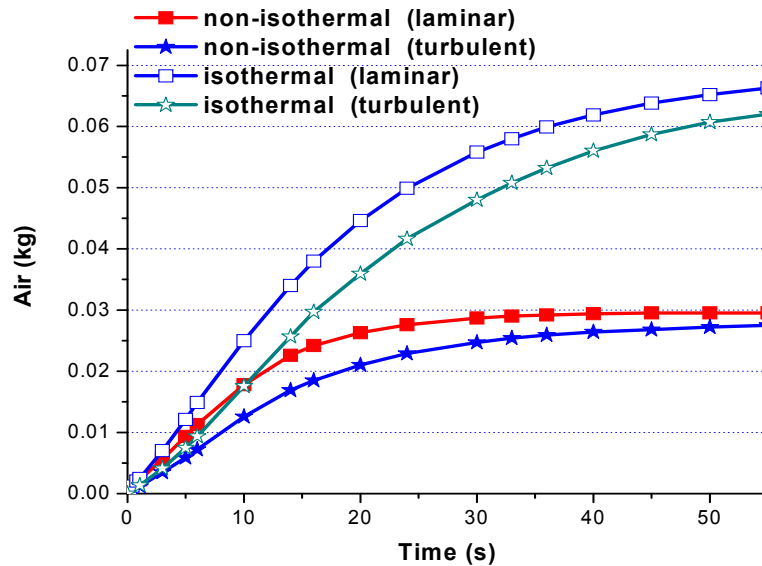
Figure 36. Accumulated Air in the experimental facility
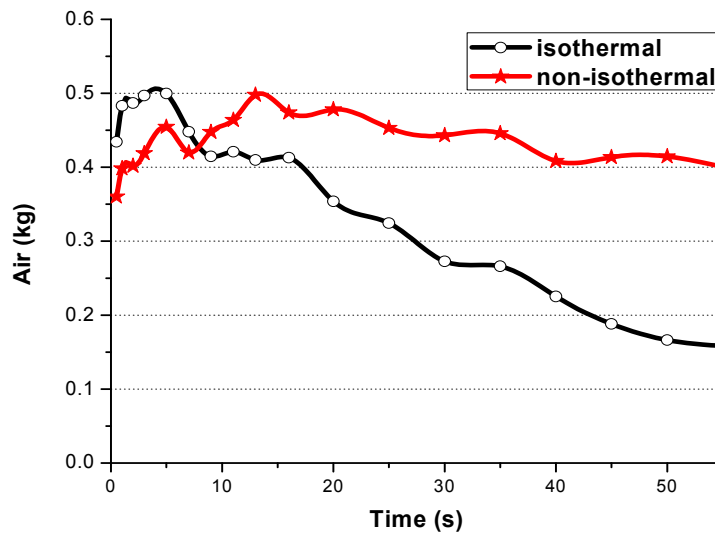
Figure 37. Air-Helium mixture plume head velocity into the facility at the center of cross vessel
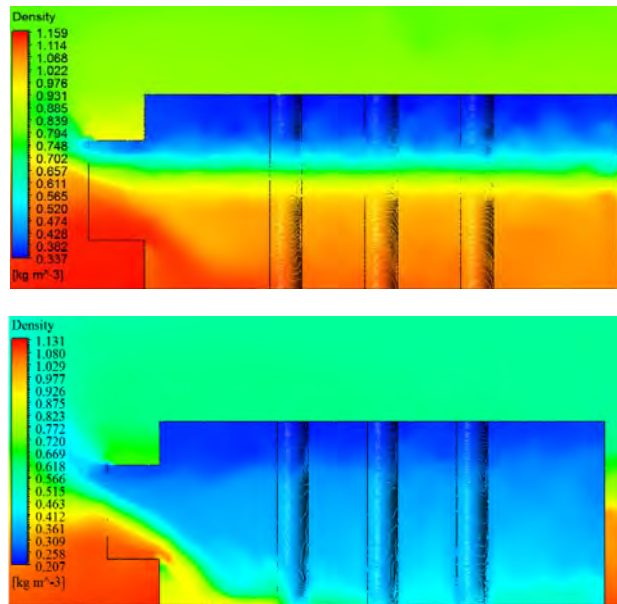
Figure 38. Density contour of isothermal (top) and non-isothermal (bottom) at 40 seconds

Mesh Sensitivity Study

To quantify the uncertainty of the CFD calculations, a grid sensitivity study was performed for the simulation using a laminar flow model. The grid sensitivity study used a method based on the Richardson extrapolation to estimate the grid convergence. Three different meshes were assumed. The coarse, medium, and fine meshes utilized 75,455, 160,756, and 339,890 polyhedral meshes, respectively. Figure 39 shows the accumulated air mass in the lower plenum for the three meshes with the FLUENT.

With grid triplet (set of fine mesh, medium mesh, and coarse mesh) solutions, order of convergences (p), grid convergence index (GCI), and estimated flow rates, can be calculated by:

$$p = \frac{\log\left(\frac{f_3 - f_2}{f_2 - f_1}\right)}{\log r}, r = h_3 / h_2 = h_2 / h_1 \tag{32}$$

$$GCI_{12} = F_s \frac{\left|\frac{f_2 - f_1}{f_1}\right|}{r_{21}^p - 1}, \quad GCI_{23} = F_s \frac{\left|\frac{f_3 - f_2}{f_2}\right|}{r_{23}^p - 1} \tag{33}$$

$$f_0 = f_1 + \frac{f_1 - f_2}{r^2 - 1} \tag{34}$$

Table 11. Additional data for mesh refinement study results

Time (s)	p	GCI_{12}	GCI_{23}	Asymptotic range of convergence	Mass flow rate (g/s)
0	-	-	-	-	-
0.3	1.470	0.026	0.100	1.267	4.02
0.4	1.729	0.016	0.068	1.151	3.31
0.5	1.870	0.013	0.046	0.896	2.11
0.6	1.682	0.011	0.054	0.841	1.90
0.7	2.431	0.076	0.193	1.397	2.90
0.8	3.577	0.044	0.123	1.147	3.30
0.9	3.925	0.042	0.112	1.017	2.85
1.0	3.764	0.047	0.123	1.021	2.99
1.25	3.604	0.060	0.140	0.960	2.98
1.5	3.148	0.081	0.176	0.994	2.81
1.75	2.802	0.106	0.210	0.995	2.64
2.0	2.427	0.133	0.257	1.065	2.76
2.5	2.311	0.156	0.291	1.056	2.80
3.0	2.125	0.184	0.324	1.044	2.79

where f is the amount of air accumulated in the lower plenum; subscript 1, 2, and 3 represent the fine, medium, and coarse grids, respectively, and r is the mesh refinement ratio. The results and the asymptotic range of convergence values are tabulated in Table 11. As time progresses, the asymptotic range of convergence remain near unity. Thus, the solutions are well within the asymptotic range of convergence. The GCI is a measure of the percentage of the computed value. It shows the error band of the solution. Figure 40 shows the extrapolated flow velocity with error bars with a 95% range of confidence. Based on the results, the error of the beginning of the air ingress was 3%; however, the error is getting smaller as the density driven flow stabilizes. Thus, the results with fine mesh are quite reliable.
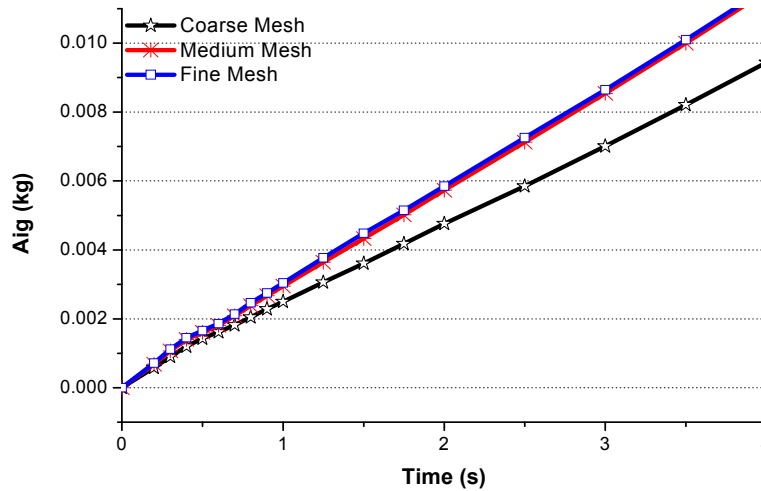
Figure 39. Mesh refinement results of accumulated Air mass in vessel
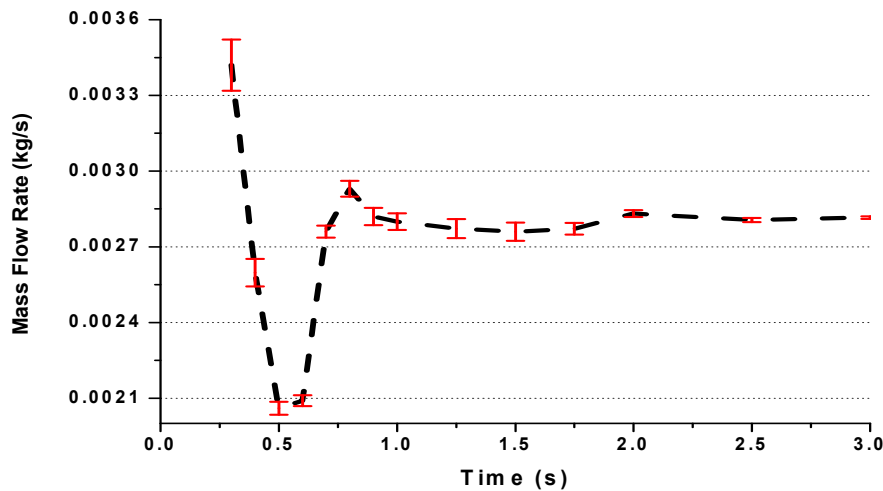
Figure 40. Extrapolated mass flow rate

Depressurization

Once the guillotine break of the cross vessel is initiated, the coolant (helium) of the reactor is discharged into the containment. The reactor pressure vessel is located in a cavity which is filled with air during normal operation; the discharged helium will be mixed with air. The mixture concentration and temperature is the key parameter for the next scenario, therefore, it should be calculated precisely.

To study the depressurization effect, a simplified 3D CFD calculation was performed. Figure 41 shows the simplified 3D CFD model. Instead of using the prototypic geometry, a regular hexahedron design with conserved volume was used. The vessel and containment volume are 265 and 25,000 m^3, respectively, same as the prototypic design. The size of the break was set to 2.241 m^2 which is the cross sectional area of the cross vessel to hypothesize a double-ended guillotine break. To get fast and safe convergence of the simulation 1st order equation was used for transient and discretization, as shown in test condition. The CFD simulation result of pressure change from 7 to 0.3 MPa, which are the prototypic design pressure and scaled down facility pressure was compared with simplified 1D analysis. .

The fluent specification and model used in this calculation are listed as follows:

- Solver
    - Solver : Pressure-Based
    - Time : Transient
    - Pressure Velocity coupling: PISO
    - Transient Formulation : 1st Order Implicit

- Discretization
    - Pressure : Standard
    - Momentum : 1st order upwind
    - Species : 1st order upwind
    - Energy : 1st order upwind

- K-ε standard turbulence

- Species transport model
    - Mixture material: Mixturetemplate
    - 2 species: Air and Helium
    - Density : Ideal-gas
    - Specific heat : mixing-law
    - Thermal conductivity : Ideal-gas-mixing-law
    - Viscosity : Ideal-gas-mixing-law
    - Mass Diffusivity : Kinetic theory
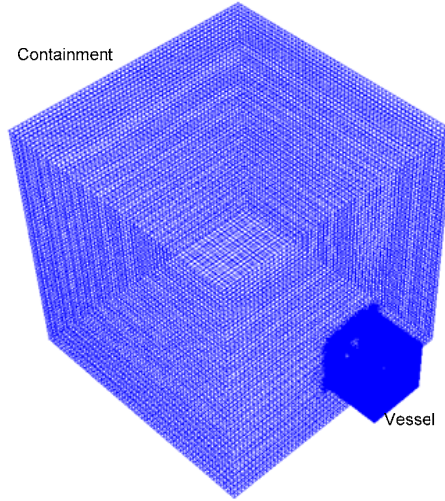
Figure 41. 3D CFD model of simplified prototypic design
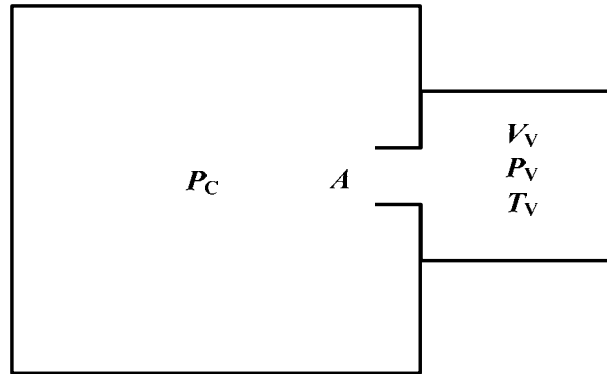
Figure 42. Simplified vessel and containment for 1D analysis

Figure 42 shows the simplified drawing of vessel and containment. A, V, P, and T represent the break area, volume, pressure, and temperature, respectively. The subscript V and C represent the reactor pressure vessel (RPV) and the containment, respectively.

It was assumed that the helium in the vessel expands isentropically and the pressure and the concentration of the gas species are uniform through the vessel and the containment. The time scale of depressurization process is expected to be a fast process, therefore, the heat transfer between that gas and the vessel wall is ignored.

Isentropic flow involves constant entropy, adiabatic and frictionless flow.

$$\left(\frac{T_2}{T_1}\right)^{k/(k-1)} = \left(\frac{\rho_2}{\rho_1}\right)^k = \left(\frac{P_2}{P_1}\right) \tag{35}$$

$$\frac{P}{P_0} = \left\{\frac{1}{1+\left[(k-1)/2\right]Ma^2}\right\}^{k/(k-1)} \tag{36}$$

$$\frac{T}{T_0} = \frac{1}{1+\left[(k-1)/2\right]Ma^2}$$ (37)

$$\frac{\rho}{\rho_0} = \left\{\frac{1}{1+\left[(k-1)/2\right]Ma^2}\right\}^{1/(k-1)}$$ (38)

The mass change in the RPV can be expressed as,

$$\frac{dm_V}{dt} = -\dot{m}_V = V\frac{d\rho_V}{dt} = V\frac{d(P_V/RT_V)}{dt}$$ (39)

$$\dot{m}_V = -\frac{V\rho_{V,t=0}d\left(P_V/P_{V,t=0}\right)^{1/k}}{dt}$$ (40)

$$\dot{m}_V = -\frac{V\rho_{V,t=0}}{K}\left(\frac{P_V}{P_{V,t=0}}\right)^{\frac{1-k}{k}}\frac{d\left(P_V/P_{V,t=0}\right)}{dt}$$ (41)

If the flow is choked, the choking occurs at the location of pipe break *A*. When the pressure inside the vessel, P_V is higher than critical pressure, $P_V{}^*$, the choking occurs. The critical pressure can be expressed as,

$$P_V^* = \frac{P_C}{\left(\dfrac{2}{1+k}\right)^{k/(k-1)}}$$ (42)

The mass flow rate at the break when choked flow

$$\dot{m}_A = A\rho_A v_A = A\rho_V\left(\frac{2}{k+1}\right)^{1/(k-1)}\sqrt{kRT_V\left(\frac{2}{k+1}\right)}$$

$$= AP_V\sqrt{\frac{k}{RT_V}\left(\frac{2}{k+1}\right)^{(k+1)/(k-1)}}$$ (43)

The scaled-down test facility initial pressure is higher than the critical pressure; therefore, the analysis can be solved by choked flow assumption. By applying discharge coefficient, C_d, the mass change inside the vessel, Eq.(41), and the mass flow through the break, Eq.(43), can be express as,

$$\dot{m}_V = C_d\dot{m}_A$$ (44)

$$\dot{m}_V = -\frac{V\rho_{V,t=0}}{K}\left(\frac{P_V}{P_{V,t=0}}\right)^{\frac{1-k}{k}}\frac{d\left(P_V/P_{V,t=0}\right)}{dt} = C_d AP_T\sqrt{\frac{k}{RT_V}\left(\frac{2}{k+1}\right)^{(k+1)/(k-1)}} = \dot{m}_A$$ (45)

$$\frac{d\left(P_V/P_{V,t=0}\right)}{dt} = -C_d\frac{A}{V}\sqrt{k^3RT_{V,t=0}\left(\frac{2}{k+1}\right)^{(k+1)/(k-1)}}\left(P_V/P_{V,t=0}\right)^{\frac{3k-1}{2k}}$$ (46)

$$\left(P_V/P_{V,t=0}\right)^{\frac{1-3k}{2k}}\frac{d\left(P_V/P_{V,t=0}\right)}{dt} = -C_d\frac{A}{V}\sqrt{k^3RT_{V,t=0}\left(\frac{2}{k+1}\right)^{(k+1)/(k-1)}}$$ (47)

$$\left(P_V/P_{V,t=0}\right)^{\frac{1-k}{2k}} = -C_d\frac{A}{V}\sqrt{k^3RT_{V,t=0}\left(\frac{2}{k+1}\right)^{(k+1)/(k-1)}}\left(\frac{1-k}{2k}\right)t + C$$ (48)

$\left(P_{V} / P_{V,t=0}\right)^{\frac{1-k}{2k}}$ is one, when the time, t, is zero. Therefore the pressure change over time is

$$\left(P_{V} / P_{V,t=0}\right) = \left\{1 - C_d \frac{A}{V} \sqrt{k^3 R T_{V,t=0} \left(\frac{2}{k+1}\right)^{(k+1)/(k-1)}} \left(\frac{1-k}{2k}\right) t\right\}^{\frac{2k}{1-k}} \qquad (49)$$

where, ρ, v, A are the density of gas, velocity, and area of the break. Subscript A represents the pipe break location.

The both test was performed with the free volume of containment and pressure vessel are 25,000 and 265 m^3 which are the same as prototypic design. Initially the pressure vessel was filled with 100% helium at 1023K and 7 MPa. The containment was filled with 100% air at 300K and 0.1 MPa. Figure 43 solid black line is a FLUENT result and red star mark is a 1D analysis. The results shows good agreement, therefore, the depressurization process can be assumed as isentropic process and this model can be used to predict the initial pressure and temperature for the OSU experimental facility. By reducing the calculation for the depressurization state, the total CFD computing time would be significantly reduced.
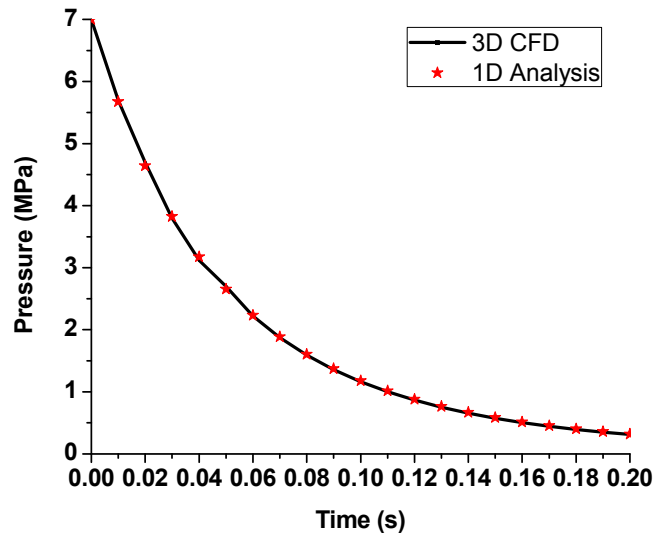
Figure 43. Comparison of depressurization using 3D CFD and 1D Analysis from 7 to 0.3 MPa

Initial condition of the test facility

Previous studies assume that the air-ingress process starts once the inside and outside pressures are equalized. However, the following calculations show the existence of pressure oscillations after blowdown termination.

As shown in Figure 44, the hot duct length is *L* and the discharging cross sectional area is *A*. The amount of mass of the gases in this hot duct section is then *AL* times the density of the air-helium mixture in the hot duct. If the gas mixture travels into the vessel by a small distance *x*, it compresses the gas inside the vessel, so that the volume inside the vessel will become V_0 - *Adx*. Thus, the pressure inside the vessel rises to $p_0 + \Delta p$.

55
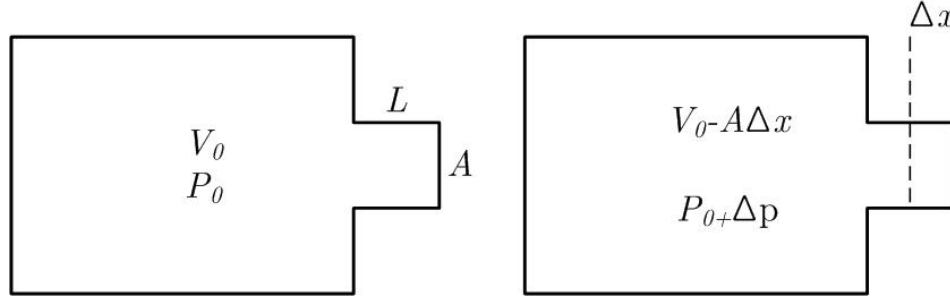
Figure 44. Vessel at equilibrium pressure (left) and at compressed by displacement (right)

Due to the compression being a very fast process, it may be considered as an adiabatic process. Therefore,

$$\frac{\Delta p}{p_0} = -\gamma \frac{\Delta V}{V_0} = -\gamma \frac{A\Delta x}{V_0}, \quad \gamma = \frac{C_p}{C_v},$$ [50]

where V is the duct volume. Applying Newton's law of motion, one has:

$$\frac{d^2 x}{dt^2} = \frac{F}{m} = \frac{\Delta P A}{\rho A L} = -\frac{\gamma A P_0}{\rho V_0 L}\Delta x$$ [51]

$$F = m\frac{d^2 x}{dt^2} = -kx, \quad f = \frac{1}{2\pi}\sqrt{\frac{k}{m}}$$ [52]

Then, the frequency of the oscillations can be calculated as:

$$f(Hz) = \frac{1}{2\pi}\sqrt{\frac{\gamma A P_0}{\rho V_0 L}} = \frac{c}{2\pi}\sqrt{\frac{A}{V_0 L}}, \quad c \text{ is speed of sound}$$ [53]

Therefore, to clarify the effect of the depressurization, pressurized isothermal CFD model was designed. Initially, the vessel and enclosure temperature were set to 300 K and the inside vessel was pressurized to 6 atm while the initial pressure of the enclosure was set at 1 atm.

The fluent specification and model used in this calculation are listed as follows:

- Solver
  - Solver : Pressure-Based
  - Time : Transient
  - Pressure Velocity coupling: PISO
  - Transient Formulation : First Order Implicit

- Discretization
    - Pressure : Standard
    - Momentum : 2nd order upwind
    - Species : 2nd order upwind
    - Energy : 2nd order upwind

- K-ε standard turbulence

- Species transport model
    - Mixture material: Mixturetemplate
    - 2 species: Air and Helium
    - Density : Ideal-gas
    - Specific heat : mixing-law
    - Thermal conductivity : Ideal-gas-mixing-law
    - Viscosity : Ideal-gas-mixing-law
    - Mass Diffusivity : Kinetic theory

Once the pipe break is initiated, the pressurized helium inside the vessel was released to the atmospheric pressure enclosure as shown in Figure 45. After the blowdown termination, pressure oscillations were observed due to the momentum of the depressurized helium. This phenomena causes gas mixing at the break surface. Figure 46 shows the gas mixture velocity at the pipe break after blowdown termination. In the case of 100% air and 100% helium, the frequencies are 78.7 and 205.6 Hz, respectively, according to Eq. (53). This result is in agreement with the CFD calculations. Because the outside of the pressure vessel in the CFD calculations is an air-helium mixture, the frequency in Figure 46 is expected to be between the frequencies of the pure air and the pure helium cases. The frequency is around 120 Hz which falls within the calculated range.
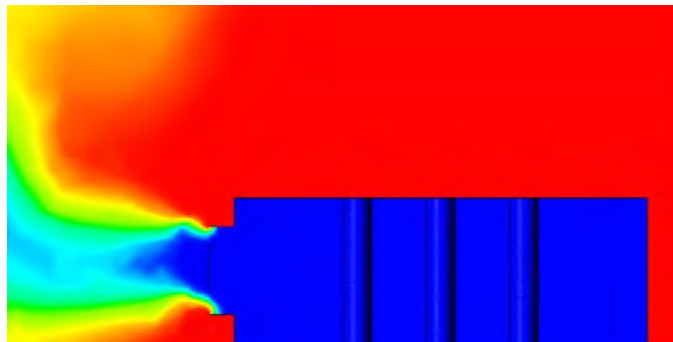
Figure 45. Initial helium blowdown
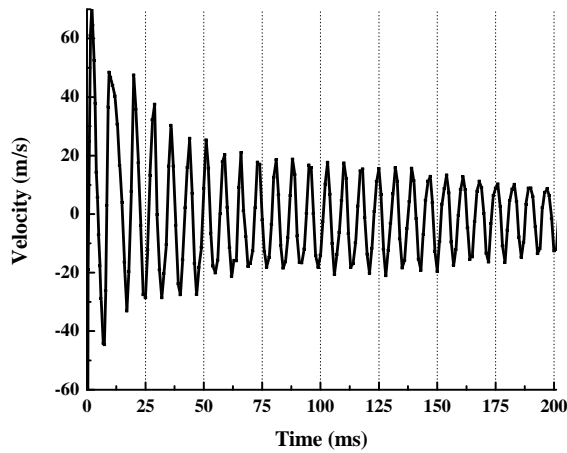
Figure 46. Velocity at the pipe break after blowdown termination

Figure 48 clearly shows the gas mixing due to the pressure oscillation after blowdown. The time of 0 seconds is the starting point when the air-helium mixture enters into the vessel. The right half of Figure 48 is the case where the initial pressure on the inside and outside of the vessel is equalized. In this case, the air-ingress phenomenon was dominated by the density driven flow. Air enters through the bottom of the vessel. However, the left half of Figure 48, which considers the initially pressurized vessel case, shows an additional stage before the density driven air-ingress. Due to the pressure oscillation, Figure 48 (a) and (b) shows the air and helium mixing which differ from the density-driven flow. It shows slightly more air entering into the vessel before the density driven flow starts. Thus, at the beginning of the density-driven air ingress process, the pressurized case has more air in the vessel than in the first case. However, air ingress speed becomes slower eventually as shown in Figure 47

The displacement x in Eq. (50) is determined by the pressure difference between inside and outside of the pressure vessel. When the initial pressure of the vessel is larger, it leads to a larger pressure difference with the outside of the vessel. Thus, at the beginning of the air ingress, more air enters into the vessel due to pressure oscillations when the initial vessel pressure is higher. However, the mixture density in the containment is decreased by the discharged helium, which makes the air ingress slower as time progresses. Because the main driving force is density difference between the outside and inside vessel mixture, the initial air mixing in the pressurized case makes the density difference to be smaller. Thus, it decreases the rate at which air ingresses into the vessel.

58
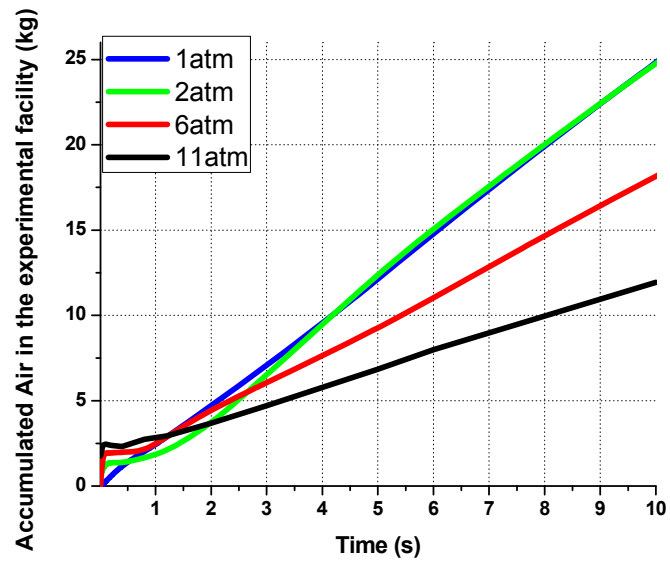
Figure 47. The effect of depressurization
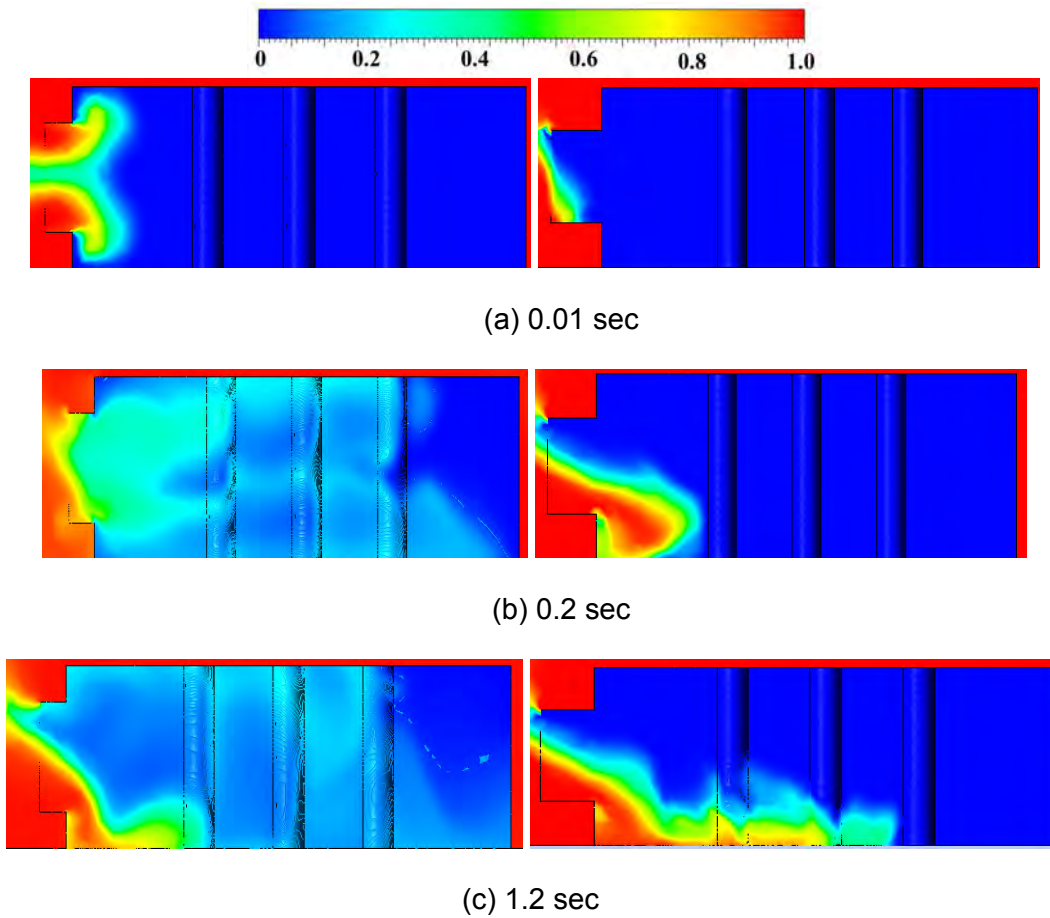
(a) 0.01 sec

(b) 0.2 sec

(c) 1.2 sec

Figure 48. Air mass fraction contour of pressurized (left) and non-pressurized (right)

(d) 2.5 sec

(e) 3.5 sec
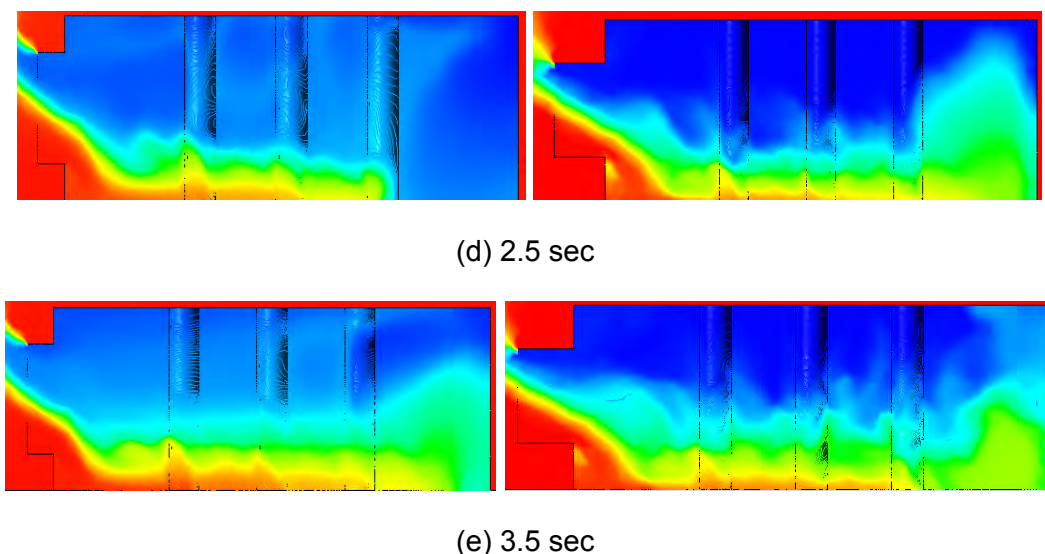
Figure 48. Air mass fraction contour of pressurized (left) and non-pressurized (right) (Continued)

Reactor building design effects

There are two reactor building design characteristics that could influence the air-ingress accident, the reactor building ventilation and multiple compartments. Both designs could limit the air ingress into the reactor

A design feature of the GT-MHR that is different from current commercial nuclear power plants is the reactor building which employs a vented, low-pressure containment. A GT-MHR design report[16] indicates that the reactor building is designed to vent whenever the internal pressure exceeds the external atmospheric pressure by 1 psi. Therefore, if a reactor depressurization process happens, the discharged helium gas will mix with the air in the containment and part of mixture would be vented from the containment. This reduces the amount of air available in the containment that could ingress into the reactor.

The amount of air in the cavity and helium in the vessel are 1016 and 221 kmol, respectively, during normal operation. When the depressurization is terminated, the amount of helium coolant discharged from the vessel is around 200 kmol. If the ventilation is considered, the same amount of helium-air mixture would be discharged to the outside containment. If the discharged gas is assumed 100% air, there is 20% less air that could ingress into the reactor.

To study the containment ventilation effect, a simplified 3D CFD calculation was performed. Figure 49 shows the simplified 3D CFD model. Instead of using the prototypic geometry, a regular hexahedron design with conserved volume was used same as Figure 41. Since the vent location and size of the GT-MHR are not given in the design report, a case study was performed with three different ventilation locations as shown in Figure 51. Vent in Figure 51.(a) faces to the reactor vessel breach with higher elevation, vent in Figure 51.(b) faces to the breach and same elevation, and vent in Figure 51.(c) located at the same elevation as (a) without facing the breach.
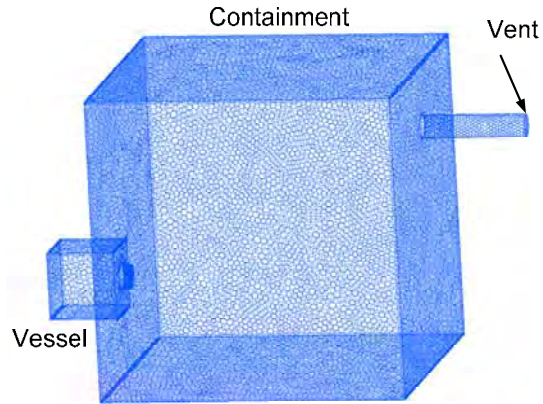
Figure 49. CFD model of volume conserved with ventilation at top right

(a) 0 sec   (b) 0.09 sec   (c) 0.27 sec

(d) 0.4 sec   (e) 1.15 sec   (f) 2.61 sec
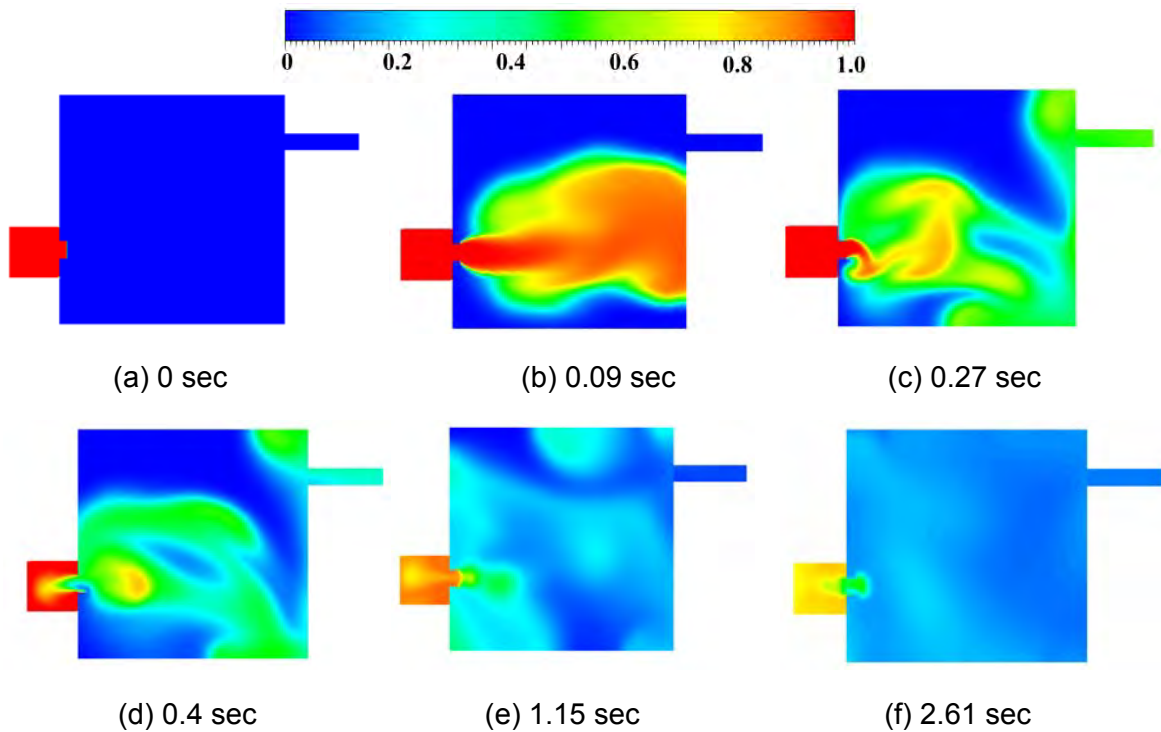
Figure 50. Contour plots of helium mole fraction at various times into the accident

Figure 50 shows calculation results of the vent located at the top right of the containment. Initially, the reactor pressure vessel was filled with 100% helium at 1023 K and 7 MPa. The containment was filled with 100% air at 300 K and 0.1 MPa. The boundary condition of the vent was set to 'pressure outlet' with 300 K and 0.1 MPa. Figure 50 (a) shows that the air and helium are initially separated in the containment and vessel. When the depressurization is initiated, the helium is discharged as shown in Figure 50 (b). The discharge continues to fill until the pressures inside the vessel and the containment are equalized. Figure 50 (c) represents the point at which the pressures are equalized. At this time, 0.27 seconds after initiation of accident, 0.33% of air and 1.22% of helium were released to atmosphere. During the early stage of the depressurization, the discharged helium is not well mixed as shown in Figure 50 (b)-(d).

Therefore, the discharged mixture concentration is determined by the mixture concentration at the vent location. As shown in Figure 52, case (a) and (b) release more helium than air. At the beginning of the depressurization, discharged helium directly hit the wall; therefore, case (a) and (b) have higher increase at the beginning of the accident. On the other hand, case (c) does not discharge helium until the helium–air mixture reaches to the vent located top left of the containment.

(a) top right   (b) bottom right   (c) top left
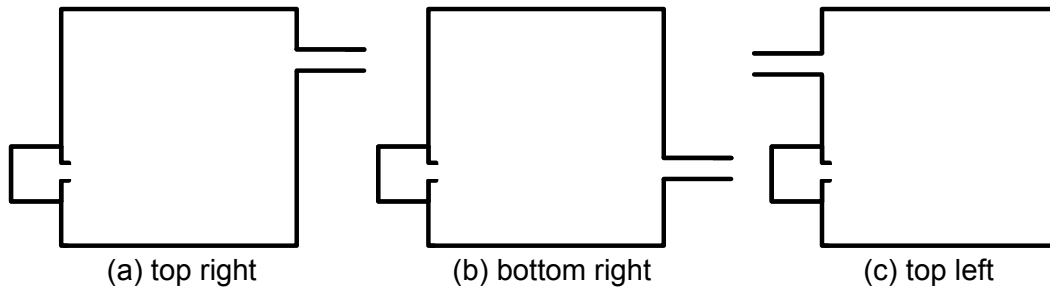
Figure 51. Various ventilation locations
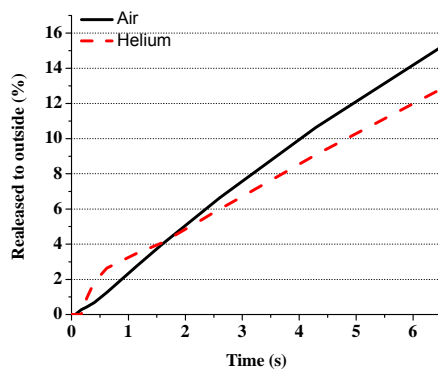
(a) top right
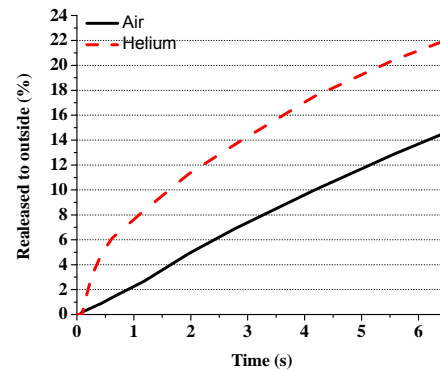
(b) bottom right
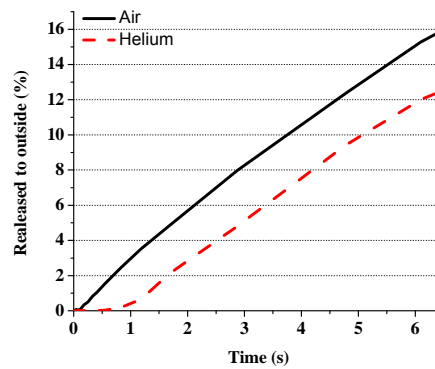
(c) top left

Figure 52. Percentage of released gases to atmosphere

Figure 53 shows the changes of air mole fraction in the volume of reactor building. It combines reactor vessel and containment. It shows the vent located at the bottom right gives higher air

mole fraction due to the initially discharged helium during the depressurization process. However, the air mole fraction change from the initial stage is less than 1% which is quite lower than 100% air or 100% helium discharge case.   Even though the vent size would affect the air concentration change, which is the same vent as the double-ended guillotine break; therefore, the vent size and location would not affect much on the density change.
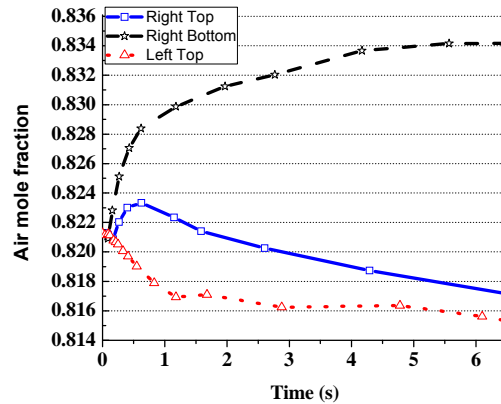
Figure 53. Air mole fraction change due to the ventilation locations
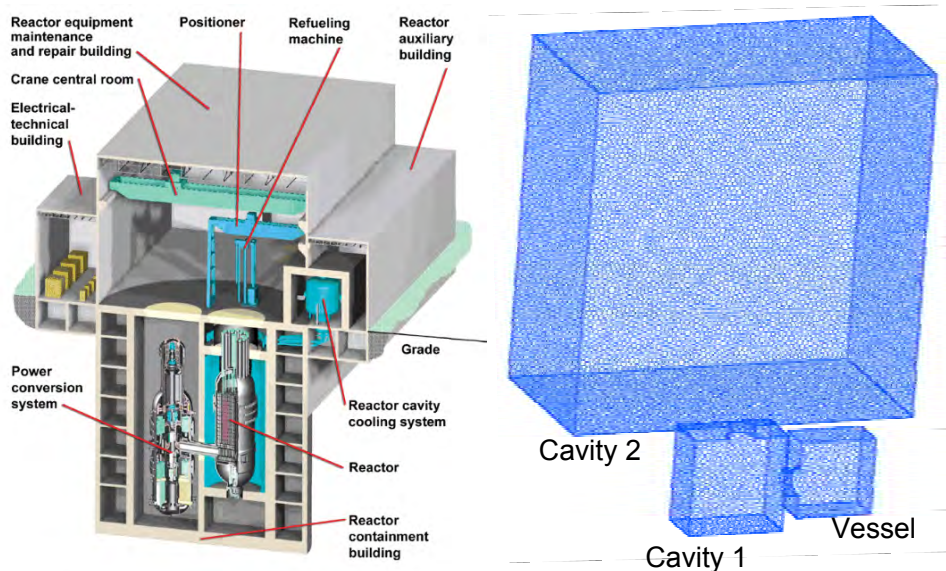
Figure 54. GT-MHR below grade installation[15] (left) and geometry of CFD model (right)

Figure 54 left shows the reactor building that has multiple compartments. Even though there are multiple compartments, it was not considered in previous analyses.   Because each compartment is not air sealed and the compartments are connected to each other as shown in Figure 54, the fluid could easily flow to other compartments. However, once the guillotine break of the cross vessel is initiated; the discharged helium would fill the compartment where the breach is located and move the air to other compartments. Because the break location is low to the ground, air would move back to the lower compartment so that the air could ingress to the reactor vessel. However, the available air would be limited by the compartment structure design. Therefore, a simplified CFD model of compartmentalized containment was made as shown on

the right side of Figure 54. The containment is divided into two parts, namely, Cavity 1 and 2. The volume of Cavity 1 and Cavity 2 were set to 530 and 24,470 m^3, respectively. It was assumed that the flow through the opening of the cross vessel during a double-ended guillotine break case would be preferred for flowing into the other compartment. The discharged helium from the reactor pressure vessel would fill the cavity volume outside the vessel and PCU first. Therefore, the cavity volume of the reactor vessel and PCU were combined into Cavity 1. The Cavity 2 volume was set so that the total containment free volume is 25,000 m^3. To examine the effects of the compartment design, the ventilation is not considered in this simulation. The flow path between each compartment was set to 2.24 m^2.
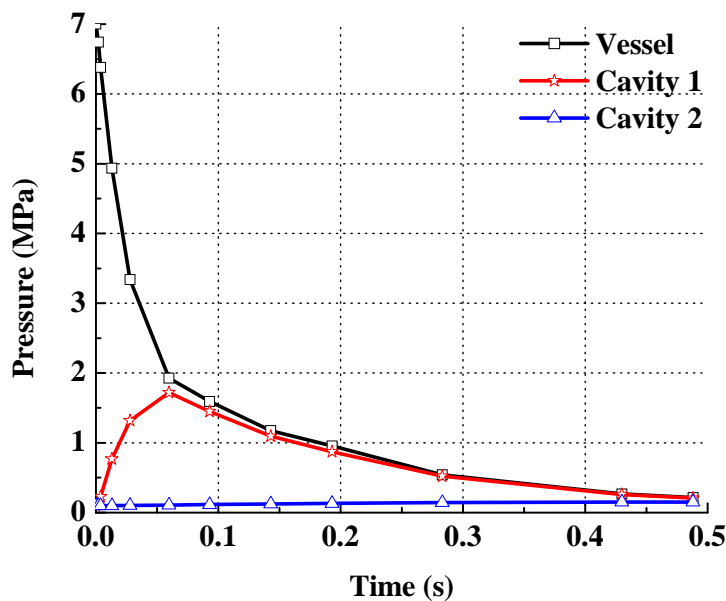
Figure 55. Pressure changes in each compartment

Initially, cavities 1 and 2 were filled with 100% air at 0.1 MPa and 300 K and the vessel was filled with 100% helium at pressure of 7 MPa and temperature of 1023 K. Once the double-ended guillotine break of the cross vessel is initiated, the discharged helium starts to fill Cavity 1 and the pressure in Cavity 1 increases as shown in Figure 55. As the pressure in Cavity 1 becomes close to the pressure in the vessel, the depressurization process slows down. Therefore, the depressurization takes more time than the previous single containment numerical model.

The contour plot in Figure 56 shows qualitatively how much air in Cavity 1 flows into Cavity 2. As the process proceeds, the discharged helium mixes with air in Cavity 1. At about t=0.5 sec, the depressurization process comes to a close and almost no air is left in cavity 1.
The compartmentalized containment numerical model results show that the amount air left in Cavity 1 is less than 10% of the initial amount. Even though some of the air in Cavity 2 would move into Cavity 1 as shown in Figure 56(j) because the relative location of cavity 1 is below cavity 2, the compartmentalized containment model incredibly reduces the amount of air that could ingress into the reactor vessel

(a) 0 sec   b) 0.05 sec   c) 0.1 sec

e) 0.2 sec   f) 0.3 sec   g) 0.4 sec

h) 0.5 sec   i) 0.6 sec   j) 0.7 sec
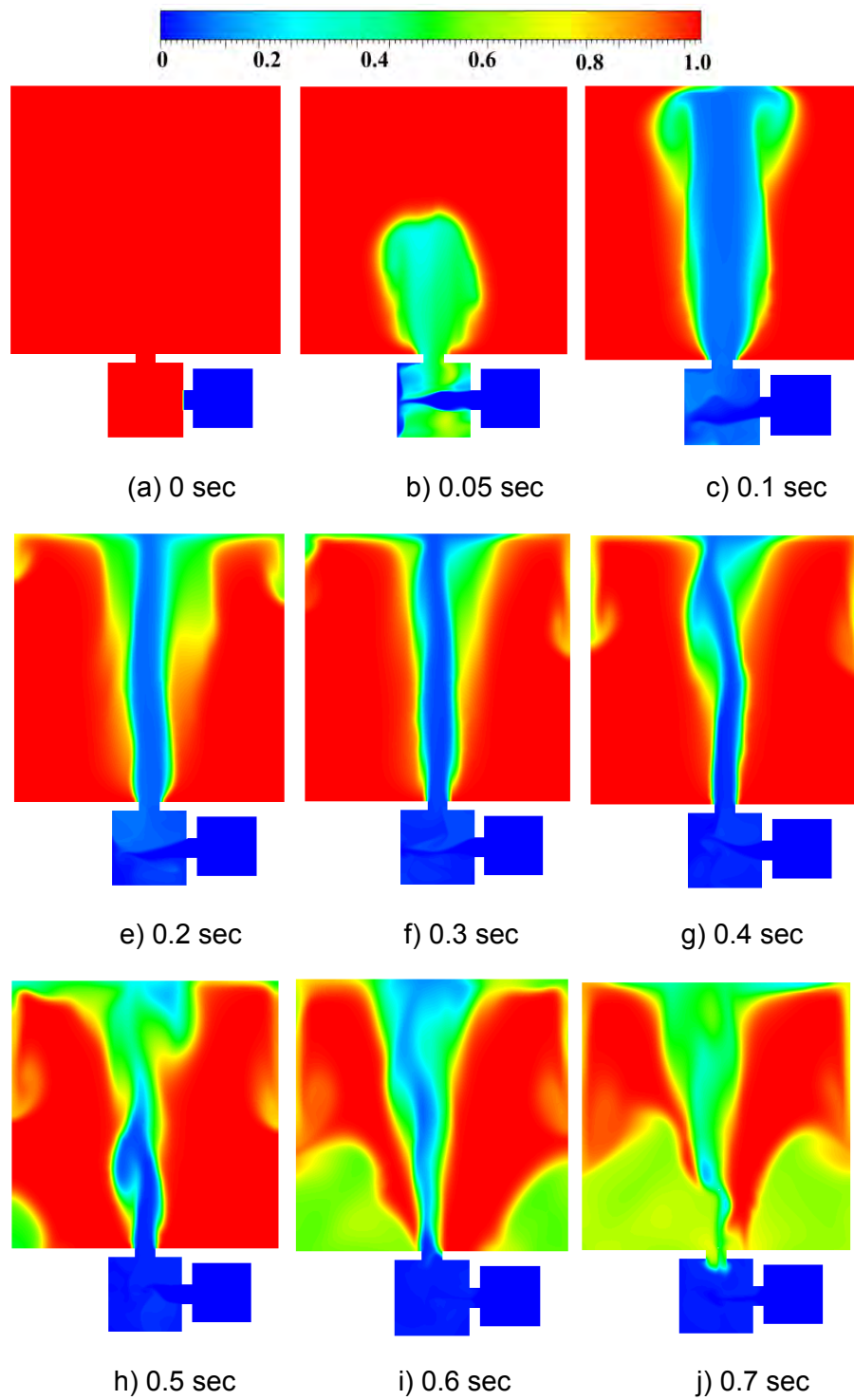
Figure 56. Contour plot of air mole fraction

<u>Air-Ingress Mitigation Method</u>

The air-ingress accident may lead to degradation of graphite structure by oxidation and, in extreme cases; a loss of structural integrity may occur and lead to release of radioactive materials. Even though the compartmentalized containment study showed significant amount of air removed from Cavity 1, air would flow into Cavity 1 and the reactor pressure vessel eventually. Therefore, a mitigation method is studied for the compartmentalized containment numerical model.

In the compartment design, the vessel is located at a relatively lower level as compared to the rest of the connected free volume so that air will accumulate to the Cavity 1 and eventually air-ingress would be initiated. The simulation was started with the vessel and cavity 1 filled with 100% helium and cavity 2 with 100% air. As time goes on, it can clearly be seen that air flows to another compartment. Figure 57 shows the air flows into Cavity 1 and reactor pressure vessel.

Yan[22] injected inert helium gas at the top head of reactor vessel and Oh[23] injected helium gas at the bottom of the lower plenum for air-ingress mitigation measure. The injection location was decided based on the protection priority, but both cases could control the air ingress well. Oh also suggested additional confinement surrounding the reactor vessel; however, this design would degrade the passive cooling of VHTR by RCCS. In addition, helium needs to be continuously injected until the internal temperature is cooled down so that there is no graphite oxidation. Yan and Oh indicated that it would be 3 months and 6 days, respectively.

Argon gas injection into Cavity 1 is applied in this study. There are five candidate inert gases for injections as summarized in Table 12. Among the five inert gases, Argon is heavier than air and the price is reasonable to use for injection.

Table 12. Proposed inert gas for injection

	Atomic number	Density (kg/m^3)	Price ($/m^3)
Helium	2	0.16	8.34
Neon	10	0.81	1,617.20
Argon	18	1.60	8.01
Krypton	36	3.37	1,110.78
Xenon	54	5.89	7,072.00

Figure 56 shows after depressurization, the cavity next to the reactor vessel would be filled with helium discharged from the reactor vessel. Therefore, a CFD simulation was performed with 100% helium in the vessel and Cavity 1 at 0.1 MPa and 1023 K and the Cavity 2 was filled with air at 0.1 MPa and 300 K. Even though the air ingress speed would change depending on the size of the flow area and location, Figure 57 clearly shows that this accident scenario could be expected.

By injecting argon in Cavity 1, the density of the gas mixture in Cavity 1 will be increased. When the mole fraction of Argon is greater than 0.7, the density of the mixture is heavier than air. As shown in the Figure 58, the density difference between Cavity 1 and Cavity 2 for the injected case decreases. Therefore, even though the injection is stopped, the density driven flow from Cavity 2 to Cavity 1 would be slowed down.

(a) 0 sec   (b) 10 sec   (c) 15 sec

Figure 57. Contour plot of air mass fraction (no injection)
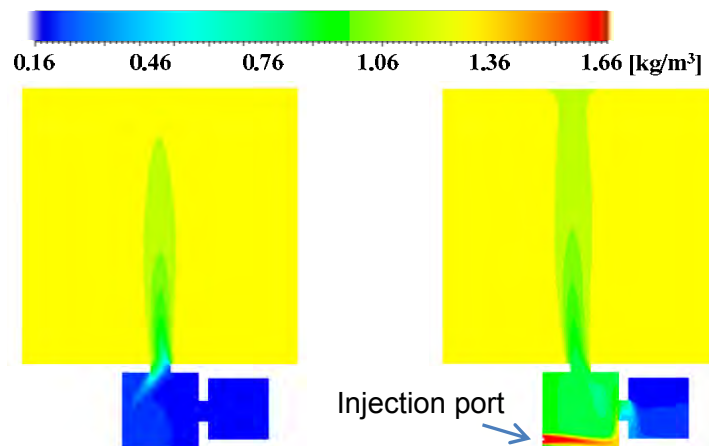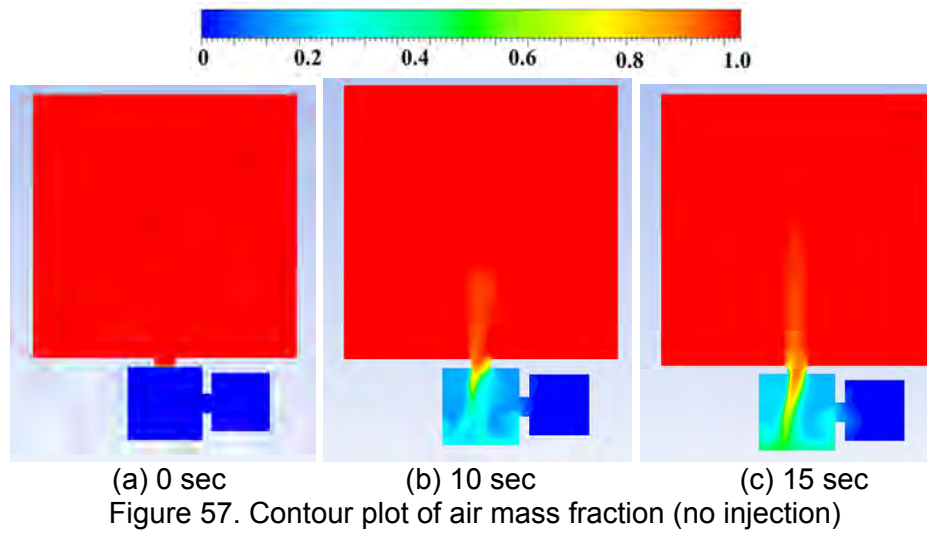
Figure 58. Contour plot of density (kg/m^3) at 25 sec - no injection (left) and injection (right)

(a) 1kg/s   (b) 2kg/s   (c) 10kg/s

Figure 59 Contour plot of air mass fraction (Argon gas injection) at 15 sec

67
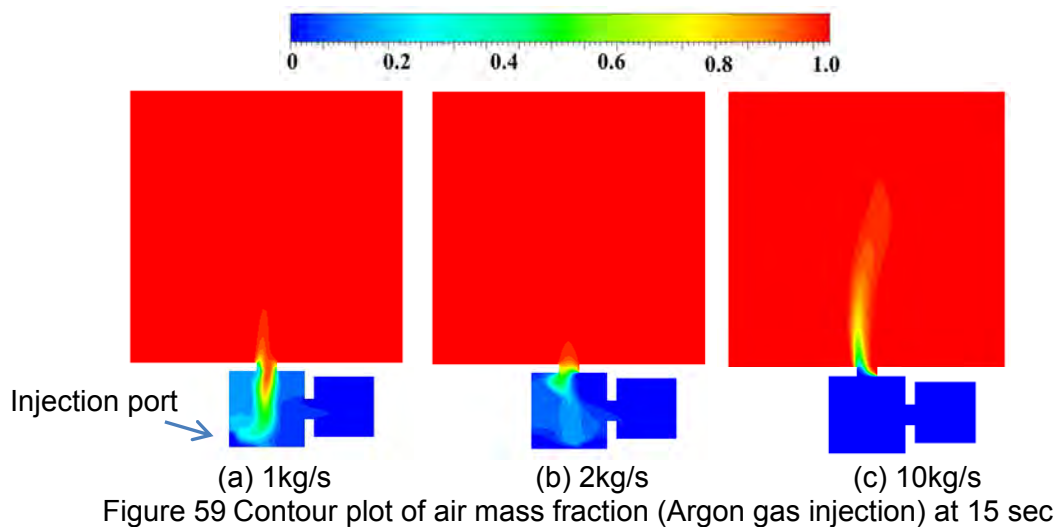
When the argon mole fraction in argon-helium mixture at room temperature is greater than 0.7, the mixture density is greater than air. The amount of argon required fill the Cavity 1 is 1.4 ton. To investigate the effect of the injection rate, CFD simulation was performed. Argon gas was injected through the bottom of Cavity 1 horizontally with three different mass injection rates were applied: 1, 2, and 10 kg/s. Figure 59 shows the results of three different injection rates at 15 sec after the initiation. As the injection rate increases, the air flow from Cavity 2 decreases due to the Cavity 1 is pressurized by argon injection. In addition, by injecting Argon gas, the density of the gas mixture in Cavity 1 increases. The simulations, utilizing argon injection in the cavity vessel as a mitigation strategy for the air-ingress accident, can be validated on the scaled-down test facility. The argon injection rate on the scaled-down test facility can be properly scaled to simulate how this phenomenology would develop on the prototypic design.

Two-dimensional Heat Transfer Support Column Transient Analysis

In addition to the one-dimensional analysis above, a two-dimensional analysis was also performed. The major difference between the current analysis and the 1-D transient analysis is that the current analysis takes a heat source into consideration. More specifically, the current analysis looks into the heat conducted in and out of the support column in the axial direction. Mathematically, this is demonstrated by imposing fixed temperature boundary conditions at the top and bottom boundaries of the support column. The governing equation that is solved is the transient two-dimensional heat diffusion equation for cylindrical coordinates. Mathematically,

$$\rho c_p \frac{\partial T}{\partial t} = \frac{1}{r}\frac{\partial}{\partial r}\left(kr\frac{\partial T}{\partial r}\right) + \frac{\partial}{\partial z}\left(k\frac{\partial T}{\partial z}\right); \; r_1 \le r \le r_2; \; t \ge 0 \quad [54]$$

For cases (1) - (3) as defined in the 1-D analysis, the boundary conditions are given in Table 13.

Table 13. Boundary Conditions for Two-dimensional Analysis

Case	Top Boundary Condition	Bottom Boundary Condition	Left Boundary Condition	Right Boundary Condition
1			$\left.\frac{\partial T}{\partial r}\right|_{r=0} = 0$	
2	Fixed Temperature (750°C)	Fixed Temperature (750°C)		$-k_s\left.\frac{\partial T}{\partial r}\right|_{r=r_2} = h\left(T(r=r_2,z,t)-T_\infty\right)$
3			$-k_s\left.\frac{\partial T}{\partial r}\right|_{r=r_1} = q''_{heater}$	

Similarly, the support column physical dimensions, total time scale, and heat transfer coefficient are given in. Heat transfer coefficients are the largest values from Figure 23 andFigure 24, respectively. Total time scale is calculated according to the method shown in Arcilesi et al.[17]

The governing equation is discretized using a finite volume discretization and explicit time-marching scheme. The stability is ensured by taking Δt to be 0.2 of Δt$_{max}$ where

$$\Delta t_{max} = \frac{1}{2\alpha\left(\frac{1}{\Delta r^2} + \frac{1}{\Delta z^2}\right)} \quad [55]$$

and α is the largest thermal diffusivity of IG-110 graphite over the range of 20 – 800°C. This yields that smallest Δt_{max}. The largest value occurs at 20°C and equals 1e-4 m^2/s. The mesh size and corresponding Δt_{max} are shown

Table 14. Support Column Dimensions, Total Time Scale, and Heat Transfer Coefficient for Two-dimensional Analysis

Case	Support Column Inner Radius, r_1 (m)	Support Column Outer Radius, r_2 (m)	Support Column Height, H (m)	Total Time Scale, τ (s)	Heat Transfer Coefficient, h (W/(m^2 K))
1	0	0.106	2.84	16.06	12.69
2		0.0275	0.3556	5.67	15.57
3	0.0148				

Table 15. Mesh Size and Time Step for Two-dimensional Support Column Heat Transfer Analysis

Case	Number of Cells in Radial Direction	Number of Cells in Axial Direction	Δr (m)	Δz (m)	Δt_{max} (s)	Δt (s)
1	40	1000	0.0027	0.0028	0.0188	0.0038
2	40	200	6.875e-4	0.0018	0.0021	4.112e-4
3	20	200	7.400e-4	0.0018	0.0023	4.668e-4

Using this method, temperature contour plots have been generated for cases (1) – (3) at time t = 3τ. To simplify comparison, the radial and axial direction (or x- and y-axis) have been normalized with respect to that particular case's column geometry. It should be noted that the far-field temperature is 25°C. Also, the thermal conductivity and specific heat capacity are non-constant. Correlations were derived from data in the available literature.[13]
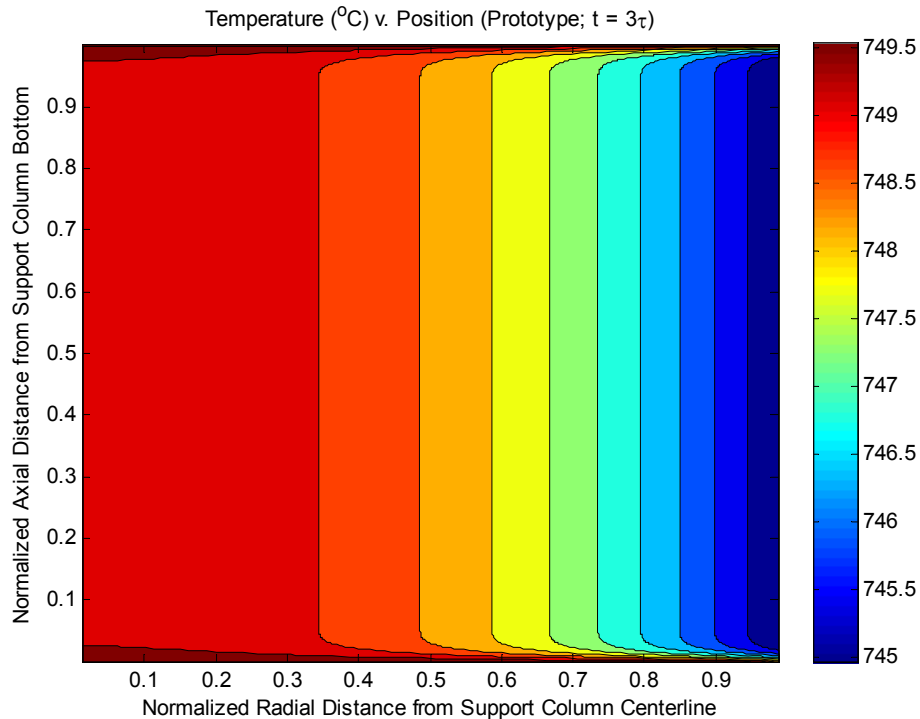
Figure 60. Temperature contour plot for prototype Geometry at t = 3τ
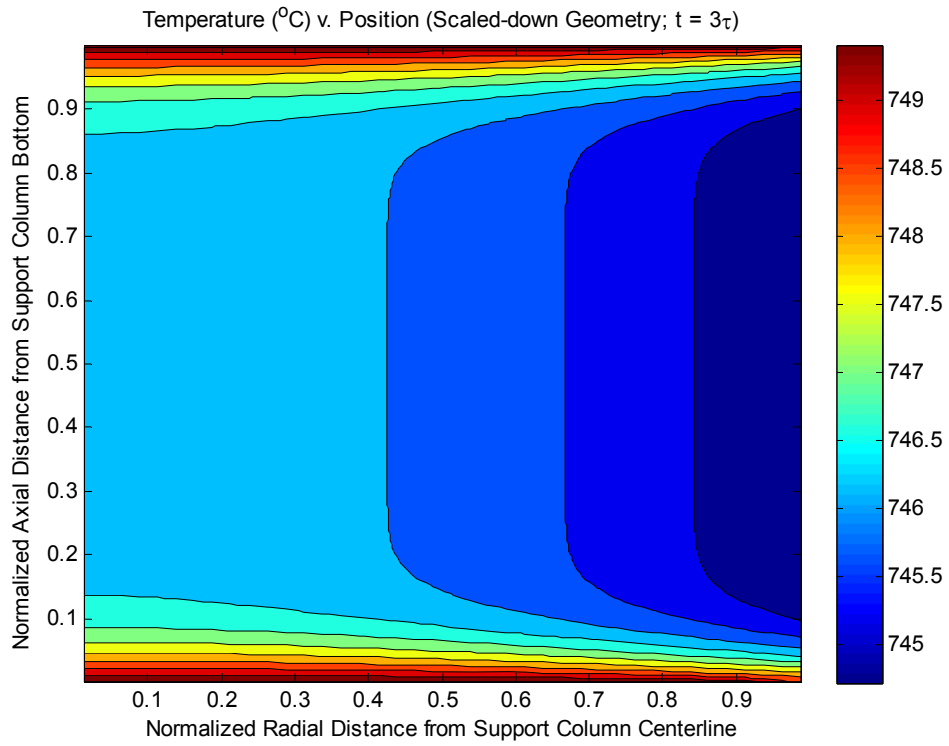
Figure 61. Temperature contour plot for prototype Geometry at t = 3τ
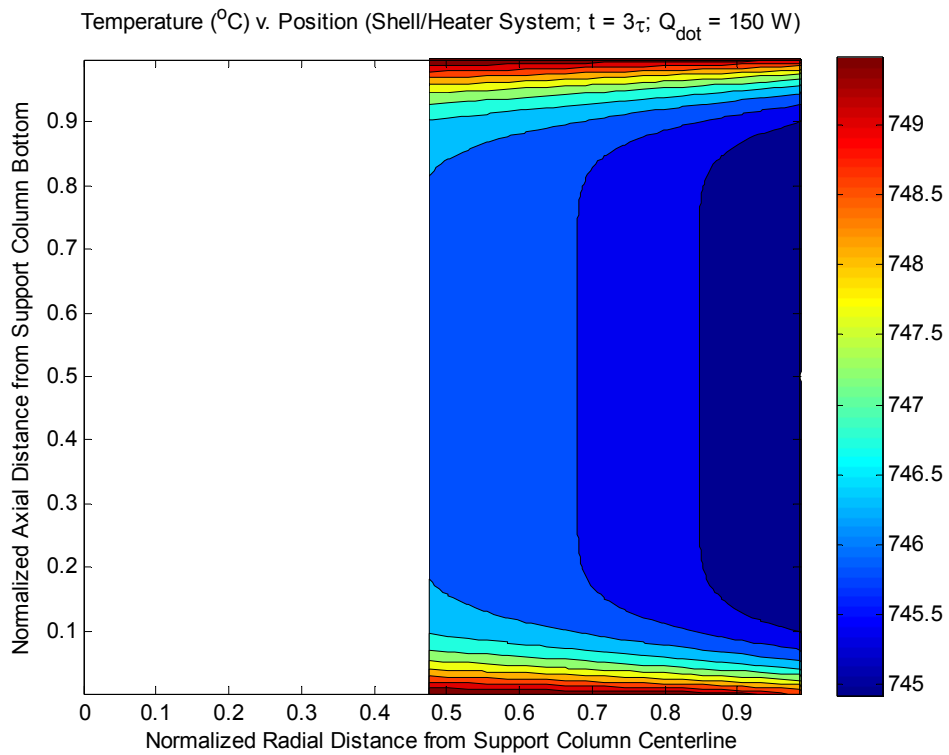
Figure 62. Temperature contour plot for shell/heater system for 150 W at t = 3τ
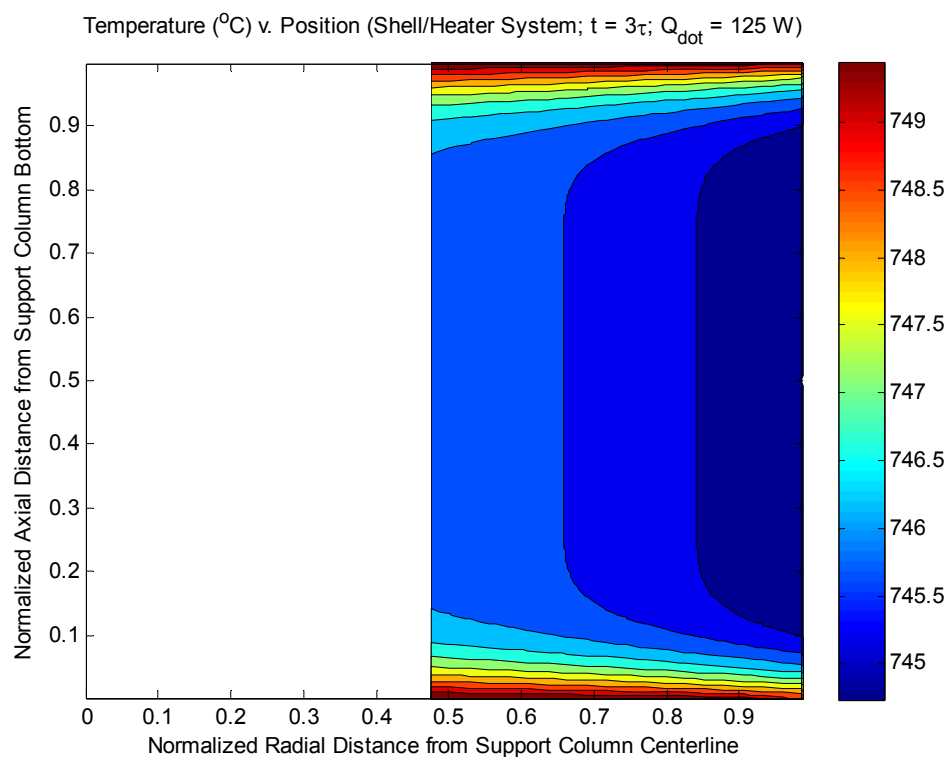
Figure 63. Temperature contour plot for shell/heater system for 125 W at t = 3τ
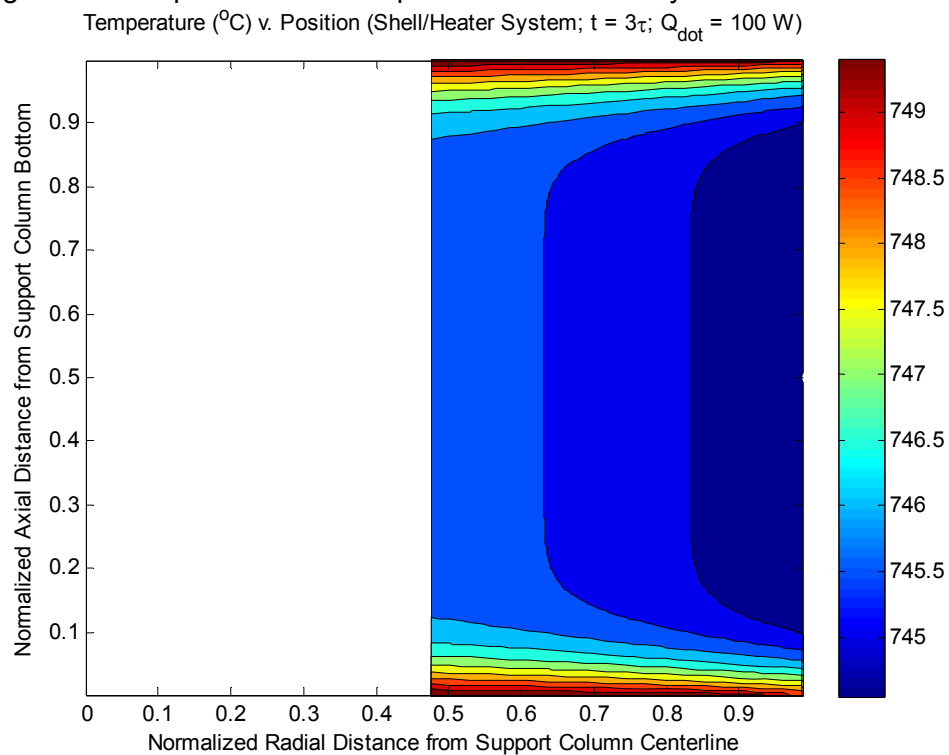
Figure 64. Temperature contour plot for shell/heater system for 100 W at t = 3τ
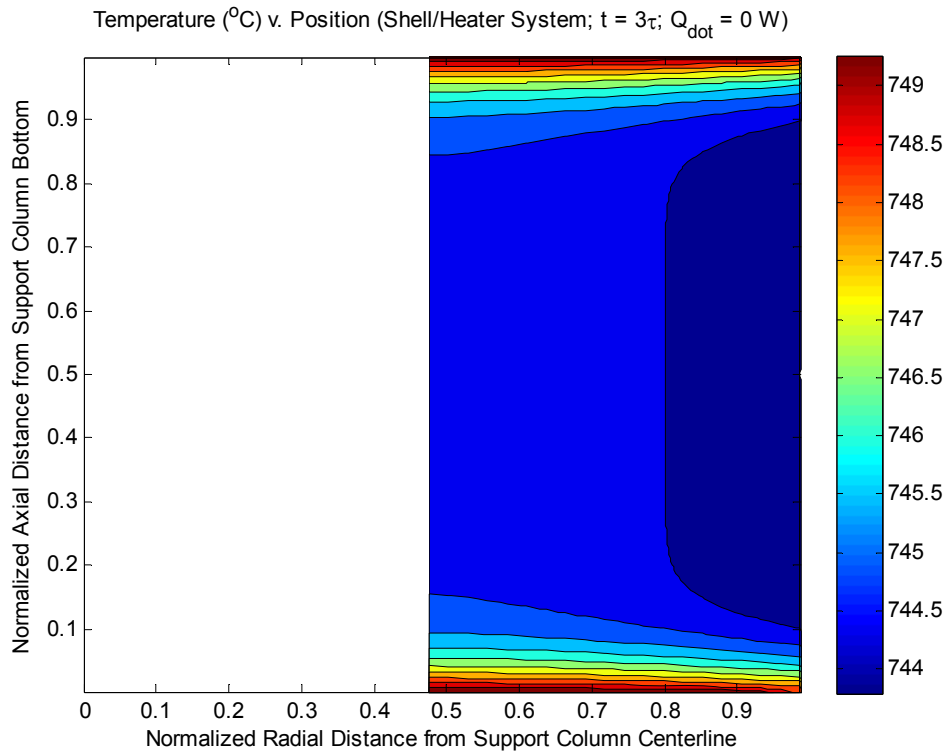
Figure 65. Temperature contour plot for shell/heater system for 0 W at t = 3т

The results of these calculations are promising. At first glance, the general temperature gradient in the radial direction for all four cases is similar. Therefore, the heat flux emitted from the support column surface for all six cases is similar since the thermal conductivity is nearly identical for all six cases. Also, the surface temperature for a majority of the support column for all six cases is within one degree celsius. Outside the center majority region, the surface temperature does not increase more than five degrees celsius. Since the surface temperatures are within a couple of degrees celsius, the natural circulation phenomenology will be preserved from a heat source point of view. It's interesting to note that even if no power is pushed through the heater in the shell/heater system, there's still very good heat transfer similarity at t = 3т. However, by inspection, the temperature profile of the shell-heater system is most similar to the temperature profile of the prototype and scaled-down support columns when the heater is emitting 125 W.

3. Test Facility Design

With most of the physical dimensions of the scaled-down test facility known, a preliminary design can be assembled. In Table 16, the known critical dimensions for the test facility are listed.

72

Table 16. Critical dimensions for the test facility

Component Dimension	Dimension Size (cm)
Duct Length	10.00
Duct Inner Diameter	18.75
Support Column Diameter	5.50
Support Column Pitch	9.4
Vessel Inner Diameter	85.00
Vessel Inner Height	35.50

Figure 66 is an overhead drawing of the test facility with the critical dimensions filled in. Currently, vendors are being consulted to discuss the viability of constructing such an apparatus. In the current design, flat blind flanges will be used to cover the top and bottom openings of the vessel. The vessel design temperature is 750 °C and design pressures ranging from 30 psi to 150 psi are being considered. Alloy 800H and Stainless Steel 617 are the two materials that are being considered for construction of the vessel. A technical challenge associated with the construction of this vessel is the thickness required for each blind flange to withstand the high pressure and temperature. This is why a final material and design pressure have not been decided.
Table 17 shows the required vessel wall thickness at for different materials and pressures.

Table 17. Vessel wall thickness for 800H and SS 617 for different pressures at 750°C

Pressure (psig)	Vessel Wall Thickness Alloy 800H (in.)	Vessel Wall Thickness SS 617 (in.)
150	0.874	0.419
75	0.430	0.208
30	0.171	0.083

The design material for the support columns would be IG-11 graphite. To achieve the high temperatures, some support columns will be inserted with cartridge heaters. Vendors have been contacted for this material.

Table 18. Top and bottom cover thicknesses for 800H and SS 617 for different pressures at 750°C (without edge moment considerations)

Pressure (psig)	Blind Flange Thickness Alloy 800H (in.)	Blind Flange Thickness SS 617 (in.)
150	4.125	2.880
75	2.917	2.037
30	1.845	1.288

In the second overhead drawing shown in Figure 67, there is a laser port showing where planar laser-induced flourescence (PLIF) could be used to take measurements. There are two locations. The first area is near the duct and would simulate "developing" flow conditions. The

second area is near the middle of the vessel and would simulate "fully-developed" flow conditions. The camera ports would be located on the top cover directly above the areas shown in the sketch. If the use of PLIF proves not to be feasible, the vessel can be fitted with other forms of instrumentation such as pitot tubes, thermocouples, and O_2 sensors.
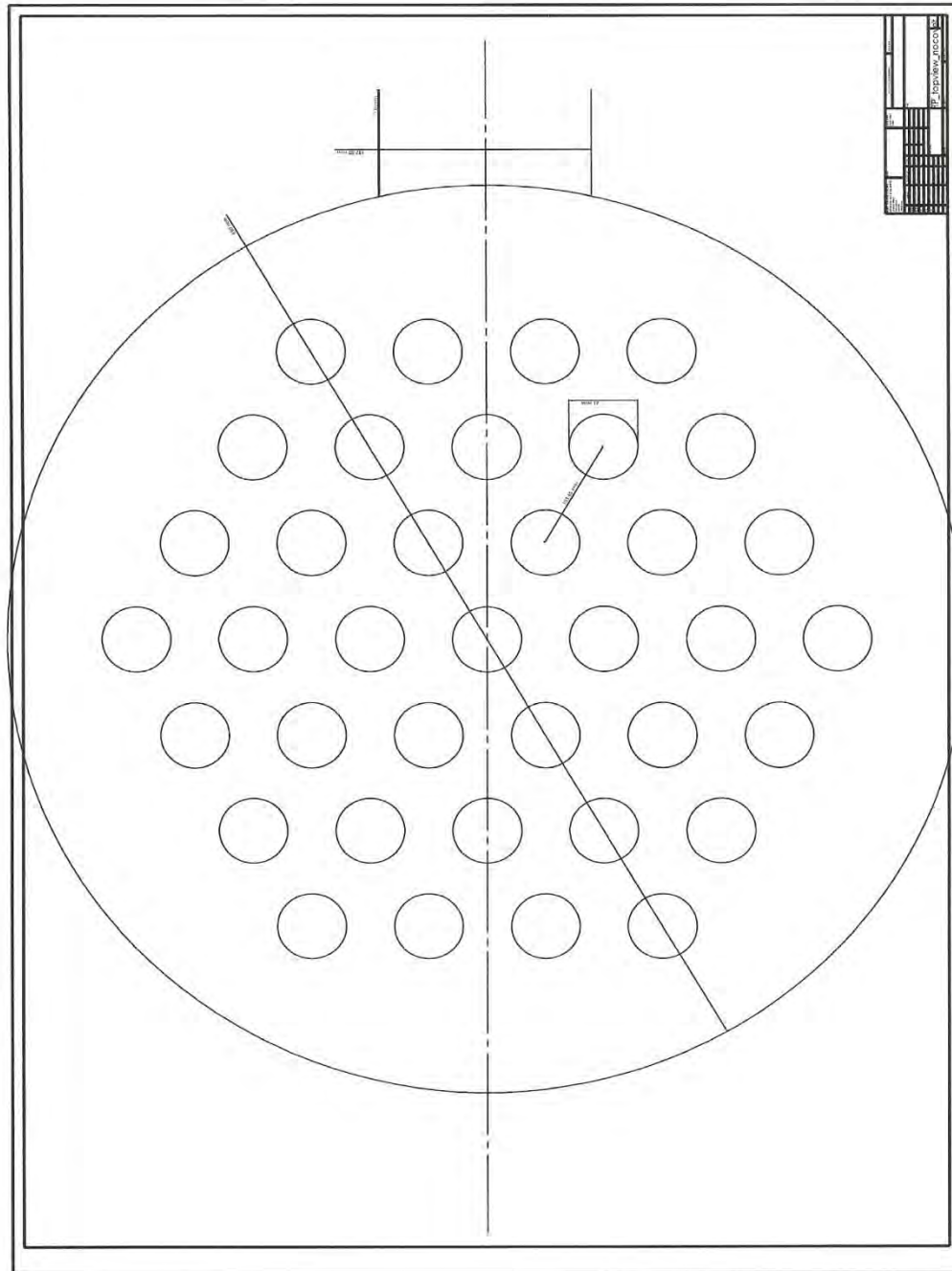
Figure 66. Overhead view without cover with design specifications
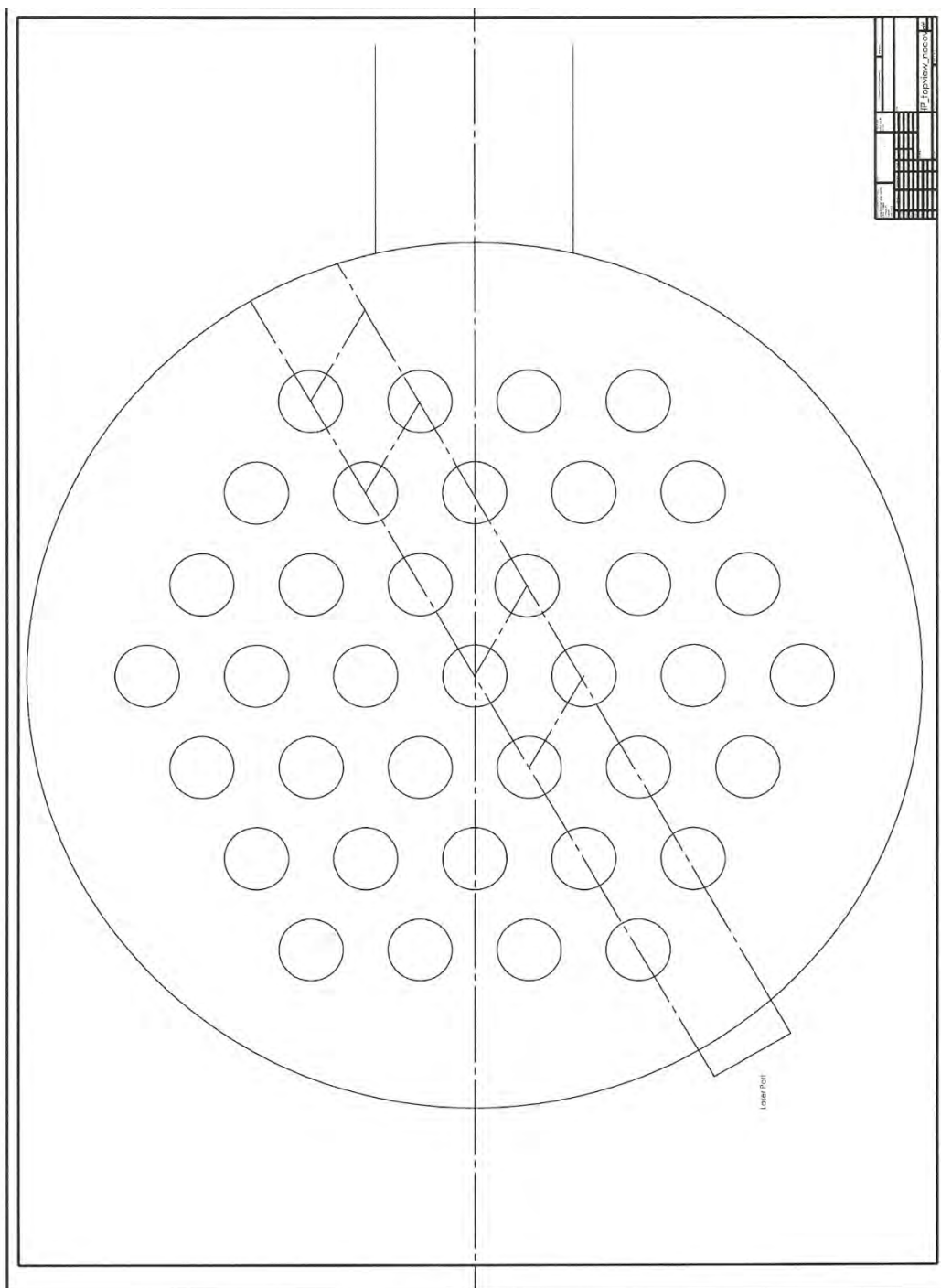
Figure 67. Overhead view without cover with PLIF laser port

Instrumentation

Instrumentation is essential to any experiment. In the following paragraphs, the instrumentation and its location for the air ingress test facility will be discussed. There are four different parameters that will be measured in the facility –pressure, temperature, oxygen concentration and flow. To measure pressure in the vessel, Honeywell Pressure (Gage) Transmitters will be used. For temperature measurements, thermocouples constructed by OMEGA will be used. Intrusive oxygen concentration instrumentation suitable for the current application has been a challenging technical issue. An extensive search was performed to find the best candidate for the experimental facility. To date, the search has been narrowed to three candidates. A discussion of all possible candidates and reasons why they were eliminated will be given in this report. Non-intrusive methods for measuring oxygen concentration were also explored and will be utilized in the proposed setup. To make flow measurements, traditional methods were considered such as differential pressure flow meters and thermal anemometers. However, due to the low-flow conditions, there's not enough differential pressure generated for DP flow meters to generate a signal. Furthermore, due to the high temperature and transient concentration and temperature conditions, thermal anemometry becomes very difficult, if not impractical, to use. Therefore, the best option to measure flow conditions for high-temperature, low-flow conditions is through particle image velocimetry.

Pressure

As indicated previously, the pressure transmitters to be used in the experimental facility is the Honeywell ST 3000 Pressure (Gage) Transmitter – Model STG944. The sensor specifications are given in Table 19.

Table 19. Sensor Specifications (*See design drawings for exact location)

Pressure Range	Temperature Range	Output Range	Frequency Response	Sensor Location*	Costs
0-500 psi	-40 – 110°C	4 – 20 mA	350 ms (Analog mode)	#1	$1,519.00

Temperature

As indicated previously, the temperature measurements will be taken by thermocouples built by OMEGA. The thermocouples are the Super OMEGA XL Thermocouple Probes. These are grounded, Type N thermocouples. The sheath is constructed of Inconel 600 and Ni-Cr Alloy. Other specifications are given in Table 20.

Table 20. Sensor Specification (*See design drawings for exact location)

Temperature Range	Tolerance (whichever is greater)	Response Time	Sensor Location*	Costs
Up to 1150°C	1.1°C or ±0.40%	1.1 s	#3	$34.00

<u>Oxygen Concentration</u>

Manyoxygen probe sensors were considered for this application; most of which were zirconium oxide probe sensors. Table 21 contains a list of oxygen sensors that were considered for the experimental facility.

Table 21. Oxygen sensors considered for test facility

No.	Oxygen Sensor Make/Model
1	Econox/Carboprobe HT
2	Econox/Carboprobe DS
3	Econox/LT Probe
4	Bosch/Automotive Sensor
5	Ametek, Inc./WDG-INSITU
6	General Electric/FGA-311
7	Bhoomi/BI 2000
8	Datatest/Model DT 3000
9	Yokogawa/ZR202G
10	Yokogawa/ZR402G
11	United Process Controls/CS 87
12	United Process Controls/Oxyfire
13	Rosemount/In Situ Oxymitter
14	Preferred Instruments, Inc./Model ZP
15	Land Instruments/WDG1200
16	Land Instruments/WDG1210
17	Honeywell/MF020
18	Honeywell/GMS-10 RVS Series
19	Honeywell/KGZ-10 Series
20	Forney/ZR-22
21	Air Instruments & Measurements, LLC/Model 3600

The temperature range of interest for the proposed experiments is 200 - 750°C. Therefore, the ideal oxygen sensor will have a sample gas temperature range that covers the 200 - 750°C. In addition, sensors with quick response times and small minimum insertion lengths are preferred. That way, many readings may be taken over the time scale of the transient (which is approximately 15 s) and close to the boundary of the test section. Table 22 gives a brief analysis of the feasibility of each sensor.

Table 22. Feasibility analysis of oxygen sensor candidates

No.	Status	Reason (if not acceptable)
1	Not Acceptable	Sample gas temperature range too high (550-1700°C)
2	Not Acceptable	Sample gas temperature range too high (550-1700°C)
3	Acceptable	N/A
4	Not Acceptable	Sample gas temperature range is low; Doesn't generate a pct.
5	Not Acceptable	Slow response time (20 s for 63% of step change)
6	Acceptable	N/A
7	Still Awaiting Information	
8	Not Acceptable	Angled probe; Slow response time
9	Not Acceptable	#10 performs the same except broader temp. range for same cost
10	Acceptable	N/A
11	Not Acceptable	Sample gas temperature range too high (600-1100°C); Large min. insertion length (6")
12	Not Acceptable	Sample gas temperature range too high (550-1600°C)
13	Not Acceptable	Slow response time (8 s for 90% of step change); Large min. insertion length (9")
14	Not Acceptable	Slow response time (7 s for 90% of step change); Large min. insertion length (middle 1/3rd of vessel)
15	Not Acceptable	Slow response time (20 s for 63% of step change)
16	Not Acceptable	Slow response time (20 s for 63% of step change)
17	Not Acceptable	Sample gas temperature range is too low (-100 - 400°C)
18	Not Acceptable	Sample gas temperature range is too low (-100 - 250°C); Slow response time (15 s)
19	Not Acceptable	Sample gas temperature range is too low (-100 - 250°C)
20	Not Acceptable	Sample gas temperature range too high (700-1400°C); Slow response time (15 s)
21	Not Acceptable	Sample gas temperature range is too low (<500°C); Large minimum insertion length (10")

As of now, there are three possible candidates for oxygen sensors. There are still some leads that are being pursued, but further analysis will be done to decide which will be used for the facility. Eventually, a Model 9060H Teledyne Heated Zirconium Oxide probe with a 1.25" diameter was chosen.

Non-intrusive methods of measuring oxygen concentration have been investigated. Using the planar laser-induced fluorescence (PLIF) system and acetone, whose evaporation point is 725°C, air concentration can be measured non-intrusively. This, however, would require the acquisition of a camera intensifier. A camera intensifier that would work with the current PLIF system costs $32,015. A purchase order for such a camera intensifier has been placed.

Flow

As mentioned previously, due to the low-flow conditions, there's not enough differential pressure generated for DP flow meters to generate a signal. In addition, thermal anemometers become very difficult, if not impractical, for this application. This is due to the expected high fluid temperatures and the changing temperature and concentration of the fluid with respect to time. The only other available option is using particle image velocimetry. Using a PIV system in conjunction with titanium dioxide seeding particles (whose melting temperature is 1800°C), the flow can be measured non-intrusively via camera ports that are set up in the proposed facility design. Furthermore, the duct will be designed with quartz windows such that counter-current flow could be observed.

Location of Instrumentation

The location of the instrumentation was based largely on the CFD studies of Dr. Chang Oh, et al.[1] and our own work by Taekyu Ham. Thermocouples and oxygen sensors were placed in locations to track the progression of recirculation currents through the test section. Pressure sensors were placed in various locations within the vessel to monitor the static pressure and detect pressure variations within the vessel. Camera and laser ports were positioned in a couple different locations on the vessel as well as the duct to measure flow velocity. Please see the design drawings for exact location of instrumentation.

Vessel Enclosure and Scheduling

Currently, an enclosure (not pressure sealed) is being designed for the vessel that will have an appropriately scaled volume to mimic the prototypic system. The design will also incorporate holdings to place the camera and laser so that PIV and PLIF can be effectively utilized. Table 23 gives a listing of the major components, their lead times and costs.

Table 23. Scheduling and Budgeting

Major Components	Lead Time	Costs
Vessel	12-14 weeks	$72,000.00
Graphite Rods	4-5 weeks	$1,332.00
Pressure Transmitters	2 weeks	$1,519.00/each
Thermocouples	2 weeks	$34.00/each

Geometry and Instrumentation Placement

Figure 68, Figure 69, and Figure 70 below outline the geometry of the proposed facility. Figure 71 outlines the most current idea of where instrumentation will be placed on the top and bottom of the vessel.
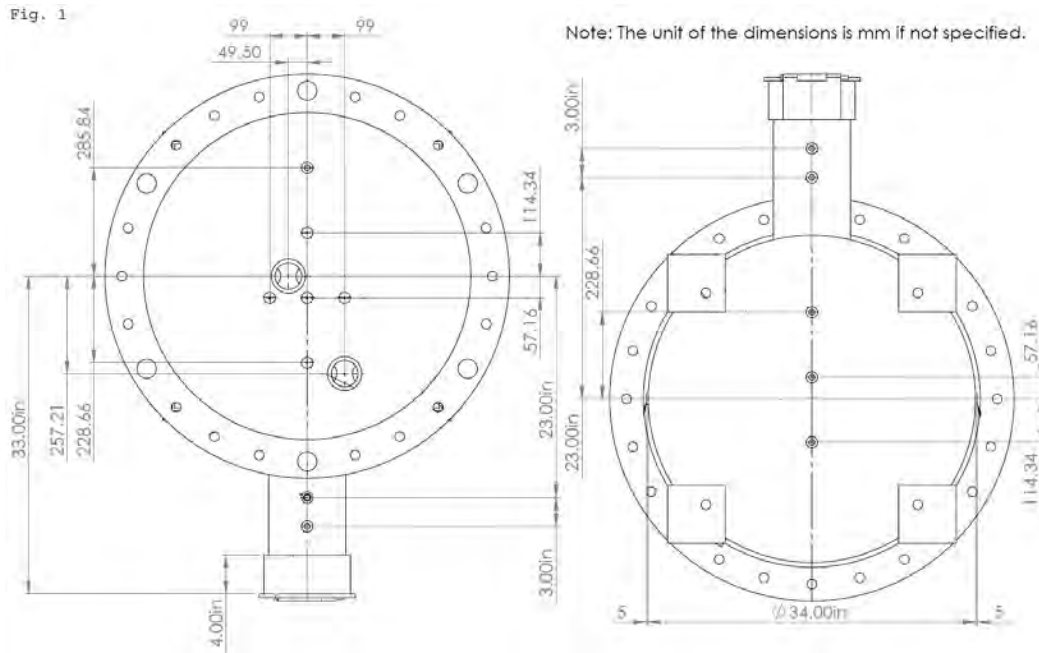
Figure 68. Top view (left) & bottom view (right)
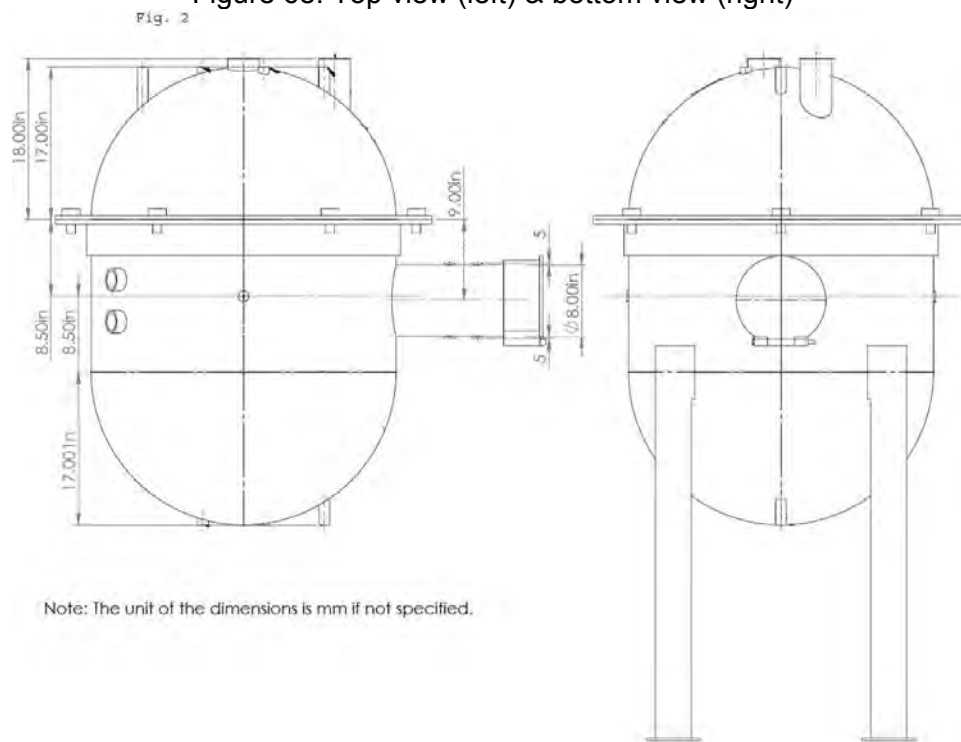
Figure 69. Side view (left) & front view (right)

80

Note: The unit of the dimensions is mm if not specified.

Fig. 3

2 X ⌀ 2.50in

2 X ⌀ 2.00in

42.90

4.67in

5.67in

VIEW H
SCALE 1 : 20

H

42.90

42.84

18.00in

SECTION G-G
SCALE 1 : 20

G   G
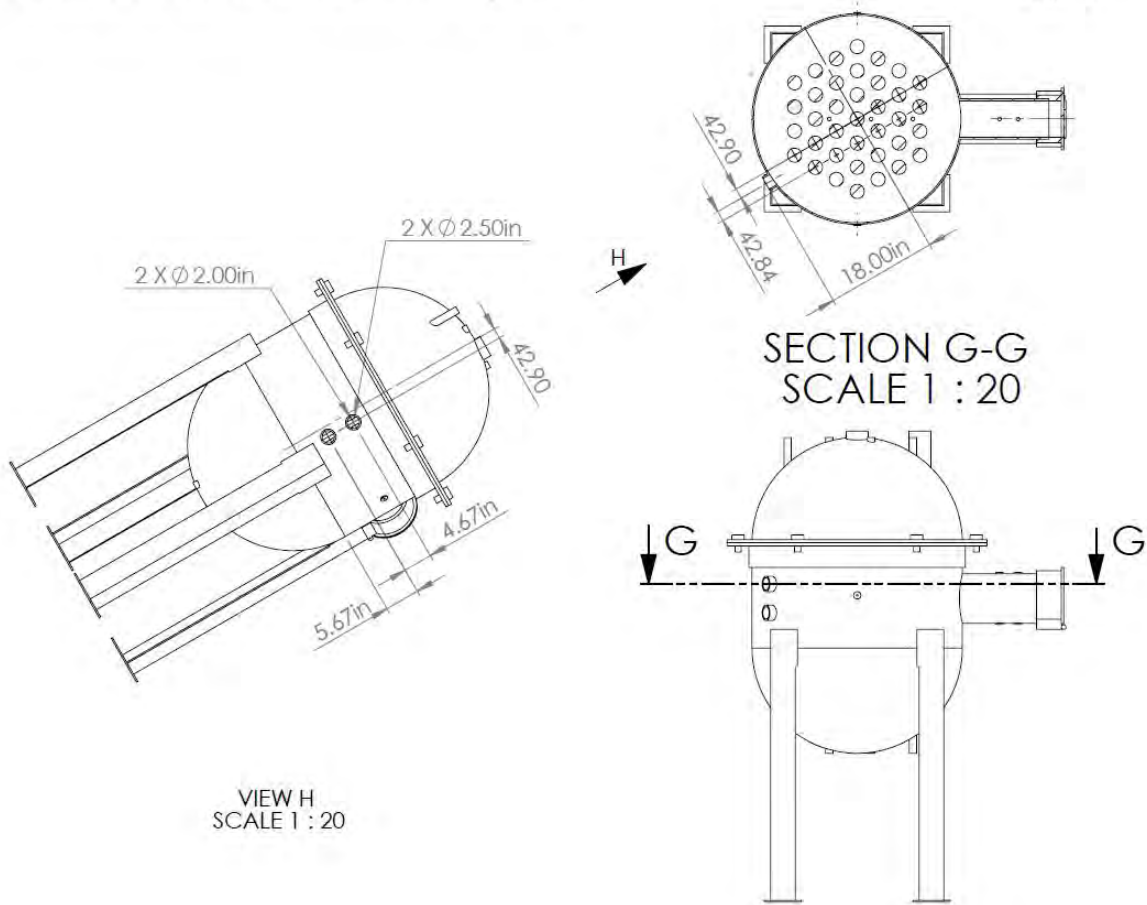
Figure 70. Cut view of the midplane (top right) & back angle view (left) &
side view (bottom right)

Fig. 4
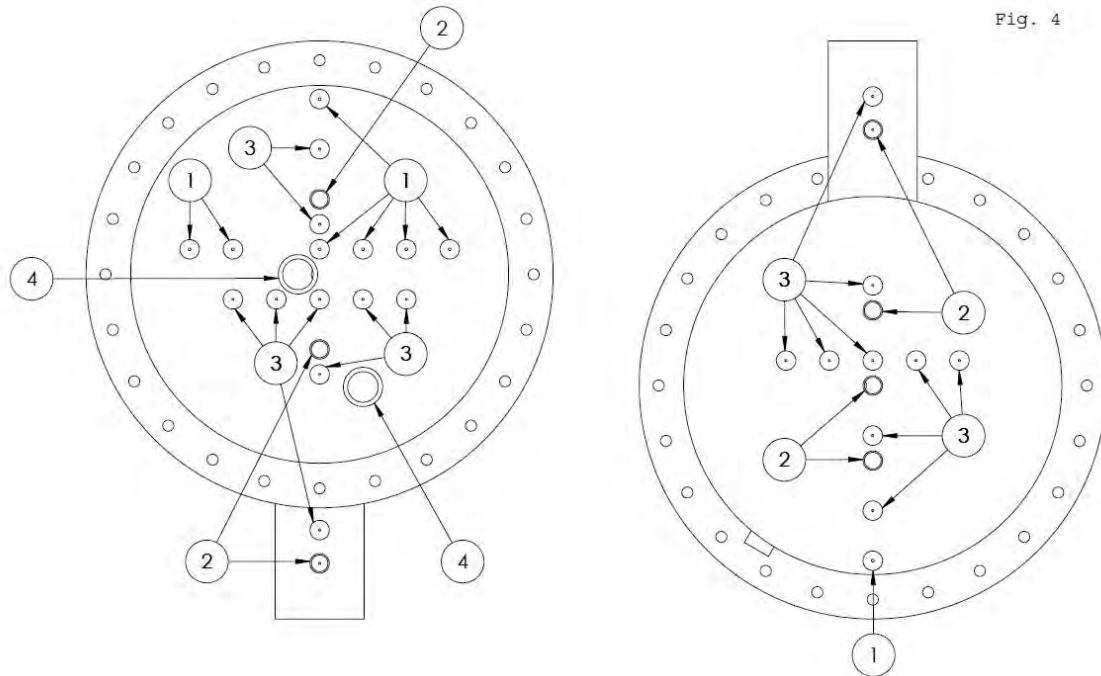
Baloon No.	For Instrumentation	Inner Diameter	Outer Diameter
1	Pressure Transmitter	1/4in	7/4in
2	Oxygen Sensor	3/2in	7/4in
3	Temp. Sensor	3/16in	7/4in
4	Camera ports (above)	70mm	90mm

Figure 71. Sensor location at top of the vessel (left) & bottom of the vessel (right)

Figure 72 is a side view of the bottom semi-hemispherical (2:1 elliptical head) shell of the air-ingress experimental facility. The shell has an outside diameter of 34" and a height of 8.5". It is constructed of Alloy 800H. The shell thickness is ¼". Sixteen - ¾", schedule 40 pipes are welded to the bottom of the shell. These pipes are fabricated from Alloy 800H and vary in length – the shortest being 8.5" long. All pipes, however, extend to the same vertical level which is 17" below the top of the bottom semi-hemispherical shell. This allows clearance for insulation to be placed along the bottom of the vessel without interfering with the entrance of the instrumentation ports. Also, the additional distance away from the vessel reduces the temperature requirements for the Conax® glands which will attach the thermocouples, pressure transducer tubing, and oxygen sensors to the vessel while maintaining the pressure boundary of the entire system. The relaxed temperature requirement is also beneficial for the instrumentation by reducing the possibility of an electrical failure.

A preliminary 1-D fin calculation shows that with a base temperature of 750°C and a heat transfer coefficient of 2 W/(m^{2}K), the temperature at the end of the pipe is about 650°C. Similarly, with a heat transfer coefficient of 5 W/(m^{2}K), the pipe-end temperature drops to 535°C. A Fluent calculation shows that the pipe-end temperature is 280°C. This takes into consideration radiation and convection heat transfer. These calculations suppose that one-half of the pipe length is wrapped in adiabatic insulation. It was decided not to make the pipes longer which would be a possible solution in lowering the pipe-end temperatures. Instead, in the current design, the pipes will extend to only 17 inches so as to not increase the overall

height of the facility. It is preferred to keep it as short as possible for convenience in performing experiments and working around the facility.   This part of the vessel will be welded to the middle shell or test section shown in Figure 77 and Figure 78.

Figure 73 is a bottom view of the bottom semi-hemispherical shell of the air-ingress experimental facility. In this figure, the type, position and spacing of the instrumentation ports are shown. Also, the position of the instrumentation ports with respect to the support columns can be seen. The perforated lines represent the support column position.

Baloon No.	Holes For Instrumentation	Inner Diameter (in)	Outer Diameter (in)
1	Pressure Transmitter	0.824	1.050
2	Oxygen Sensor	0.824	1.050
3	Temp. Sensor	0.824	1.050
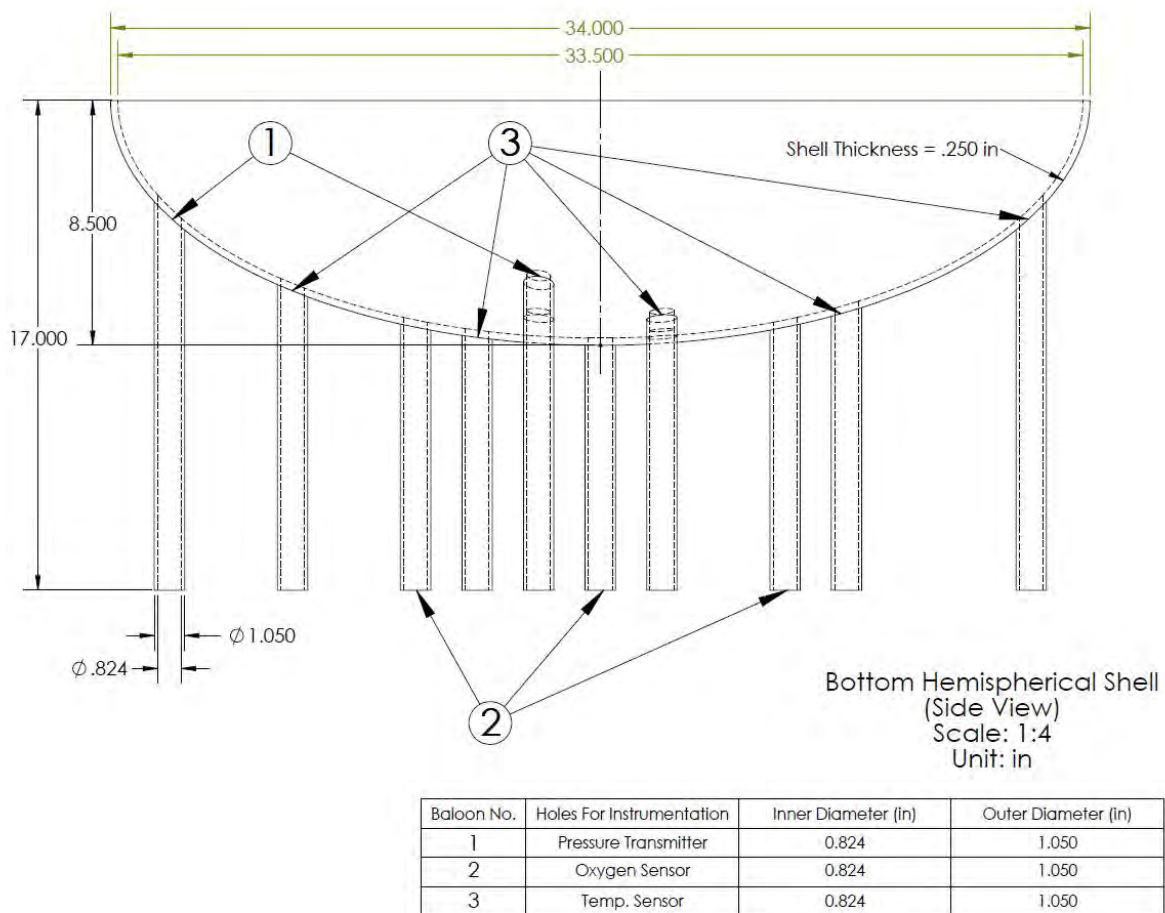
Figure 72. Side view of the bottom hemispherical shell

Balloon No.	Holes For Instrumentation	Inner Diameter (in)	Outer Diameter (in)
1	Pressure Transmitter	0.824	1.050
2	Oxygen Sensor	0.824	1.050
3	Temp. Sensor	0.824	1.050
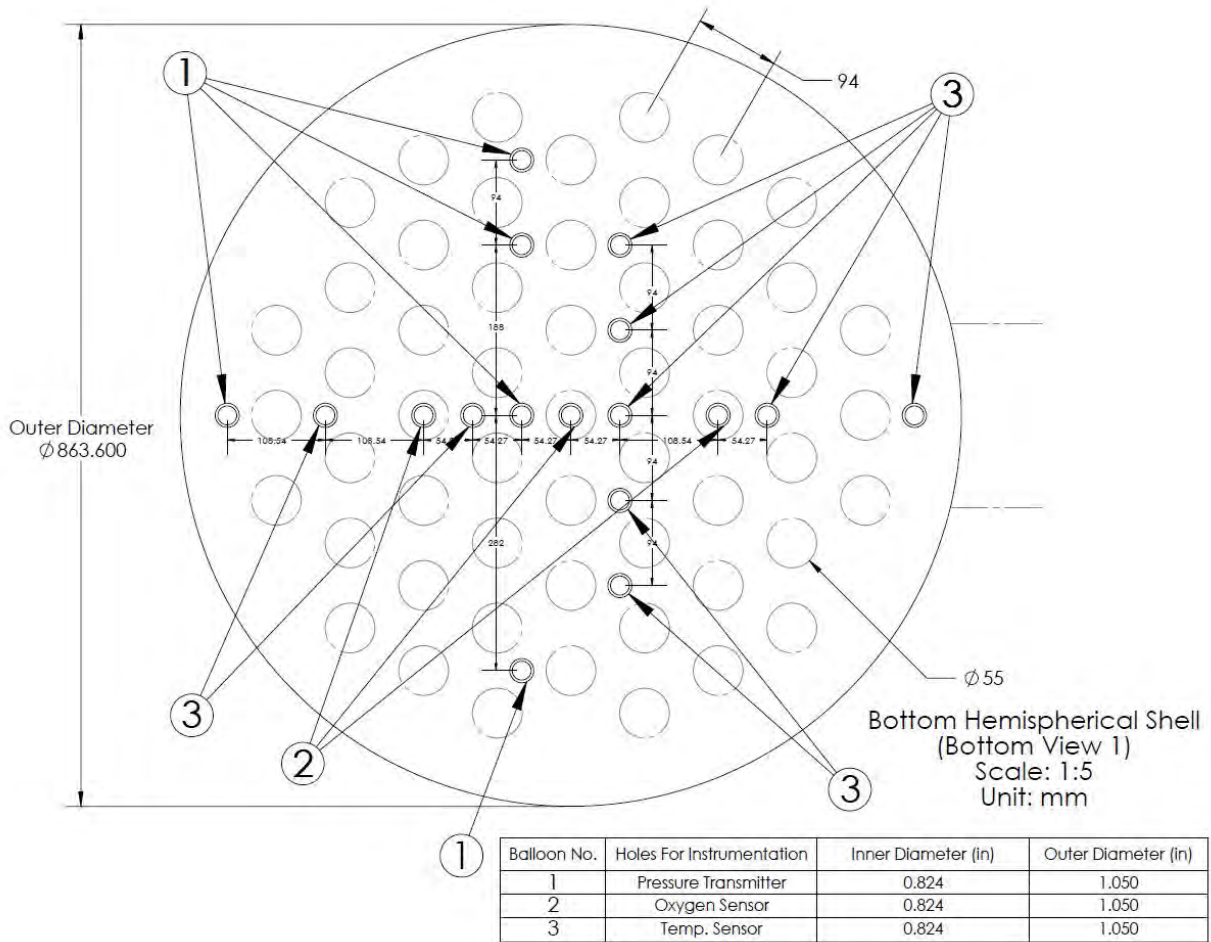
Figure 73. Bottom view of the bottom hemispherical shell

Figure 74 is another bottom view of the bottom semi-hemispherical shell. The type and position of each instrumentation port can be seen relative to the support column position. In Figure 73 and Figure 74, the orientation is such that the outlet is pointing to the right.
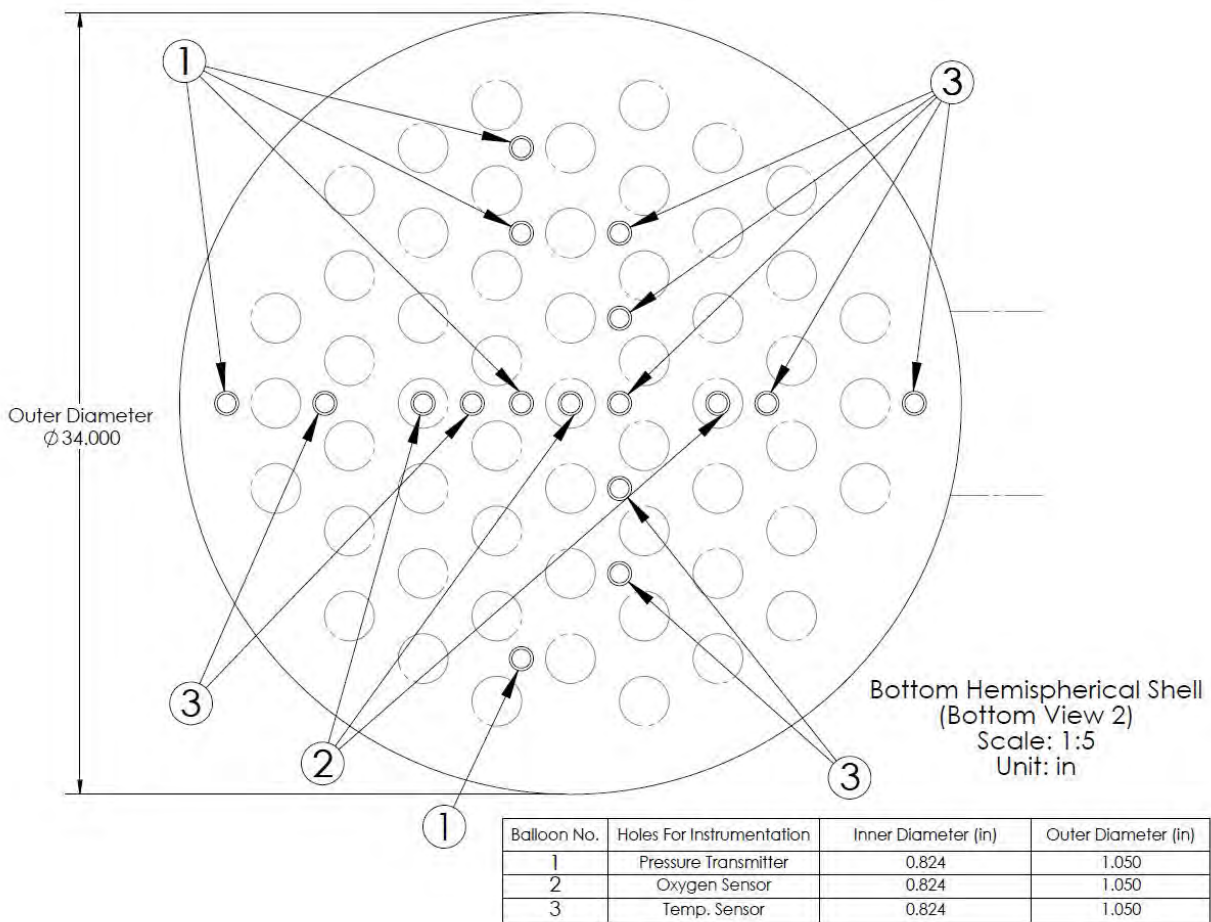
Figure 74. Bottom view of bottom hemispherical shell

Balloon No.	Holes For Instrumentation	Inner Diameter (in)	Outer Diameter (in)
1	Pressure Transmitter	0.824	1.050
2	Oxygen Sensor	0.824	1.050
3	Temp. Sensor	0.824	1.050

Figure 75 is a top and side view of the bottom plate which separates the bottom semi-hemispherical shell from the middle shell. It's constructed of Alloy 800H. It rests on a lip on the bottom of the middle shell. The support columns located in the middle shell will be positioned in the quasi-hexagonal array of 55 circles which mimics the prototypic support column arrangement. Each circle has a diameter of 55 mm and is 0.5 in. deep. The center-to-center pitch is 94 mm. This drawing is oriented in such a way that the outlet duct points to the right as indicated by the dotted lines. The holes with the "4" designation are for the cold toes of the insertion heaters to pass through and to fill the bottom semi-hemispherical shell with ¼" ceramic balls. Filling the bottom shell with ceramic balls reduces its free volume and helps preserve the phenomenology of the prototypic system.

Figure 76 is the bottom view of the bottom plate with and without the support column positions projected onto the plate. The holes for the various types of instrumentation are shown. A chamfer is used for each hole and its dimensions are outlined accordingly. The reason for the chamfer is to facilitate the successful installation of the instrumentation into the test section.

Figure 77 and Figure 78 show the middle shell or test section of the air-ingress experimental facility. On the bottom of the shell, the lip is located that will support the bottom plate. On the top of the shell, a flange is welded. The top semi-hemispherical shell will be bolted to this top flange. The duct is located at the front. Extensions can be connected to the duct to simulate different break scenarios. An air piston will be used to secure the duct cover and initiate the accident sequence. Toward the back of the middle shell, there are two 2-inch windows constructed of quartz which allow the laser of the PIV/PLIF system to pass through.
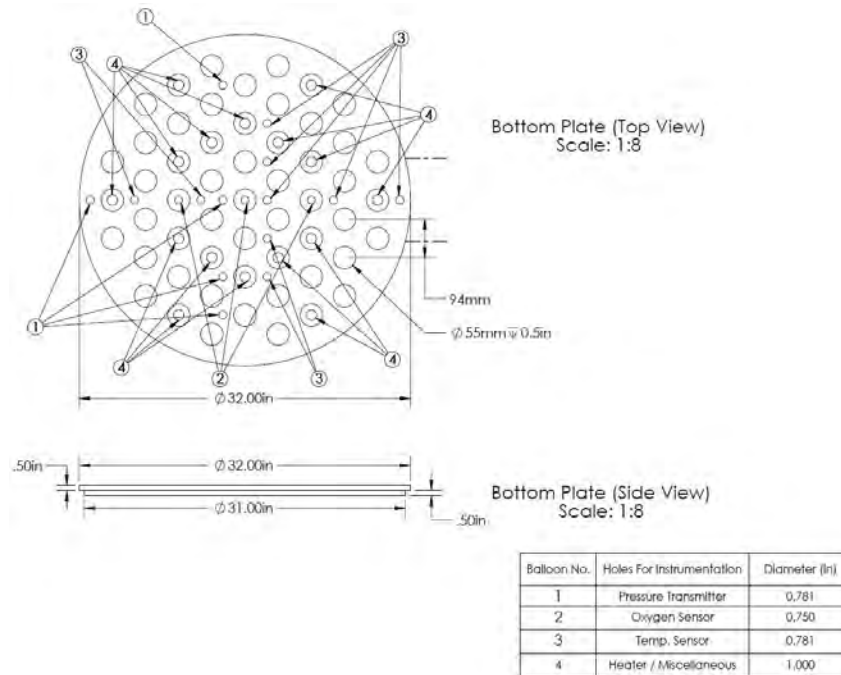
Figure 75. Top view of bottom plate (top) and side view of bottom plate (bottom)

Balloon No.	Holes For Instrumentation	Inner Diameter (in)	Outer Diameter (in)
1	Pressure Transmitter	0.781	1.031
2	Oxygen Sensor	0.750	1.000
3	Temp. Sensor	0.781	1.031
4	Heater / Miscellaneous	1.000	N/A
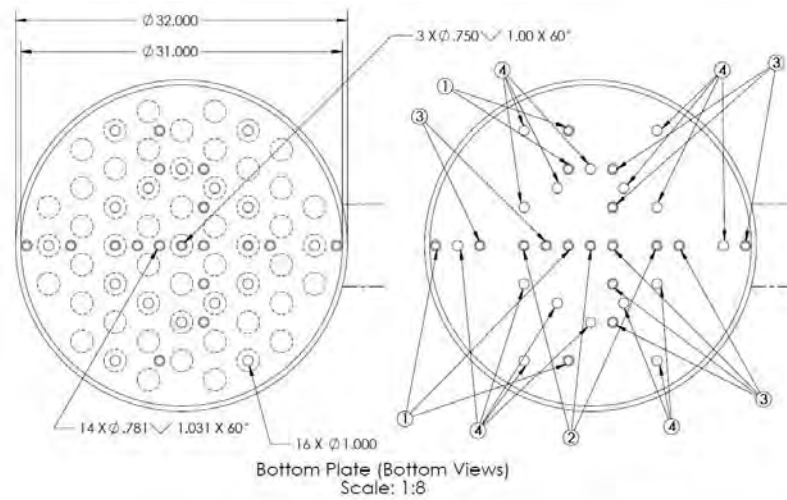
Figure 76. Bottom view of bottom plate
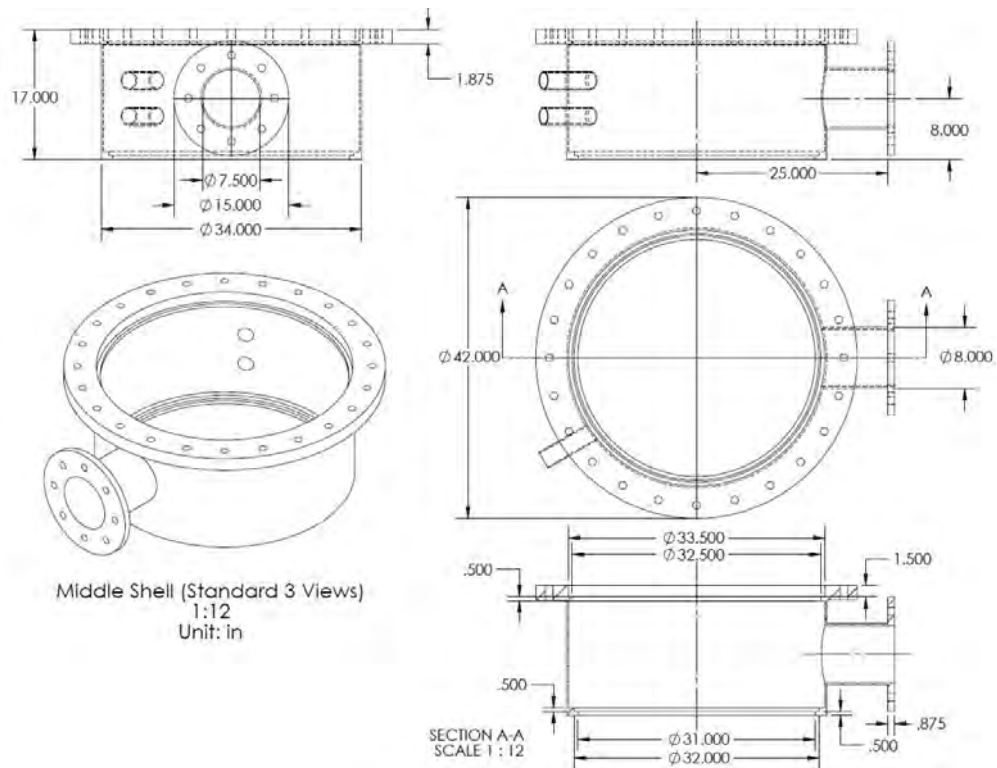
Figure 77. Middle shell or test section

87
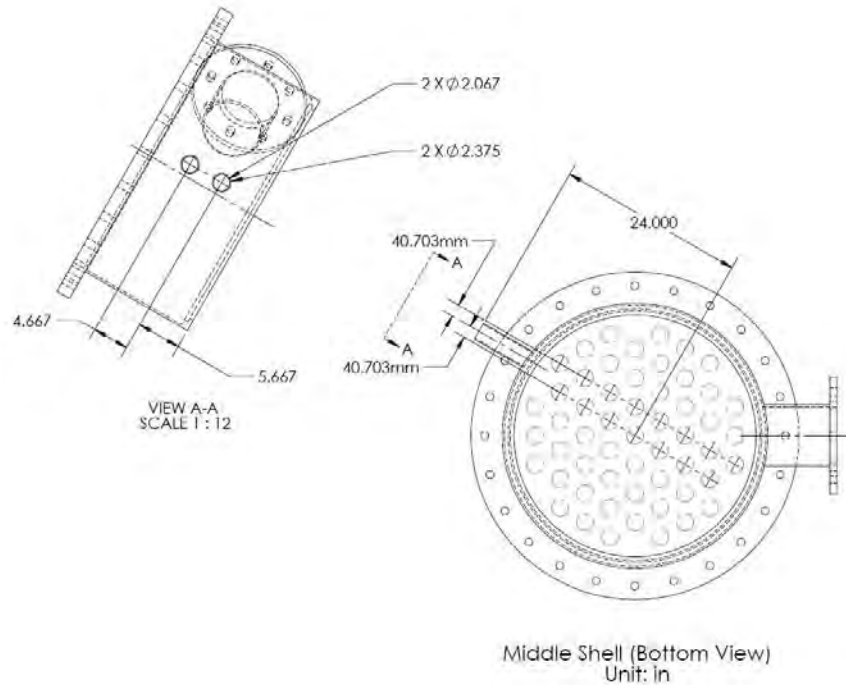
Figure 78. Bottom view of middle shell or test section (top left)

Figure 79 is the top view of the top plate. Figure 80 is the bottom and side view of the top plate. The top plate separates the middle shell from the top semi-hemispherical shell which is shown in Figure 81 through Figure 83.

Figure 79 shows a top view of the top plate with and without the support column location projections. The top side of the plate has chamfers on the holes that are designed to allow the oxygen sensors and heaters to pass through. As stated previously for the bottom plate, this is to facilitate the successful installation of the instrumentation into the test section. The two larger holes are for the camera to take images for the PIV/PLIF system.   Here, velocity and concentration measurements are taken. The 1" holes, in each support column anchor, are to ensure that the support columns are correctly inserted to their proper position. The orientation of this drawing is such that the outlet duct is pointed to the right.

2 X Ø .750
⌵ 1.000 X 60°

6 X Ø 1.000
⌵ 1.250 X 60°

Ø 33.500

Top Plate (Top View)
Scale: 1:8
Unit: in

Balloon No.	Holes For Instrumentation	Inner Diameter	Outer Diameter
1	Oxygen Sensor	0.750in	1.000 in
2	Camera Ports (Top)	2.067in	N/A
3	Heater	1.000 in	1.250 in
4	Screw	0.250in	N/A
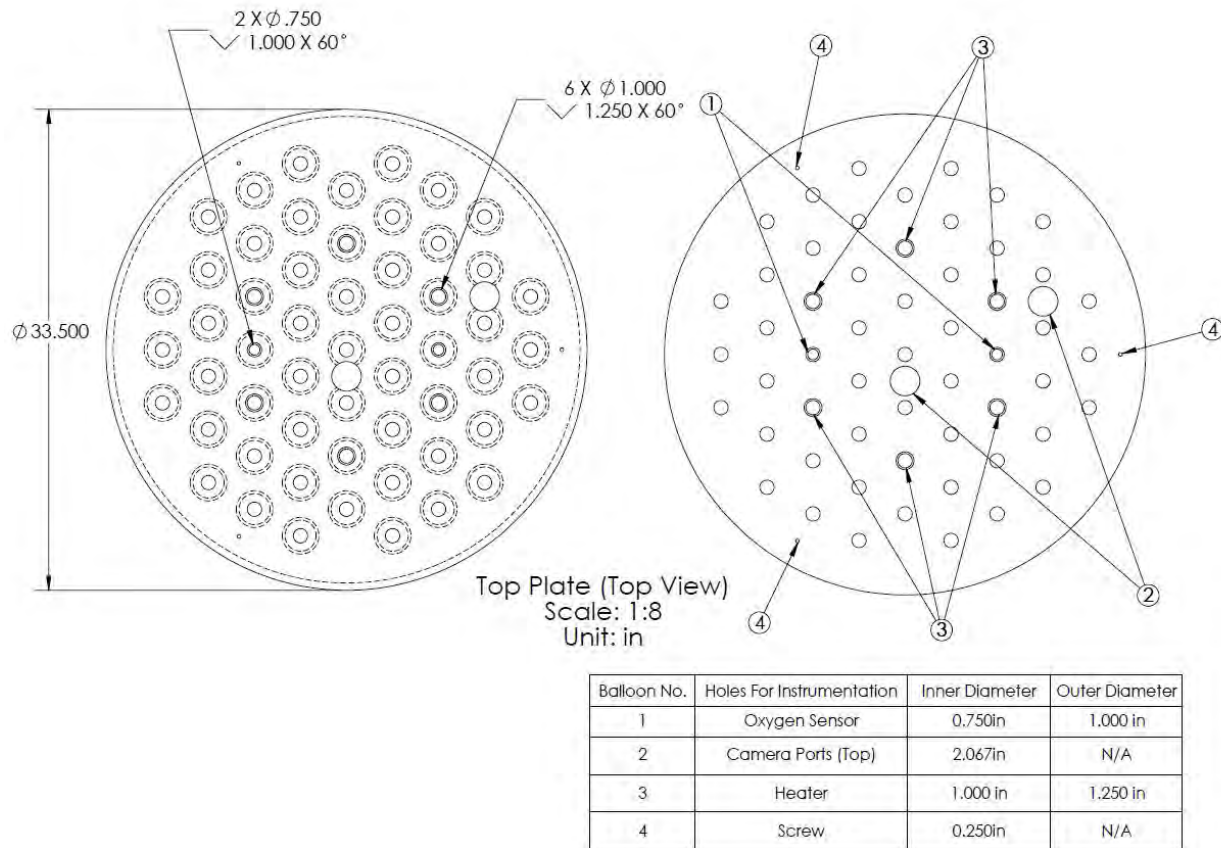
Figure 79. Top view of top plate

Figure 80 shows a bottom view and side view of the top plate. The hexagonal array of holes is designed for the support columns to occupy. Each hole has a chamfer to make it easier to align the support column within the hole. This alignment is critical to preserve the flow phenomenology. It is also seen that the plate thickness is one inch thick and is constructed of Alloy 800H.

Ø 55 mm ⏦ 0.5 in
⋁ Ø 65 mm X 60°

94mm

Top Plate (Bottom View)
Scale: 1:8

Balloon No.	Holes For Instrumentation	Inner Diameter
1	Oxygen Sensor	0.750 in
2	Camera Ports (Top)	2.067in
3	Heater	1.000 in
4	Screw	0.250in

Ø 1.000

Ø 32.500in

Top Plate (Side View)
Scale: 1:8

.500in

.500in

Ø 33.500in
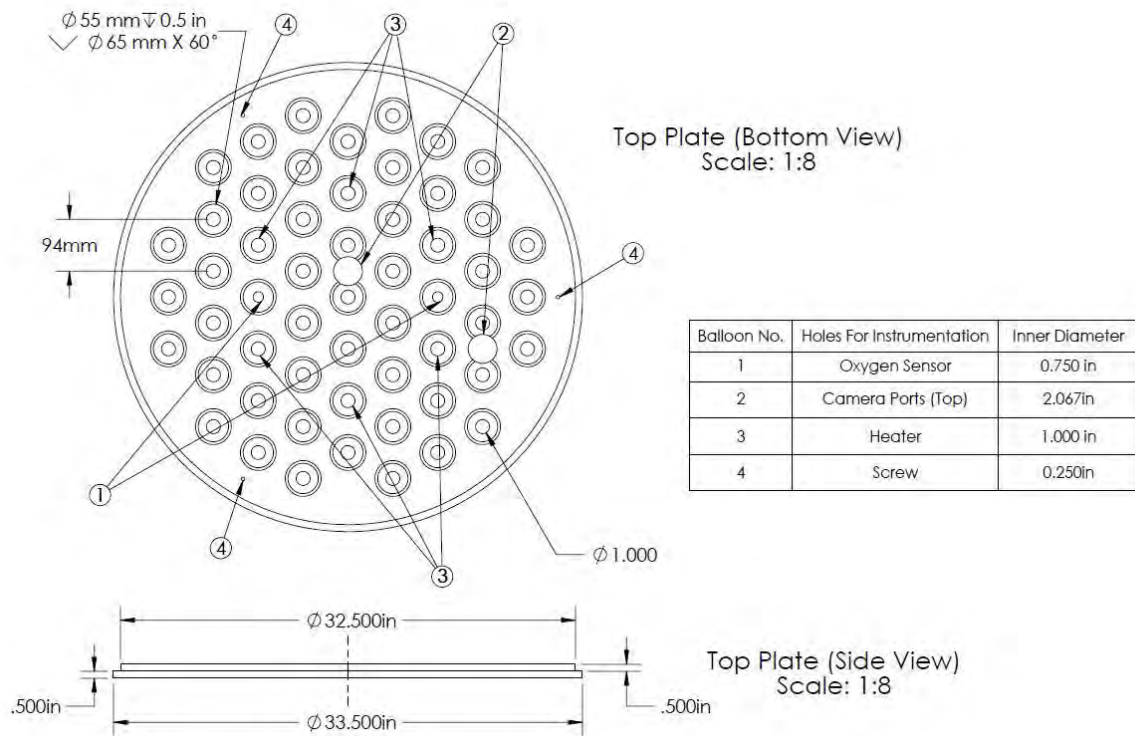
Figure 80. Bottom view of top plate (top) and side view of top plate (bottom)

Ø 1.049

Ø 2.067

Shell Thickness = .250 in

18.375

8.500
8.250

.500

1.375

Ø 33.500
Ø 42.000

Top Hemispherical Shell
(Side View)
Scale: 1:5
Unit: in

Balloon No.	Holes For Instrumentation	Inner Diameter (in)	Outer Diameter (in)
1	Oxygen Sensor	0.824	1.050
2	Camera ports (above)	2.067	2.375
3	Heater	1.049	1.315
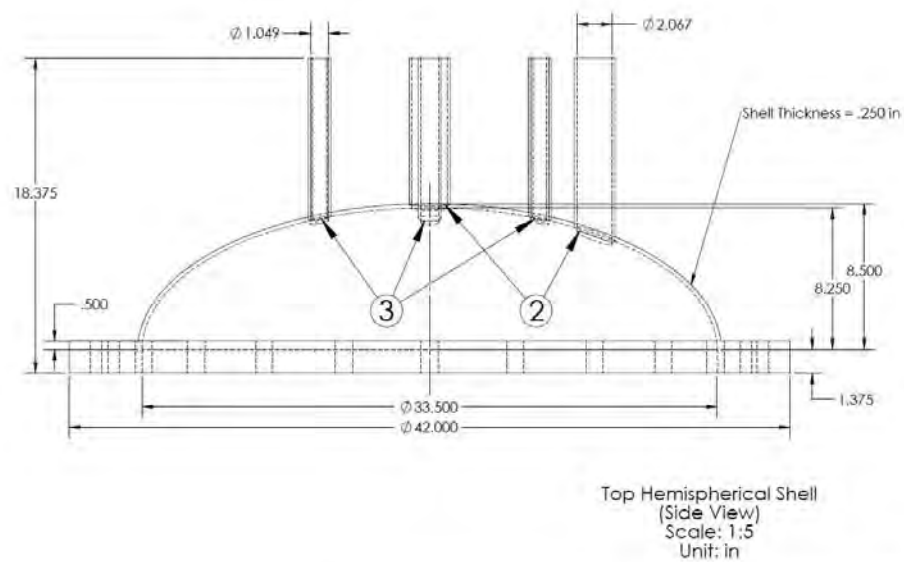
Figure 81. Side view of top hemispherical shell

90
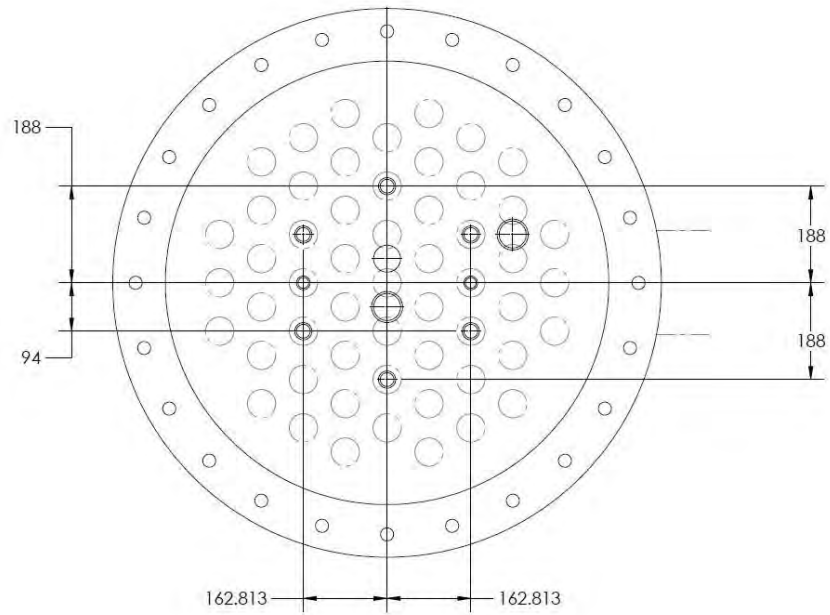
Top Hemispherical Shell
(Top View 1)
Scale: 1:8
Unit: mm

Figure 82. Top view of the top hemipsherical shell
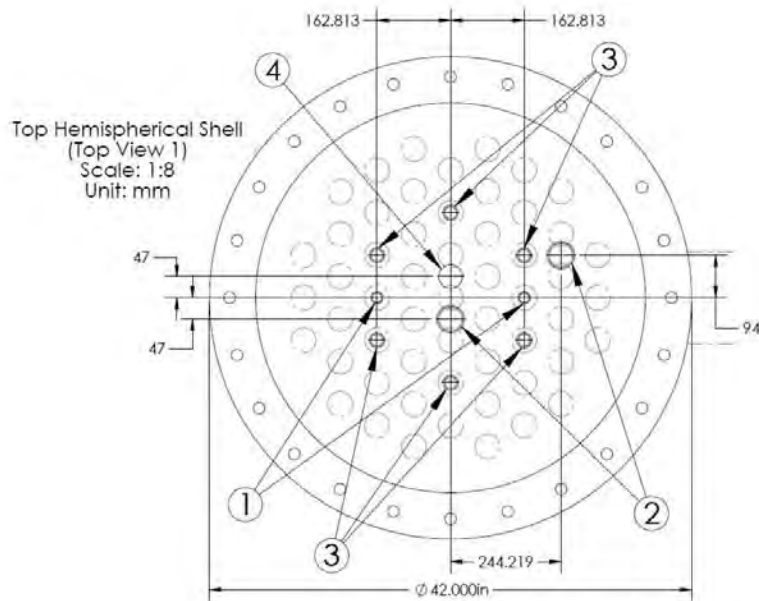
Top Hemispherical Shell
(Top View 1)
Scale: 1:8
Unit: mm

Balloon No.	Holes For Instrumentation	Inner Diameter (in)	Outer Diameter (in)
1	Oxygen Sensor	0.824	1.050
2	Camera ports (above)	2.067	2.375
3	Heater	1.049	1.315
4	Miscellaneous	2.067	N/A

Figure 83. Top view of top hemispherical shell

Figure 81 is a side view of the top semi-hemispherical shell. It is constructed of Alloy 800H. This piece is bolted down to the middle shell as seen in Figure 77 and Figure 78. There are 11 openings on the top of the head – 1 for insertion of ceramic balls, 2 for camera ports, 2 for oxygen sensors, and 6 for heaters. All pipes extending from the shell end at the same vertical level (17 inches above the shell bottom). This allows clearance for insulation to be installed and relaxes the temperature requirement for the Conax® glands. The ceramic balls (which are primarily aluminum oxide and silicon dioxide) add approximately 270 kg to the top plate. Even at the high operational temperatures of 750°C, the added weight on the top plate produces a minimal deflection of 0.0025".

Figure 82 and Figure 83 are a top view of the top semi-hemispherical shell. These figures show the type, position and relative spacing of the ports with respect to each other as well as the support columns. For both figures, they are oriented such that the outlet duct is pointing to the right.

Costs for Significant Items In Vessel Construction and Operation

Table 24. Lists of costs for construction of vessel

Item	Manufacturer	Model No.	Cost	Quantity	Total Cost	Lead Time
Pressure Glands	Conax	MHM5-250-A2-G	$287/ea	5	$1,435.00	1-2 weeks
Temperature Glands	Conax	MHM5-125-A4-G, P/N 314414-050	$227/ea	8	$1,816.00	1-2 weeks
O_2 Sensor Glands	Conax	PG5-750-A-G	$141/ea	5	$705.00	1-2 weeks
Heater Glands	Swagelok	SS-1610-1-16BT	$50.40/ea	6	$302.40	1-2 weeks
Pressure Tubing	PA, Inc.	0.25 in. tubing/0.049 in. wall thickness	60 ft @ $12.00/ft	60 ft	$720.00	In Stock
Alloy 800H Pipe	JJ Mfg.	¾", Sch. 40	$26.00/ft	14.7 ft (required length)	$382.20	In Stock
Alloy 800H Pipe	JJ Mfg.	1", Sch. 40	$35.00/ft	4.8 ft. (required length)	$168.00	In Stock
Alloy 800H Pipe	JJ Mfg.	2", Sch. 40	$60.00/ft	2.9 ft. (required length)	$174.00	In Stock

Thermcouple	OMEGA	NQXL-18G-31	$33.65/ea	8 (min. number)	$269.20	1 week
Pressure Transmitter	Honeywell	STD930-E1A-00000-1C	$1,519.00/ea	5 (min. number)	$7,595.00	2 weeks
Oxygen Sensor	Teledyne	9060H (20" length)	$2,920.00/ea $4,970.00/ea	4 probes and 2 control units	$21,620.00	6-8 weeks
Insertion Heater	Watlow	MultiCell Heater	$1,013.09	6	$6,078.54	10 working days
Band Heaters	Chromalox	34" ID X 4" W 5kW 220V	$906.00	1	$906.00	20 days
Band Heaters	Chromalox	42" ID X 4" W 5kW 220 V	$1,130.00	1	$1,130.00	20 days
Support Columns	Toyo Tanso	55 mm O.D. 15 in. length Hollow Rod: 25 mm I.D.	$165.00/solid rod; $210.00/hollow rod	49 solid rods/6 hollow rods	$9,345.00	4-5 weeks
Ceramic Balls	Tipton Ceramic Corp.	Ceramic Ball; 13% Al_2O_3, 80% SiO_2	$120/bag	18 bags	$2,160.00	1-2 weeks
Low Pressure Sight Class	Rayotek Scientific, Inc.	Window Material: Fused silica	$1,625/ea	4 lenses	$6,500.00	10 weeks
Pneumatic Air Cylinder	Grainger	6 in. Bore, 12 in. Stroke	$699.00	1	$699.00	1-2 weeks
Insulation	?	?		?	?	?
Intensifier	LaVision, Inc.	IRO 25 Intensified Relay Optics	$37,500	1	$37,500	8-10 weeks
Solid Particle Seeder	LaVision, Inc.	Particle Blaster 100	$9,500	1	$9,500	8-10 weeks
Titanium Dioxide Seed Particles	LaVision, Inc.		$170	1	$170	8-10 weeks
Total					$109,175.00	

Design of Confinement

Utilizing the prototypic geometry and normal operating conditions of the GT-MHR, it was found that the mole ratio of air in the confinement to helium in the vessel is 5.15. In order to maintain this mole ratio, the confinement volume of the scaled-down geometry was calculated for different initial vessel pressures. In these calculations, the volume of the confinement is taken to be 25,000 m^3 and the free volume of the pressure vessel 265 m^3. The initial pressure and temperature of the vessel is 7 MPa and 850°C, respectively. The initial pressure and temperature of the confinement is 0.10 MPa and 25°C, respectively. The ideal gas law was used to calculate the number of moles and free volume of the scaled-down confinement.

Table 25. Scaled-down confinement volume for different initial vessel pressures

Initial Scaled-down Vessel Pressure (psig)	Initial Vessel Temperature (°C)	Scaled-down Confinement Volume (m^3)
0	750	0.315
30	750	0.963
60	750	1.605

In addition to this simple analysis, using the first law of thermodynamics, the mixed mean temperature of the pressure vessel-confinement system is calculated. This analysis was performed to give the final temperature of the air-helium mixture after the helium is emptied into the confinement. This temperature occurs after the contents are well mixed. It is also assumed that that no heat is lost or gained from the confinement and that no work is done by the control volume, which makes sense since it is a rigid volume.

Table 26. Initial conditions for final temperature analysis

	Confinement	Pressure Vessel
Pressure (MPa)	0.101325	7
Volume (m^3)	25,000	265
Temperature (K)	300	1123
Species	100% Air	100% Helium

The governing equation is given by

$$U_f - U_i = 0 \qquad\qquad [56]$$

where U_f and U_i are the internal energy of the system at the final and initial stages, respectively. By making some proper substitutions and reworking this equation, the final temperature can be solved.

$$T_f = \frac{(m_{he} C_{v_i,he} T_{i,he} + m_a c_{v_i,a} T_{i,a})}{(m_{he} c_{v_f,he} + m_a c_{v_f,a})} \qquad\qquad [57]$$

By iterating this equation, T_f can be solved. Using the initial conditions listed in Table 26, the final temperature is 382.6 K. Using the ideal gas law, the final pressure is 0.1538 MPa. In the GT-MHR containment, there are vents located on the wall. Therefore, the global pressure within the confinement is maintained at or very near atmospheric pressure. Since the final pressure in the first law analysis is above atmospheric pressure, a transient control volume analysis is performed. The governing equation is given in equation [35]. It is assumed that only air escapes out of the confinement and it does so at its initial temperature.

$$U_f - U_i = -m_e h_e \qquad [58]$$

Rearranging Eq. 58, the final temperature can be solved.

$$T_f = \frac{\left(m_e C_{p,a} T_{i,a} + m_{he} C_{v_i,he} T_{i,he} + m_{a,i} c_{v_i,a} T_{i,a}\right)}{\left(m_{he} c_{v_f,he} + m_{a,f} c_{v_f,a}\right)} \qquad [59]$$

where $m_e = m_{a,i} - m_{a,f}$. Iterating over Equations 58 and 59 the with ideal gas law, a final temperature can be found. All final pressures are atmospheric pressure. A summary of the results can be found in Table 27. Different cases are based initial vessel pressure in the scaled-down facility.

Table 27. Results of transient control volume analysis following depressurization

	Final Temperature (K)	Percent of Initial Air Mass Lost
Prototype	366	37.2%
Scaled-down (60 psig)	406	42.5%
Scaled-down (53.4 psig)	394	37.1%
Scaled-down (30 psig)	360	18.7%
Scaled-down (0 psig)	327	-4.0%

From Table 27, it can be seen that the closest final temperature can be attained when the initial vessel pressure of the scaled-down system is about 30 psig. The closest species concentration can be attained when the initial vessel pressure of the scaled-down system is 53.37 psig.

Feasibility of Reduction of the Vessel Temperature Rating from 750°C to 650°C

The feasibility of a reduction in the vessel temperature rating is investigated in this section. This is to make the cost of the facility construction affordable. Although a thorough cost analysis has not yet been performed, it appears to be advantageous to reduce the vessel temperature rating from 750 to 650°C. There are two sources of cost reduction in making the proposed temperature reduction. First, the initial construction costs will be less since less material will be required to make the vessel structurally sound at the design pressure conditions. This is due to an increase in the allowable stress of the Alloy 800H. Second, the maintenance costs of the vessel will be lower at 650°C. A 750°C rated vessel requires the use of a flange gasket to seal the non-welded seams. This means that each time the seal is broken on one of the three gaskets on the vessel (one on the body and two on the duct), a new gasket will have to be

inserted. The costs of the body flange and duct flange are $480 and $425, respectively. On a vessel rated to 650°C, a metal O-ring can be used instead of a flange gasket. The advantage to using a metal O-ring as compared to a flange gasket is that it does not need to be replaced when the seal is broken. A quote for a 650°C, 35 psig rated vessel is underway. Then, a thorough and complete cost analysis will be performed.

The following figures are a series of graphs that show the relative difference in the thermo-physical properties and some key non-dimensional numbers between an air-helium mixture in the enclosure at different initial temperatures (20 - 200°C) and different initial air mole ratios (0 – 1 in increments of 0.1) and pure helium in the vessel at initial temperatures of 200, 400, 648, 676, 750, and 850°C. 648 and 676°C are the two temperature limits for the metal O-rings given by the manufacturer. The figures will closely show the similarity of the relative difference between these important properties as the initial helium temperature is varied.
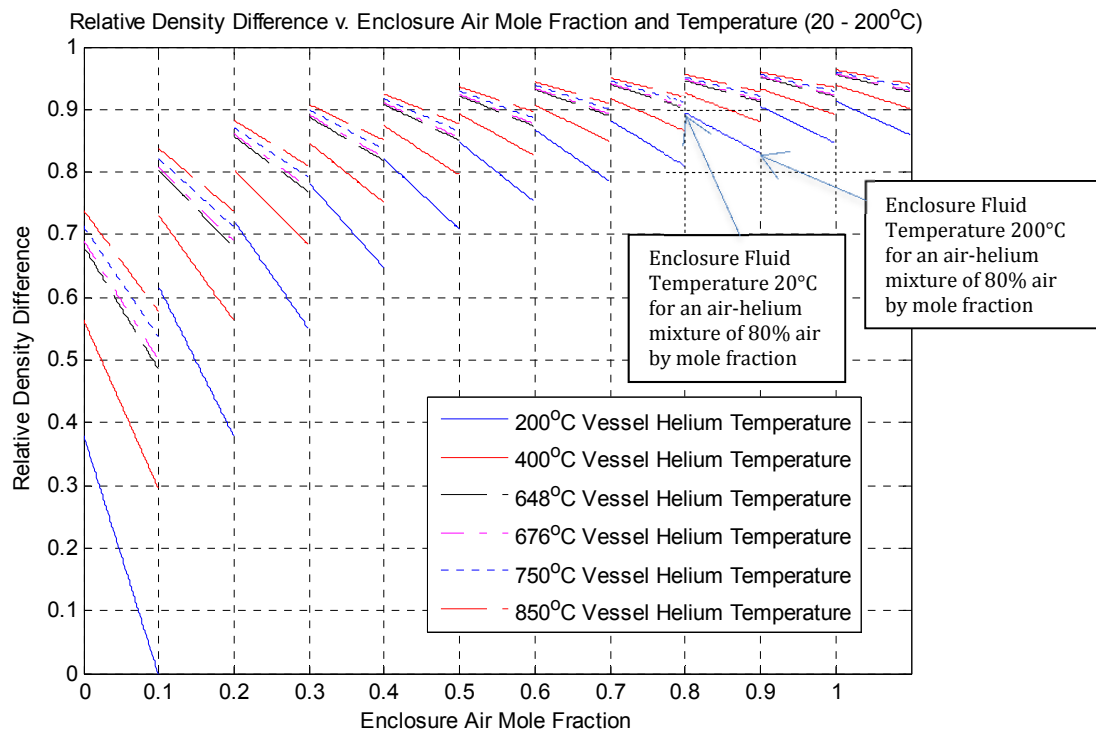
Figure 84. Relativity density difference with respect to enclosure mixture density

Relative Dynamic Viscosity Difference v. Enclosure Air Mole Fraction and Temperature (20 - 200°C)
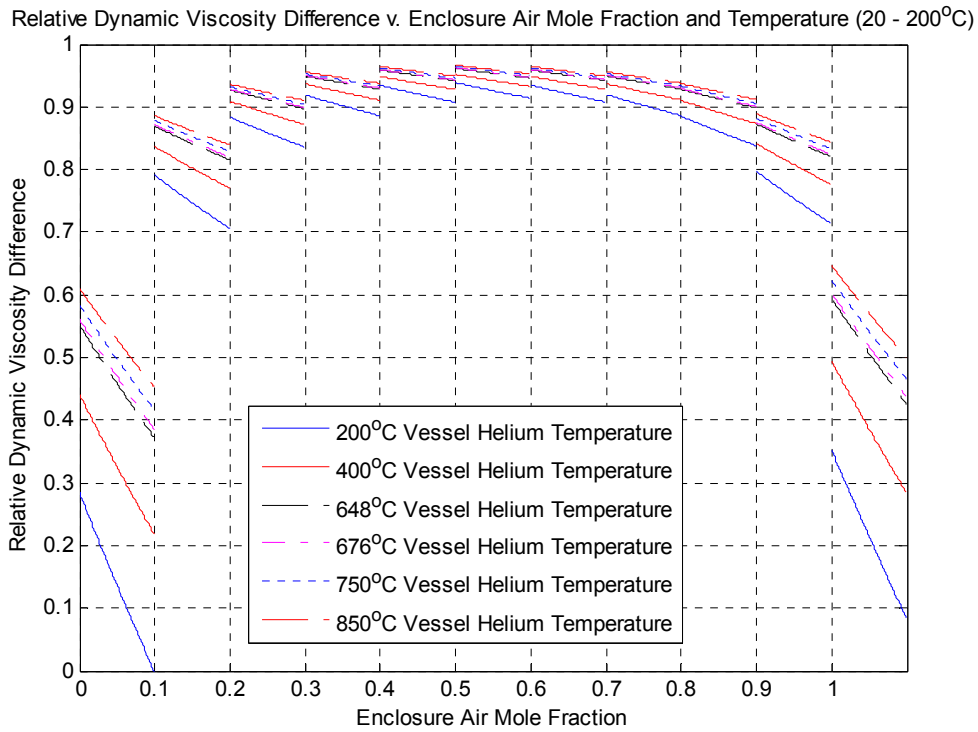
Figure 85. Relative dynamic viscosity difference with respect to vessel helium viscosity

Relative Kinematic Viscosity Difference v. Enclosure Air Mole Fraction and Temperature (20 - 200°C)
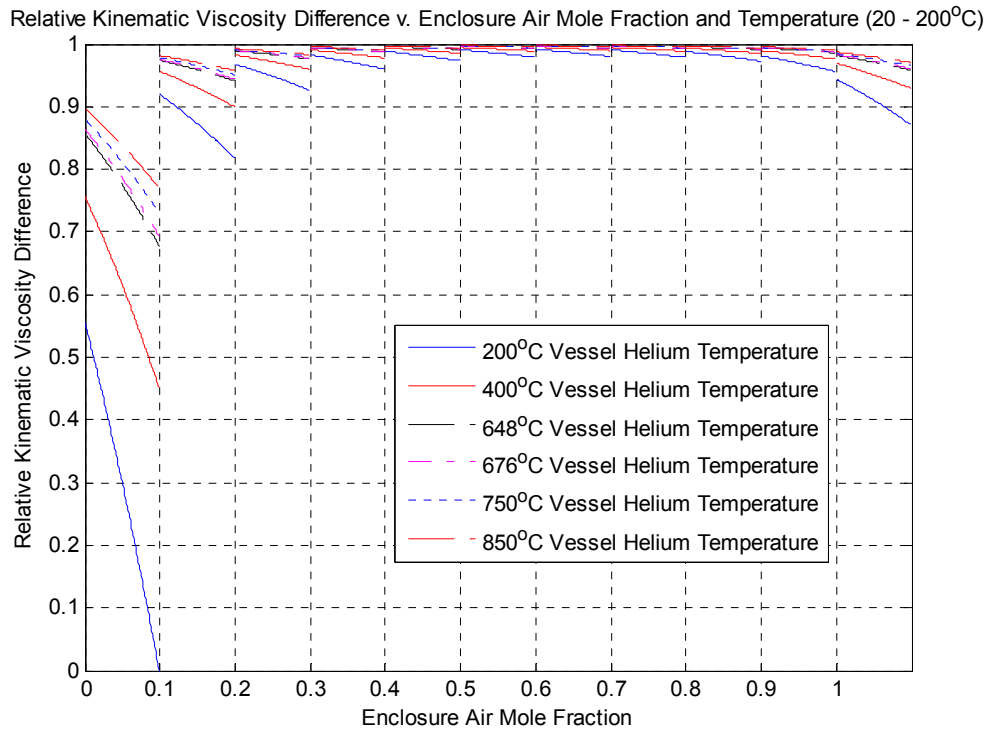
Figure 86. Relative kinematic viscosity difference with respect to vessel helium kinematic viscosity

Relative Specific Heat Capacity Differenc v. Enclosure Air Mole Fraction and Temperature (20 - 200°C)
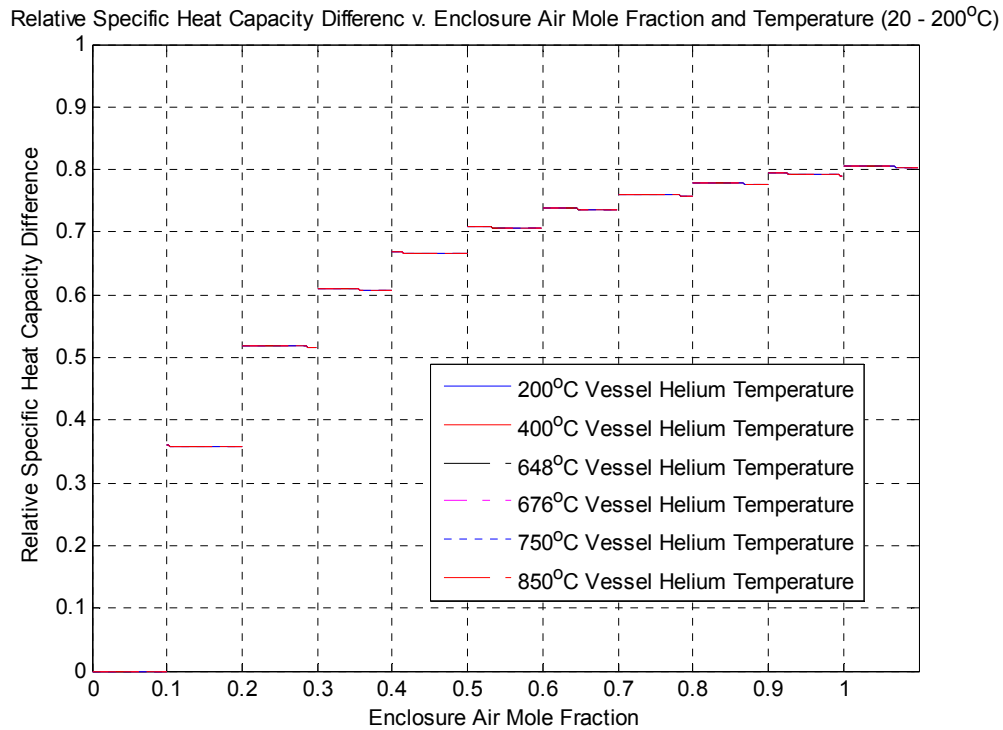
Figure 87. Relative specific heat capacity (SHC) difference with respect to vessel helium SHC

Relative Thermal Conductivity Difference v. Enclosure Air Mole Fraction and Temperature (20 - 200°C)
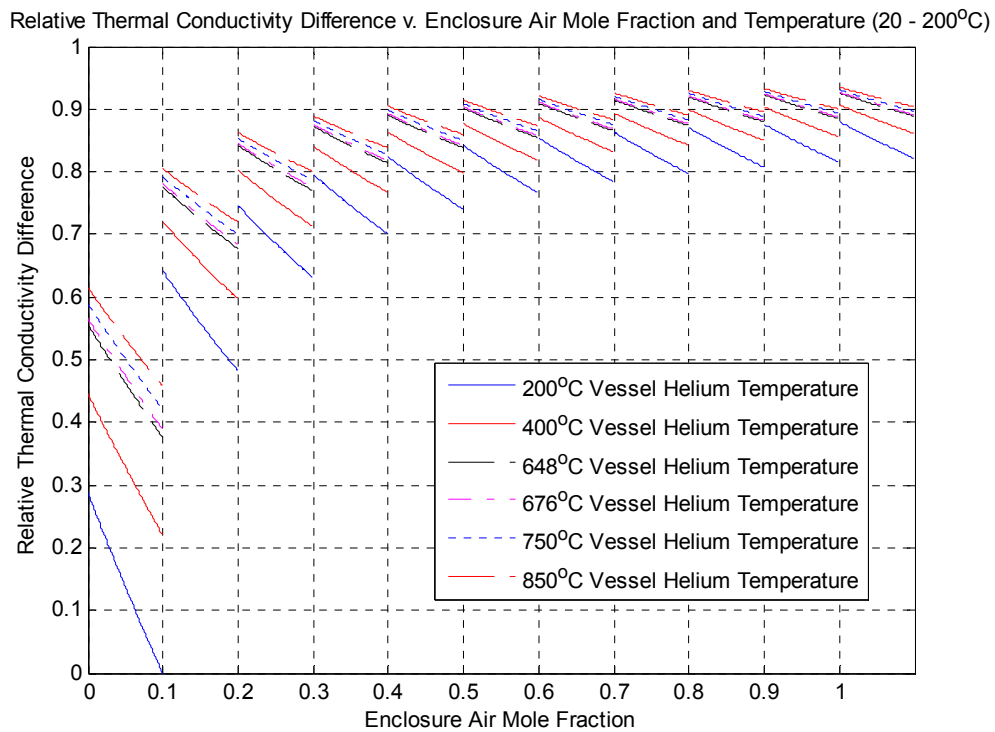
Figure 88. Relative thermal conductivity (TC) difference with respect to vessel helium TC
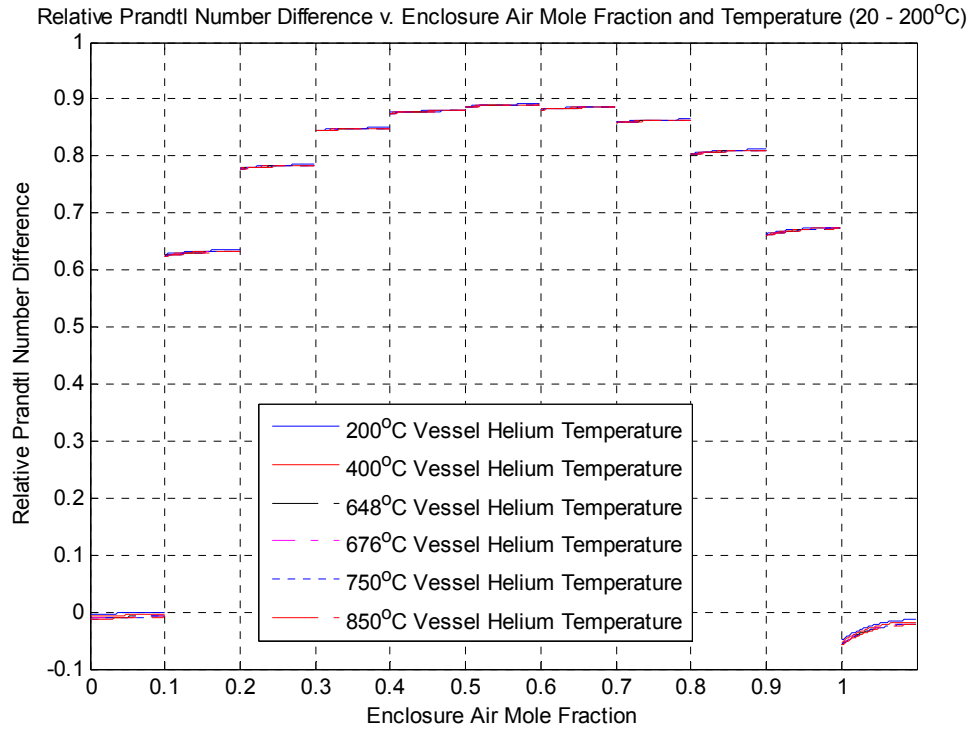
Figure 89. Relative Prandtl number difference; $(Pr_{ves} - Pr_{enc})/Pr_{ves}$
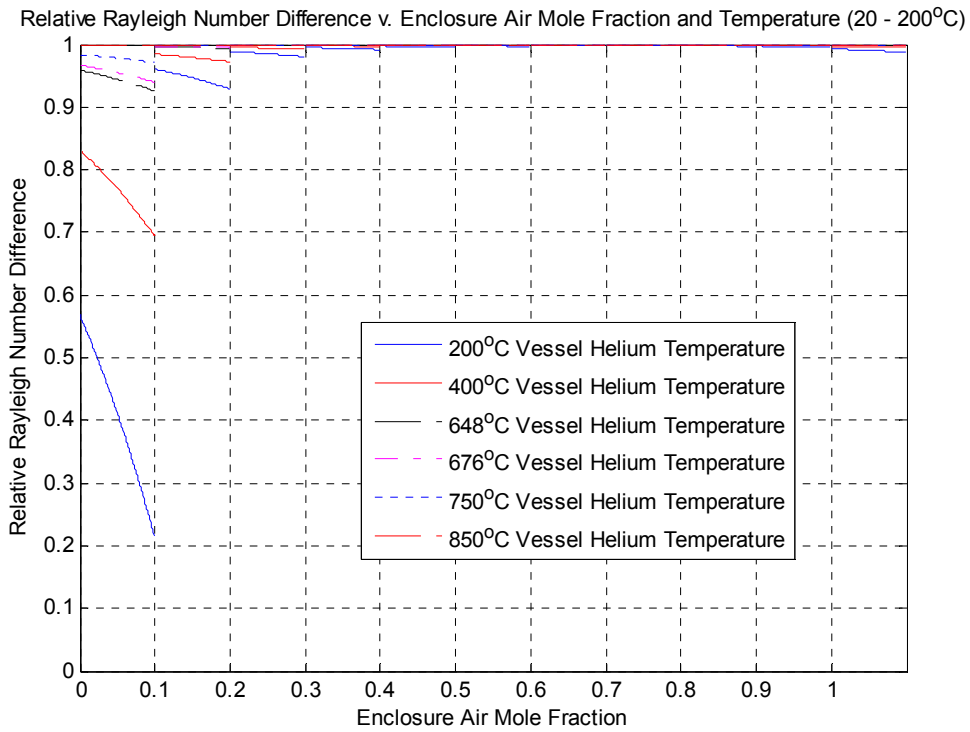
Figure 90. Relative Rayleigh (Ra) number difference with respect to enclosure mixture Ra
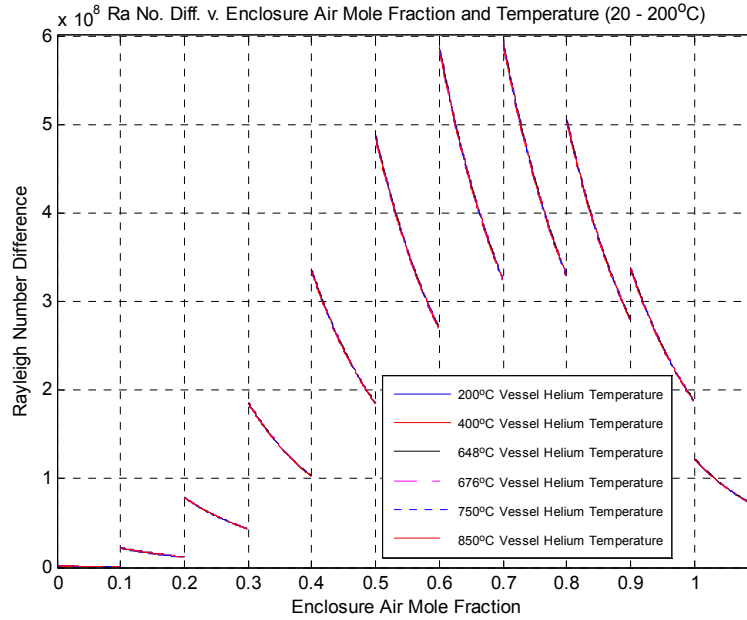
Figure 91. Absolute Rayleigh number difference

Table 28. Comparison of non-dimensional Froude (ND Fr) for 650°C Vessel

Case (Low Temp, Species)	Prototype Geometry ND Fr, 850°C	Scaled-down Geometry ND Fr, 650°C	Ratio
25°C, He	2.462e-3	2.717e-3	1.104
170°C, He	2.132e-3	2.257e-3	1.058
500°, He	1.003e-3	6.452e-4	0.644
25°C, Air	3.896e-3	4.107e-3	1.054
170°C, Air	3.198e-3	3.129e-3	0.978
500°, Air	2.372e-3	1.881e-3	0.793
25°C, Mixed Species	3.182e-3	3.139e-3	0.986
170°C, Mixed Species	2.663e-3	2.603e-3	0.978
500°, Mixed Species	2.297e-3	2.204e-3	0.960
		Average	0.951

Table 29. Comparison of non-dimensional friction number for 650°C Vessel

Case (Low Temp, Species)	Prototype Geometry ND Fr, 850°C	Scaled-down Geometry ND Fr, 650°C	Ratio
25°C, He	572	495	0.865
170°C, He	607	557	0.918
500°, He	1,108	1,690	1.525
25°C, Air	366	332	0.907
170°C, Air	412	393	0.954
500°, Air	467	556	1.191
25°C, Mixed Species	268	282	1.052
170°C, Mixed Species	314	325	1.035
500°, Mixed Species	350	352	1.006
		Average	1.050

From Figure 84 to Figure 91 and Table 28 and Table 29, it can be seen that there is not significant distortion due to lowering the experimental temperature to 650°C from 750°C.

Graphite Oxidation

When air enters into the reactor the high temperature graphite structures will have a chemical reaction with oxygen. The situation would cause a significant temperature increase from the exothermic reaction. This will cause damage to the structural integrity and accumulation of explosive and toxic *CO* gas in the reactor. Therefore, the graphite oxidation rate during experiment should be analyzed using FLUENT before the actual test.

The graphite oxidation is the reaction that the reactants can only come in and go out by diffusion due to the no-slip boundary condition at the wall. Therefore, the reactants mass flux by diffusion must equal the graphite reaction rate and the overall graphite reaction regime divided into three as shown in Figure 92

Regime 1: The temperature range is 673 to 900 K. This regime is called the chemical kinetic regime. Because the reaction rate is slow, there is enough time for the reactant material to diffuse into graphite pores. The reaction surface of pores is much more than the external graphite surface, the oxidation happens mostly inside graphite. Therefore, the reaction in this regime degrades the mechanical strength of the graphite components

Regime 2: The temperature range is 900 to 1123 K. The diffusion into the pores becomes limited with temperature increase. Even though the reaction rate increases exponentially with increasing temperature, the inability of the reactants to diffuse into the graphite, limits the amount of internal oxidation. Therefore, the graphite reaction eventually shifts to the external surface as the temperature increases.

Regime 3: The temperature range is over 1123 K. Since the reaction is fast, the reaction occurs on the external surface only. Since the available reactant is the limiting factor for this regime, only surface corrosion of the graphite components is observed.
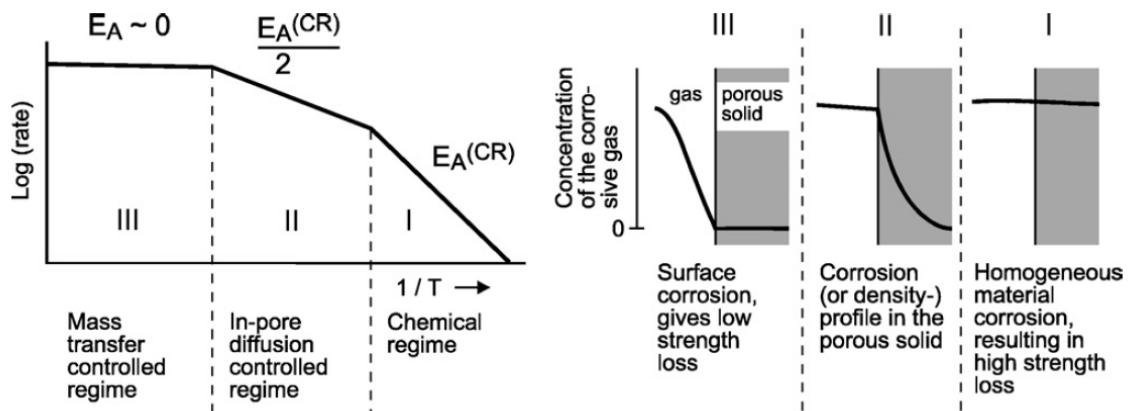
Figure 92. Graphite Oxidation Regimes

The reaction of graphite with oxygen would produce carbon dioxide and carbon monoxide.

$$C + xO_2 \rightarrow yCO + zCO_2 \qquad\qquad [60]$$

101

The stoichiometric values of *x,y,* and *z* are expressed as functions of the ratio, CO/CO_2. If $F = CO/CO_2$, then the stoichiometric values for O_2 depletion, x, would be: $x = \dfrac{F+2}{2(F+1)}$

While the CO and CO_2 generation, y and z, would be $y = \dfrac{F}{F+1}$, $z = \dfrac{1}{F+1}$

The ratio of CO/CO_2, $F = 7396 \exp\left(\dfrac{-69604}{RT}\right)$

Pressure Vessel Change of Materials

Alloy 800H has been the chosen design material for the pressure vessel material. It is an appropriate choice because of its low corrosion and high maximum allowable stress for elevated to high temperatures. Several quotes have been received for a pressure vessel constructed of Alloy 800H with different temperature and pressure design conditions. The most inexpensive option is a vessel with a design pressure condition of 35 psig and a design temperature condition of 750°C. This design costs $115,400. Table 30 shows the costs of pressure vessels with different design conditions. The design of this vessel is outlined in Figure 72 through Figure 83.

Table 30. Costs for Different Pressure Vessel Design Conditions

Option	Design Temperature Condition	Design Pressure Condition (psig)	Costs
1		60	$138,200
2	750°C	45	$134,300
3		35	$115,400

All three of these options exceed the available budget for a pressure vessel which is approximately $75,000. In order to reduce the costs of the vessel, one could do the following: (1) reduce the pressure rating of the vessel, (2) reduce the temperature rating of the vessel, or (3) change the material of the vessel. Since Option #3 already has a low pressure rating (35 psig), there is not much to gain from lowering the pressure rating in terms of saving costs. Also, there should be some kind of blowdown phase in the experiments. By lowering the pressure rating even more, further distorts the experimental results. By reducing the temperature rating of the vessel, minimal savings can be achieved since there is a small reduction in the amount of material that would be used. The third option is to change the material of the vessel. Looking at available options and considering maximum allowable stresses at high temperatures as well as costs, the alternative vessel material was chosen to be stainless steel 316 (SS316). The maximum allowable stress is among the highest of any stainless steel (11.2 ksi at 1050°F (565°C)). Additionally, it is significantly cheaper than Alloy 800H. On average, a metric ton of Alloy 800H is $20,500 while a metric ton of SS316 is $2,000. Also, when dealing with SS316, one can purchase that material in circular rings which is conducive for fabricating flanges economically. With Alloy 800H, the material cannot be purchased in circular rings but has to be purchased in blocks then machined to a certain shape. This presents considerable difference in the amount of material that would need to be purchased and a reduction in the amount of manual labor required to construct the vessel. Both point to an increased savings in final vessel costs. A quote for an SS316 pressure has not yet been received, but should be shortly.

One technical setback of using a high-temperature vessel constructed from SS316 as opposed to Alloy 800H is that in order for the vessel to be an ASME certified vessel, the maximum temperature at which the vessel can operate at 35 psig is 1050°F (565°C). This can be problematic since performing experiments at high temperatures (~750°C) is important in order to maintain similarity to the prototypic situation. In trying to understand what loads the vessel can actually support, some additional calculations were performed. The hoop stress that is exerted on the vessel when the chamber pressure is 30 psig is 2,010 psi. The maximum allowable stress for a SS316 vessel at 1300°F (705°C) is 4,100 psi. The number given for the maximum allowable stress is for an ASME certified vessel which allows for 100,000 hours of use. If the usage time is reduced to 1,000 hours, the maximum allowable stress increases significantly. In fact, for SS316 the rupture strength increases from 4,000 psi to 11,000 psi at 760°C as you decrease the usage time from 100,000 to 1,000 hours. This means that even with a SS316 vessel, we can collect data for high-temperature experiments while the vessel is initially pressurized to 30 psig.

Table 31. Design specifications for SS316 pressure vessel

Vessel Material	Design Pressure	Design Temperature	Cost
SS316	35 psig (241 kPa)	1050°F (565°C)	$71,600

Containment Vessel

A containment vessel has been designed as part of the air-ingress test facility. Its free volume is approximately 1 m^3. This free volume was established so that the air-to-helium mole ratio is preserved when the vessel is pressurized with helium to 30 psig. The top opening on the side of the vessel is to allow for the flexibility to run simulations while venting the containment. The bottom opening on the side wall is for vacuuming and charging the vessel. The openings below the flange are for thermocouple and O2 sensor insertion. Its dimensions are shown in Figure 93. The containment vessel joined to the pressure vessel is shown in Figure 94. The design for the containment vessel is different from the containment of the prototypic GT-MHR. In the prototypic case, the reactor vessel sits in the containment. That type of configuration would be difficult to simulate in an experimental setup since it makes access to the pressure vessel for maintenance and its instrumentation much more difficult. It is also more difficult to gain access to the camera and laser ports for the PIV system. Using two separate vessels, it allows for easier access to the pressure vessel. One drawback to this design is that it does not completely allow for the plume leaving the pressure vessel to follow the same path it would in the prototype geometry. To mitigate this drawback, the containment vessel is designed so that there is significant free volume above the flange connection. Also, the flange itself is close-coupled to the vessel so there is little to no flow obstruction as the plume exits into the containment vessel.

Table 32. Design specifications for SS304 containment vessel

Vessel Material	Design Pressure	Design Temperature	Cost
Stainless Steel 304	10 psig (69 kPa)	220°F (104°C)	$11,200
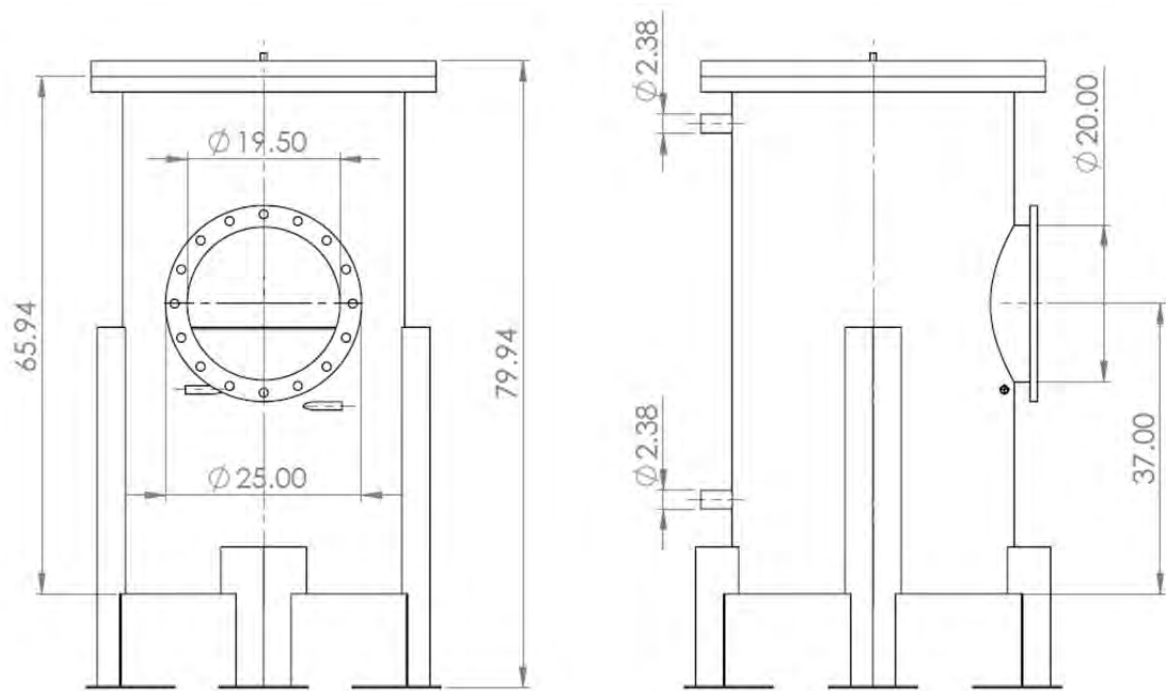
Figure 93. Front and side view of containment vessel
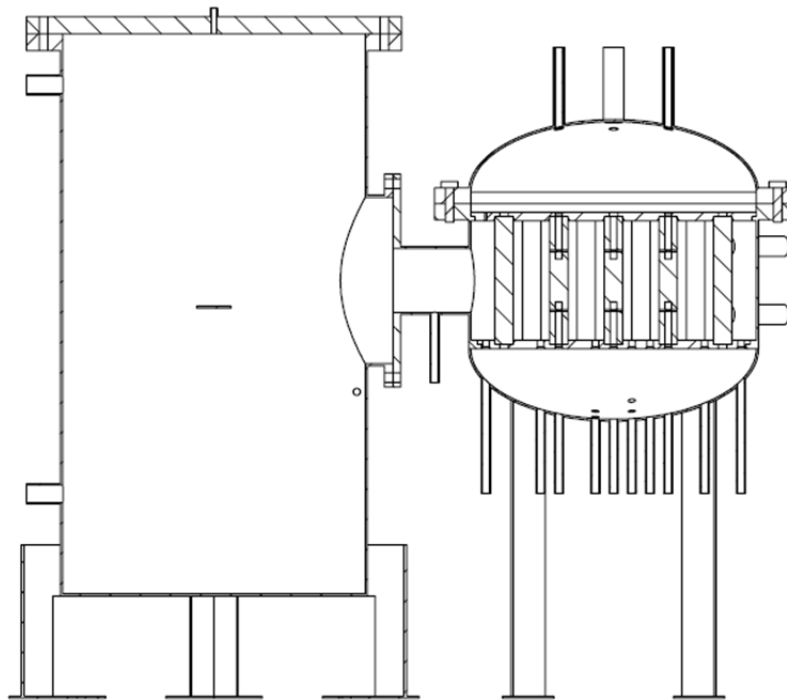
Figure 94. Containment vessel joined to the pressure vessel

Proposed Set of Experiments

A test matrix has been drafted which represents a minimum set of experiments for the air-ingress scenario as shown in Table 33. Four different types of breaks have been considered for use in the experiments. The first type is a double-ended guillotine (DEG) break. The second type is an axial break (AB) along the surface of the hot duct. The third type is circumferential break (CB) along the surface of the hot duct. The fourth type is a semicircle break (SB) on a flat plate at the end of the hot duct. The last three breaks can be oriented in different ways such as the break at the top (T), side (S), or bottom (B) of the duct. These breaks will be run for a set of pressurized and non-pressurized conditions all of which will maintain the proper air-to-helium mole ratio.

Table 33. Initial conditions and break geometry for minimum set of experiments

	Break Geometry									
	DEG	AB-T	AB-S	AB-B	CB-T	CB-S	CB-B	SB-T	SB-S	SB-B
Atm., 95%, 100%	X	X				X				
Atm., 88.8%, 100%	X	X	X	X	X	X	X			
Atm., 85%, 100%	X	X				X				
15 psig, 100%, 100%										
15 psig, 94.2%, 100%	X	X			X	X	X			
15 psig, 90%, 100%										
30 psig, 99.3%, 100%	X	X				X				
30 psig, 95%, 100%	X									
30 psig, 90%, 100%	X									

Table 33 shows the minimum set of proposed air-ingress experiments. The left most column has three numbers in each row. The first number is the initial pressure of the pressure vessel. The second number is the initial air concentration (by mole) in the containment vessel. The third number is the initial helium concentration (by mole) in the pressure vessel. The conditions which are in bold font maintain the air-to-helium mole ratio of the prototypic case – 5.15.

Experimental Procedure for Air-ingress Experiments

The scaled-down test facility is a 1/8th scaled-down model by length and by diameter of the hot exit plenum and the hot duct of the Very-High-Temperature Reactor (VHTR). The scaled-down test facility is comprised of two distinct vessels which are connected by a duct as shown in Figure 95. The vessel on the left simulates the containment of the prototypic design and is designated as the containment vessel. The design temperature and pressure of this vessel is 100°C at 25 psia (172 kPa) and is manufactured from 304 SS. The vessel on the right of Figure 95 simulates the hot exit plenum of the prototypic design and is designated as the pressure vessel. The design temperature and pressure of this vessel is 565°C at 50 psia (345 kPa) and is manufactured from 316 SS. The pressure vessel has a duct which is welded to its body that simulates the hot duct of the prototypic design. With a flange at its end, the hot duct joins the two vessels with a flange connection that is designed to be leak tight.
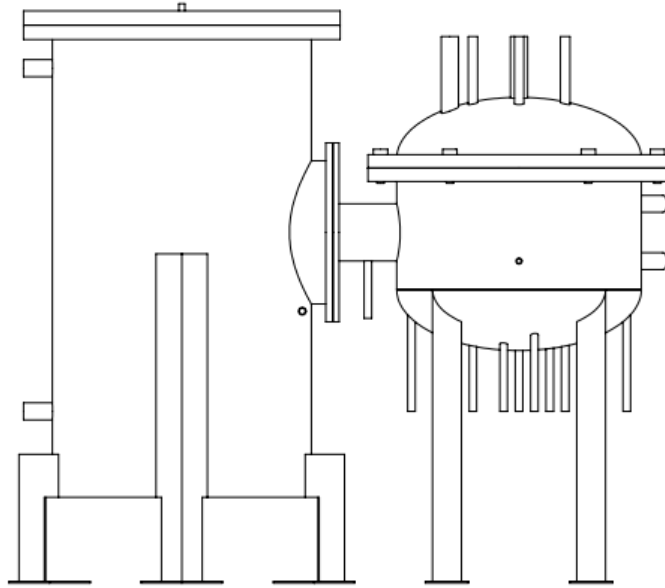
Figure 95. Schematic of scaled-down test facility comprised of containment vessel (left) and pressure vessel (right)

The proposed set of experiments that will be performed on the scaled-down test facility fall into one of the two categories: (i) pressurized experiments or (ii) non-pressurized experiments. The difference between pressurized and non-pressurized experiments is that pressurized experiments have an initial pressure in the pressure vessel that is greater than 14.7 psia (101 kPa) but less than or equal to 50 psia (345 kPa). Whereas, the initial pressure of the pressure vessel for non-pressurized experiments is 14.7 psia (101 kPa). Therefore, pressurized experiments include the phenomenon and effects of a depressurization in the air-ingress accident sequence.

Pressurized and non-pressurized experiments are both considered in the test matrix of the air-ingress experiments because both sets of experiments have a distinct advantage. Pressurized experiments take into account the effect of a depressurization during the air-ingress accident. On the other hand, non-pressurized experiments will prolong the use of the experimental facility. Since these non-pressurized experiments will be performed with the initial pressure of the pressure vessel at atmospheric pressure, there will be less strain on the facility as compared to pressurized experiments. These experiments, however, will not take into account the effect of a depressurization during the air-ingress accident.

In both types of experiments, experimental parameters are adjusted to establish the desired density difference between the helium gas in the pressure vessel and the air-helium gas mixture in the containment vessel. As shown in the scaling analysis of the design, the density difference is the principal driving force of the density-driven air ingress phenomenon. The initial density difference is the initial condition for the proposed set of experiments. For pressurized experiments, there are three experimental parameters that can be controlled to properly establish the initial condition of the experiment. These three parameters are the (1) initial temperature of the helium gas in the pressure vessel, the (2) initial pressure of the helium gas in the pressure vessel, and the (3) initial mole ratio of the air-helium gas mixture in the containment vessel. For non-pressurized experiments, there are two experimental parameters that can be controlled to properly establish the initial condition of the experiment. These two

parameters are the (1) initial temperature of the helium gas in the pressure vessel and the (2) initial mole ratio of the air-helium gas mixture in the containment vessel. For all experiments, the initial pressure of the air-helium gas mixture in the containment vessel is 14.7 psia (101 kPa), while the initial temperature of the air-helium gas mixture in the containment vessel is approximately at ambient temperature (~20°C). The exact temperature of the air-helium gas temperature will be measured with thermocouples positioned at various locations in the containment vessel. Table 34 summarizes the range of the experimental parameters available for establishing the initial condition or initial density difference of the experiment.

Table 34. Range of experimental parameters to set the initial condition of the experiment

	Pressurized Experiments		Non-Pressurized Experiments	
	Pressure Vessel	Containment Vessel	Pressure Vessel	Containment Vessel
Pressure (kPa)	101 < P ≤ 345	P = 101	P = 101	P = 101
Gas Temperature (°C)	20 ≤ T ≤ 700	T = ~20	20 ≤ T ≤ 700	T = ~20
Helium Mole Fraction	y_{he} = 1	$0 ≤ y_{he} ≤ 1$	y_{he} = 1	$0 ≤ y_{he} ≤ 1$

From Table 34, the maximum gas temperature of the pressure vessel is 700°C, yet, as previously stated, the design temperature and pressure of the pressure vessel is 565°C at 50 psia (345 kPa). This design condition is based on 100,000 hours of vessel use. Since the prototypic temperatures of the VHTR are near 850°C, it is desirable to perform some experiments closer to the prototypic temperature than 565°C. To determine the vessel's capacity to withstand stress due to elevated pressures and high temperatures, the hoop stress was calculated for the pressure vessel at the upper limit of its design specifications. A similar calculation was not performed for the containment vessel because the pressure and gas temperatures are well below the vessel design conditions. The hoop stress is calculated for a thin-walled cylinder since the inner radius of the vessel (*r* = 16.75") is more than five times the vessel wall thickness (*t* = 0.25"). The hoop stress (σ) is calculated based on the following equation:

$$\sigma = \frac{pr}{t}$$

[46]

For a pressure differential (*p*) of 35 psid, which is consistent with the pressure vessel being charged to 50 psia (345 kPa), the hoop stress exerted on the vessel is 2,345 psi or 2.35 ksi. For 1,000 hours of vessel use and a vessel temperature of 704.4°C (1300°F), the rupture strength of the 316 SS pressure vessel is approximately 16.5 ksi as shown by marker 1 in Figure 96. For 10,000 hours of vessel use and a vessel temperature of 704.4°C (1300°F), the rupture strength of the 316 SS pressure vessel is approximately 11 ksi as shown by marker 2 in Figure 96. For 100,000 hours of vessel use and a vessel temperature of 704.4°C (1300°F), the rupture strength of the 316 SS pressure vessel is approximately 8.5 ksi as shown by marker 3 in Figure 96. This means that the vessel can be operated for several thousands of hours (1,000 to 10,000 hours) at temperatures around 700°C and at pressures of 50 psia and the rupture strength of the vessel will be 4.7 to 7.0 times greater than the actual hoop stress exerted on the vessel. This will allow for some experiments to be performed on the scaled-down facility where the initial helium temperature in the pressure vessel is 700°C and the initial helium pressure in the pressure vessel is 50 psia (345 kPa).

While the scaled-down test facility; more specifically, the pressure vessel, is capable of withstanding hoop stresses for temperature and pressure conditions up to 700°C at 50 psia (345 kPa) for a reduced vessel lifetime, thereby allowing some high-temperature experiments to be carried out that exceed the temperature condition imposed by the ASME Boiler & Pressure Vessel Code for this specific vessel, it would also be advantageous to conduct well-scaled experiments in which the initial helium temperature in the pressure vessel is at a lower temperature. The main reasons that the addition of lower temperature experiments is preferable to exclusively performing high-temperature experiments is as follows: (1) it prolongs the life of the pressure vessel by reducing the thermal fatigue to the vessel and its joints; (2) it prolongs the life of the graphite support columns in the pressure vessel by reducing the rate of graphite oxidation; (3) the amount of time required to bring the test facility up to the desired initial temperature is reduced, this will increase the number of experiments that can be performed; (4) it prolongs the life of the in-situ instrumentation such as thermocouples and oxygen sensors, this will reduce cost and maintenance time.
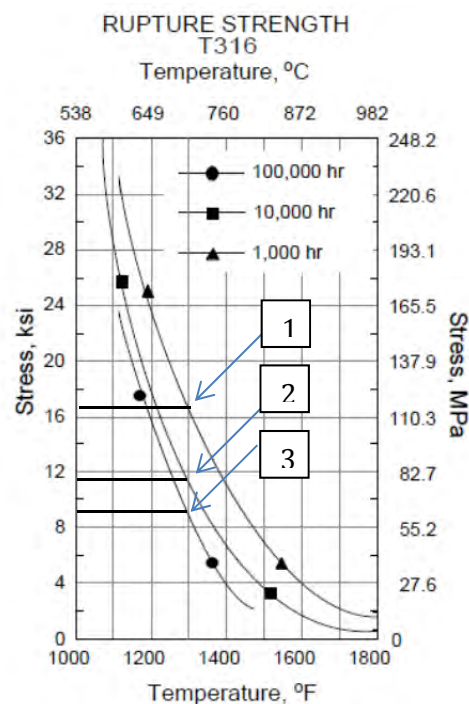
Figure 96. Rupture strength as a function of vessel usage time and vessel temperature[22]

The oxidation of graphite is a temperature dependent phenomenon. Depending on the temperature of the graphite, its oxidation is controlled by different regimes. From the available literature[25, 26], three graphite oxidation regimes have been established: the chemical regimes, the in-pore diffusion controlled regime, and the boundary layer controlled regime. At low temperatures, the reaction between the graphite and the oxidizing gas occurs very slowly and the oxidizing gases can penetrate deeply into the graphite. This means that the concentration of the oxidizing gases and the resulting oxidation are nearly uniform through the whole depth of the penetration. In this regime, the oxidation rate is controlled purely by chemical reactivity. At elevated temperatures, the oxidation falls into the in-pore diffusion controlled regime, which is between the chemical regime and the boundary layer controlled regime. The oxidation rate is controlled by a combination of in-pore diffusion and chemical reaction. In this regime, the concentration of reactant and therefore burn-off varies exponentially in depth, giving rise to what is known as an oxidation burn-off profile. At high temperatures, the chemical reactivity is so

108

high that all the oxidizing gases react at the surface of the hot graphite. The concentration of oxidizing gases varies sharply at the graphite surface. The oxidation is severe at the exterior surface of the graphite block and changes the geometry of the graphite body without damaging the interior material.

In the literature[27], temperature limits are set for each regime of oxidation for air. At temperatures below 500°C, the oxidation belongs to the chemical regime. Between 500 and 900°C, the oxidation belongs to the in-pore diffusion controlled regime. At temperatures over 900°C, the oxidation belongs to the boundary layer regime. Figure 97 shows how much of the IG-110 graphite oxidizes with respect to temperature after 4 h of exposure to air at a given graphite temperature. It can be seen that the amount of graphite oxidation increases as temperature increases and that the amount of oxidation begins to increase significantly as the graphite temperature passes 500°C. This suggests that in order to preserve the life of the graphite support columns the initial temperature of the experiment should be at or below 500°C. Some high-temperature experiments can be performed; however, this will account for a higher rate of graphite oxidation. This will allow for fewer experiments to be performed for a given set of columns. Also, this shows that the rapid removal of air from the pressure vessel after the completion of an experiment is an important aspect to the experimental procedure.
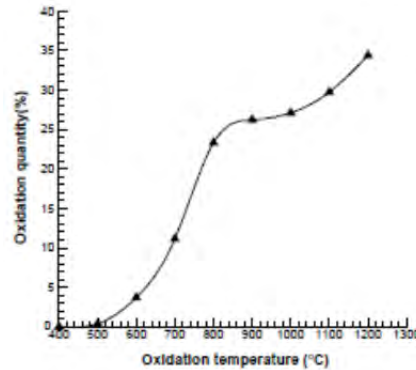
Figure 97. Oxidation quantities for different temperatures[27]

Table 35. Thermal mass of the pressure vessel and its internal structures

	Material Volume (m^3)	Density (kg/m^3)	Mass (kg)	Average Heat Capacity (J/(kg·K))	Thermal Mass (J/K)
Stainless Steel 316	0.08334	8000	666.72	542	361,000
IG-11 Graphite	0.04863	1770	86.07	1353	116,000
Ceramic Balls	0.19319	1400	270.46	840	227,000
Helium Gas (50 psia, 293K)	0.20983	0.5663	0.12	3116 (constant vol.)	374

Another important experimental consideration is the time required to raise the temperature of the pressure vessel and its internal structures from the ambient temperature, which is approximately 20°C, to the desired initial temperature of the experiment. The pressure vessel and its internal structures, which consists of graphite rods and ¼" ceramic balls, constitute a significant amount of thermal mass. The graphite rods are constructed of IG-11 graphite and the ceramic balls are fabricated primarily from silicon oxide (80 wt. %) and aluminum oxide (13 wt. %). The material volume, material density, mass, average heat capacity and thermal mass of the pressure vessel material (316 SS) and its internal structures are listed in Table 35. The

average heat capacity of stainless steel 316 and IG-11 graphite are calculated by applying the mean value theorem for integrals over the interval from 20-700°C to the specific heat capacity correlation, c(T), which is derived from experimental data[28, 29].

From the First Law of Thermodynamics, the amount of energy required to raise the temperature of the pressure vessel can be calculated.   In this case, work done by the control volume is neglected and the change in kinetic and potential energy is also neglected. This leaves eq. [47].

$$\Delta U = Q \qquad [47]$$

 Eq. [48] shows the eq. [47] in more explicit terms:

$$Q = m_{316}\int_{20}^{T} c_{316}(T')\,dT' + m_{11}\int_{20}^{T} c_{11}(T')\,dT' + m_{cer}c_{cer}(T-20) + m_{he}c_{v,he}(T-20) \qquad [48]$$

The mass of each material is given in Table 35. $m_{316}, m_{11}, m_{cer}, m_{he}$ is the mass of stainless steel 316, IG-11 graphite, ceramic, and helium, respectively. The heat capacity expressions of stainless steel 316 and IG-11 graphite are given in eq. [49] and [50]:

$$c_{316}(T) \;=\; -0.0016T^2 + 2.66T + 664.37 \qquad [49]$$

$$c_{11}(T) \;=\; 0.2386T + 456.25 \qquad [50]$$

Table 36. Time required to attain various final heat-up temperatures

Final Temperature (°C)	Energy Required to Attain Final Temperature (MJ)	Minimum Heat-up Time (h)
100	48.9	1.13
300	181.05	4.19
500	325.38	7.53
700	479.72	11.10

The heat capacity of the ceramic balls and helium are constant values of 840 J/(kg·K) and 3,116 J/(kg·K), respectively. Table 36 shows the amount of energy required to raise the temperature of the pressure vessel material and its internal components from 20°C to various final temperatures. The heat-up time is based on a series of heaters that supply a constant power of 12 kW to the pressure vessel system for the duration of the heat-up period. Therefore, it is assumed that the heaters can operate at their maximum power output for the duration of the heat-up process. In reality, this may not be possible since the thermal conductivity of stainless steel 316 (~20 W/(m·K)) and ceramic (~1 W/(m·K)) is low. This could result in the heaters exceeding their maximum allowable temperature of 900°C and becoming ruined. Also, in this calculation, heat losses from the system are neglected. Therefore, the heat-up times given in Table 36 represent the minimum heat-up time to attain the given final temperature for the pressure vessel system. It can be seen that as the final temperature increases, the heat-up

time increases. Therefore, if more lower-temperature experiments were part of the test matrix, more experiments could be performed.

A test matrix (Table 37) has been drafted which represents an initial set of experiments for the air-ingress scenario. Four different types of breaks have been considered for use in the experiments. The first type is a double-ended guillotine (DEG) break (Fig. 88a). The second type is a semicircle break (SB) on a flat plate at the end of the hot duct (Fig. 88b). The third type is a circumferential break (CB) along the surface of the hot duct (Fig. 88c). The fourth type is a slit break (SlB) on a flat plate at the end of the hot duct (Fig. 88d). The last three breaks can be oriented in different ways such as the break at the top (T), side (S), or bottom (B) of the duct. In the test matrix , experiments are distinguished by varying the break geometry and orientation, the initial pressure vessel temperature, the initial pressure vessel pressure, and the initial containment vessel air/helium mole ratio. This allows one to see how each parameter or phenomenology affects the air-ingress scenario. Those effects which are taken into consideration by varying the parameters of the experiment are molecular diffusion, density difference due to a concentration difference, temperature effects which can enhance the density-driven flow, pressure effects and break geometry effects. There are still some experiments for which the initial parameters remain undecided such as initial pressure vessel pressure and initial containment vessel air/helium mole ratio. Initial density difference cannot be calculated for pressurized experiments. It is difficult to predict how much air and/or helium will leave the containment vessel during the depressurization.

(a) Double-ended Guillotine Break

(b) Semicircle Break

(c) Circumferential Break

(d) Slit Break
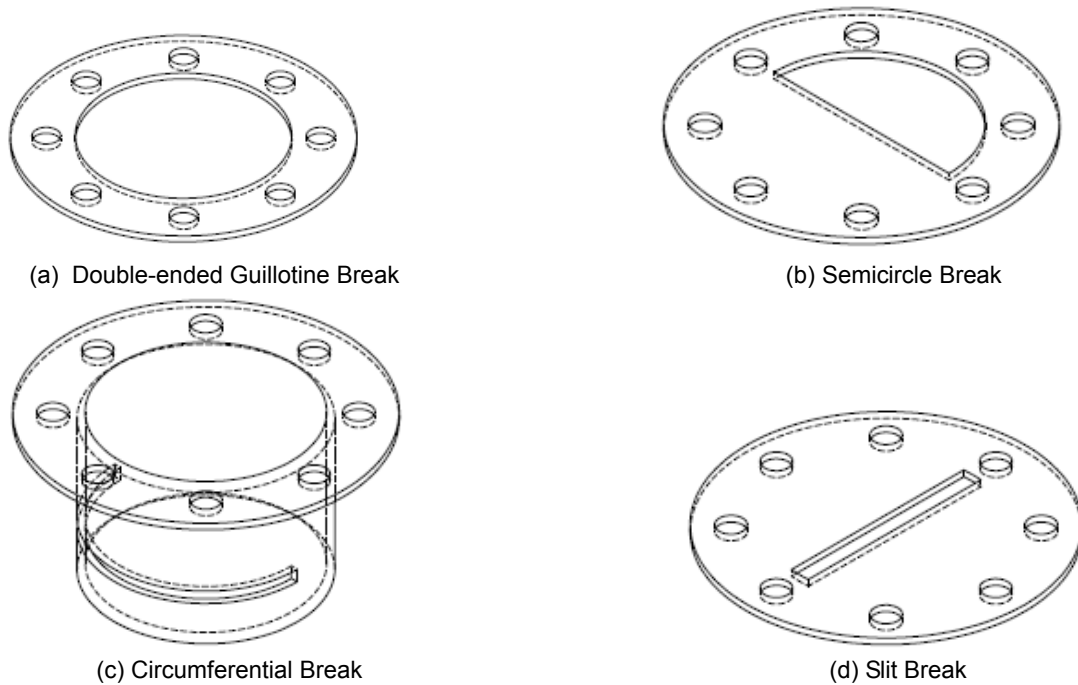
Figure 98. Break and slit plates for air-ingress experiments on the scaled-down test facility

Table 37. Initial set of proposed air-ingress experiments

	Experiment Number	Break Type/Orientation	Initial Pressure Vessel Temperature (°C)	Initial Pressure Vessel Pressure (psig)	Initial Containment Vessel Air/He Mole Ratio	Initial Density Difference (kg/m^3)
MD	1	DEGB (2A)	Ambient Temp. (~20)	0	1:99 (or 2x O2 lower limit)	0.0104

DDC	2	DEGB	Ambient Temp. (~20)	0	1:3	0.2595
DDC	3	DEGB	Ambient Temp. (~20)	0	1:1	0.5189
DDC	4	DEGB	Ambient Temp. (~20)	0	3:1	0.7784
DDC	5	DEGB	Ambient Temp. (~20)	0	1:0	1.0378
P, MD	6	DEGB	Ambient Temp. (~20)	30	1:99	
P, DDC	7	DEGB	Ambient Temp. (~20)	30	1:3	
P, DDC	8	DEGB	Ambient Temp. (~20)	30	1:1	
P, DDC	9	DEGB	Ambient Temp. (~20)	30	3:1	
P, DDC	10	DEGB	Ambient Temp. (~20)	30	1:0	
P, DDC	11	DEGB	Ambient Temp. (~20)	15	1:1	
P, G, DDC	12	SB-T (0°)	Ambient Temp. (~20)	0, 15 or 30?	1:1?	
P, G, DDC	13	SB-45 (45°)	Ambient Temp. (~20)	0, 15 or 30?	1:1?	
P, G, DDC	14	SB-S (90°)	Ambient Temp. (~20)	0, 15 or 30?	1:1?	
P, G, DDC	15	SB-135 (135°)	Ambient Temp. (~20)	0, 15 or 30?	1:1?	
P, G, DDC	16	SB-B (180°)	Ambient Temp. (~20)	0, 15 or 30?	1:1?	
P, G, DDC	17	CB-T (0°)	Ambient Temp. (~20)	0, 15 or 30?	1:1?	
P, G, DDC	18	CB-45 (45°)	Ambient Temp. (~20)	0, 15 or 30?	1:1?	
P, G, DDC	19	CB-S (90°)	Ambient Temp. (~20)	0, 15 or 30?	1:1?	
P, G, DDC	20	CB-135 (135°)	Ambient Temp. (~20)	0, 15 or 30?	1:1?	
P, G, DDC	21	CB-B (180°)	Ambient Temp. (~20)	0, 15 or 30?	1:1?	
P, G, DDC	22	SIB (0°)	Ambient Temp. (~20)	0, 15 or 30?	1:1?	
P, G, DDC	23	SIB (45°)	Ambient Temp. (~20)	0, 15 or 30?	1:1?	
P, G, DDC	24	SIB (90°)	Ambient Temp. (~20)	0, 15 or 30?	1:1?	
T, MD	25	DEGB	100	0	1:99	0.0461
T, DDC	26	DEGB	100	0	1:3	0.2951
T, DDC	27	DEGB	100	0	1:1	0.5546
T, DDC	28	DEGB	100	0	3:1	0.8140
T, DDC	29	DEGB	100	0	1:0	1.0735
P, T, DDC	30	DEGB	100	30	1:99	
P, T, DDC	31	DEGB	100	30	1:3	
P, T, DDC	32	DEGB	100	30	1:1	
P, T, DDC	33	DEGB	100	30	3:1	
P, T, DDC	34	DEGB	100	30	1:0	
P, T, DDC	35	DEGB	100	15	1:1	
T, P, G, DDC	36	SB-T (0°)	100	0, 15 or 30?	1:1?	
T, P, G, DDC	37	SB-45 (45°)	100	0, 15 or 30?	1:1?	
P, T, G, DDC	38	SB-S (90°)	100	0, 15 or 30?	1:1?	
T, P, G, DDC	39	SB-135 (135°)	100	0, 15 or 30?	1:1?	
T, P, G, DDC	40	SB-B (180°)	100	0, 15 or 30?	1:1?	
T, P, G, DDC	41	CB-T (0°)	100	0, 15 or 30?	1:1?	
T, P, G, DDC	42	CB-45 (45°)	100	0, 15 or 30?	1:1?	
T, P, G, DDC	43	CB-S (90°)	100	0, 15 or 30?	1:1?	
T, P, G, DDC	44	CB-135 (135°)	100	0, 15 or 30?	1:1?	
T, P, G, DDC	45	CB-B (180°)	100	0, 15 or 30?	1:1?	
T, P, G, DDC	46	SIB (0°)	100	0, 15 or 30?	1:1?	
T, P, G, DDC	47	SIB (45°)	100	0, 15 or 30?	1:1?	
T, P, G, DDC	48	SIB (90°)	100	0, 15 or 30?	1:1?	
T, MD	49	DEGB	400	0	1:99 (or 2x O2 lower limit)	0.1043
T, DDC	50	DEGB	400	0	1:3	0.3534
T, DDC	51	DEGB	400	0	1:1	0.6128
T, DDC	52	DEGB	400	0	3:1	0.8723
T, DDC	53	DEGB	400	0	1:0	1.1318
P, T, DDC	54	DEGB	400	30	1:99	
P, T, DDC	55	DEGB	400	30	1:3	
P, T, DDC	56	DEGB	400	30	1:1	
P, T, DDC	57	DEGB	400	30	3:1	
P, T, DDC	58	DEGB	400	30	1:0	
P, T, DDC	59	DEGB	400	15	1:1	

T, P, G, DDC	60	SB-T (0°)	400	0, 15 or 30?	1:1?	
T, P, G, DDC	61	SB-45 (45°)	400	0, 15 or 30?	1:1?	
T, P, G, DDC	62	SB-S (90°)	400	0, 15 or 30?	1:1?	
T, P, G, DDC	63	SB-135 (135°)	400	0, 15 or 30?	1:1?	
T, P, G, DDC	64	SB-B (180°)	400	0, 15 or 30?	1:1?	
T, P, G, DDC	65	CB-T (0°)	400	0, 15 or 30?	1:1?	
T, P, G, DDC	66	CB-45 (45°)	400	0, 15 or 30?	1:1?	
T, P, G, DDC	67	CB-S (90°)	400	0, 15 or 30?	1:1?	
T, P, G, DDC	68	CB-135 (135°)	400	0, 15 or 30?	1:1?	
T, P, G, DDC	69	CB-B (180°)	400	0, 15 or 30?	1:1?	
T, P, G, DDC	70	SIB (0°)	400	0, 15 or 30?	1:1?	
T, P, G, DDC	71	SIB (45°)	400	0, 15 or 30?	1:1?	
T, P, G, DDC	72	SIB (90°)	400	0, 15 or 30?	1:1?	
T, MD	73	DEGB	700	0	1:99 (or 2x O2 lower limit)	0.1267
T, DDC	74	DEGB	700	0	1:3	0.3757
T, DDC	75	DEGB	700	0	1:1	0.6352
T, DDC	76	DEGB	700	0	3:1	0.8946
T, DDC	77	DEGB	700	0	1:0	1.1541
P, T, DDC	78	DEGB	700	30	1:99	
P, T, DDC	79	DEGB	700	30	1:3	
P, T, DDC	80	DEGB	700	30	1:1	
P, T, DDC	81	DEGB	700	30	3:1	
P, T, DDC	82	DEGB	700	30	1:0	
P, T, DDC	83	DEGB	700	15	1:1	
T, P, G, DDC	84	SB-T (0°)	700	0, 15 or 30?	1:1?	
T, P, G, DDC	85	SB-45 (45°)	700	0, 15 or 30?	1:1?	
T, P, G, DDC	86	SB-S (90°)	700	0, 15 or 30?	1:1?	
T, P, G, DDC	87	SB-135 (135°)	700	0, 15 or 30?	1:1?	
T, P, G, DDC	88	SB-B (180°)	700	0, 15 or 30?	1:1?	
T, P, G, DDC	89	CB-T (0°)	700	0, 15 or 30?	1:1?	
T, P, G, DDC	90	CB-45 (45°)	700	0, 15 or 30?	1:1?	
T, P, G, DDC	91	CB-S (90°)	700	0, 15 or 30?	1:1?	
T, P, G, DDC	92	CB-135 (135°)	700	0, 15 or 30?	1:1?	
T, P, G, DDC	93	CB-B (180°)	700	0, 15 or 30?	1:1?	
T, P, G, DDC	94	SIB (0°)	700	0, 15 or 30?	1:1?	
T, P, G, DDC	95	SIB (45°)	700	0, 15 or 30?	1:1?	
T, P, G, DDC	96	SIB (90°)	700	0, 15 or 30?	1:1?	

Phenomenology:
MD – molecular diffusion
DDC – density difference due to concentration difference
T – temperature effects
P – pressure effects
G – break geometry effects

Break Type:
DEGB – Double-Ended Guillotine Break
SB – Semicircle Break
CB – Circumferential Break
SIB – Slit Break

Break Orientation:
T – Top
B – Bottom
S - Side

CFD simulation of the scaled-down test facility

In order to perform CFD calculations of scaled-down test facility, half symmetric grid model was generated as shown in Figure 99. The experiment number 34, 58, and 82 which are suggested in Table 37 were performed. All of the cases are DEGB test with the initial temperatures in the vessel are 373, 673, and 973 K respectively, and 293 K in the containment. The initial pressure was set to 0.3 and 0.1 MPa in the vessel and containment, respectively.

The fluent specification and model used in this calculation are listed as follows:

- Solver
    - Solver : Pressure-Based
    - Time : Transient
    - Pressure Velocity coupling: PISO
    - Transient Formulation : First Order Implicit

- Discretization
    - Pressure : PRESTO!
    - Momentum : 2nd order upwind
    - Species : 2nd order upwind
    - Energy : 2nd order upwind

- K-ε standard turbulence

- Species transport model
    - Mixture material: Mixturetemplate
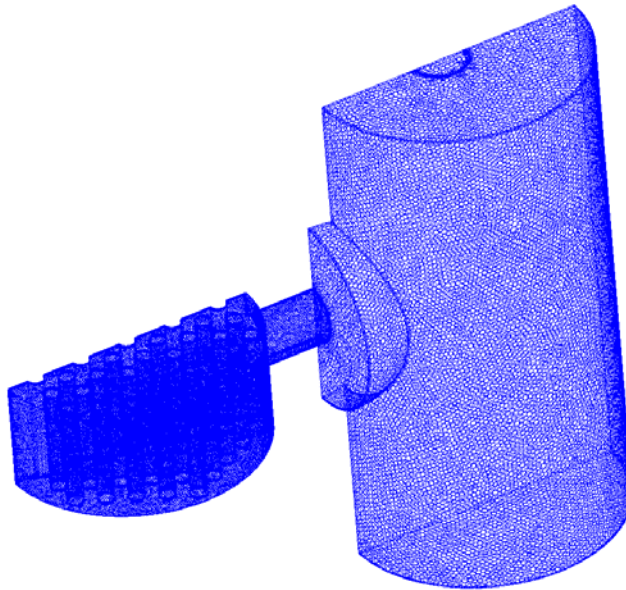   - 2 species: Air and Helium

Figure 99. CFD model of scaled down test facility

Figure 100 shows the temperature change during depressurization for the experiment 82. The simulations were performed with two different sets of boundary conditions and were compared with isentropic case. One case is when no heat is transferred from internal structure, and the other is when the inside structure temperature is fixed as 973 K. The maximum deviation of no heat flux case and constant temperature case from isentropic are 2 and 0.5 %, respectively. It shows the depressurization process can be calculated with 1D analysis by assuming constant enthalpy.

The sudden temperature decrease during the depressurization process is recovered in a short time as shown in Figure 101. The instantaneous maximum heat flux reaches 143, 106, and 78 kW for wall temperature 973, 673, and 373 K respectively. Therefore, the temperatures are recovered in a second as shown in Figure 101.
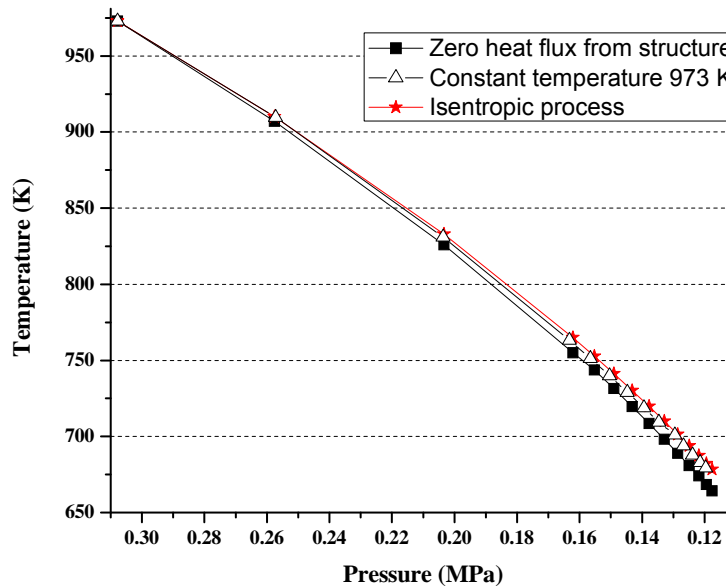

Figure 100. Temperature decrease due to pressure change during depressurization for experiment 82
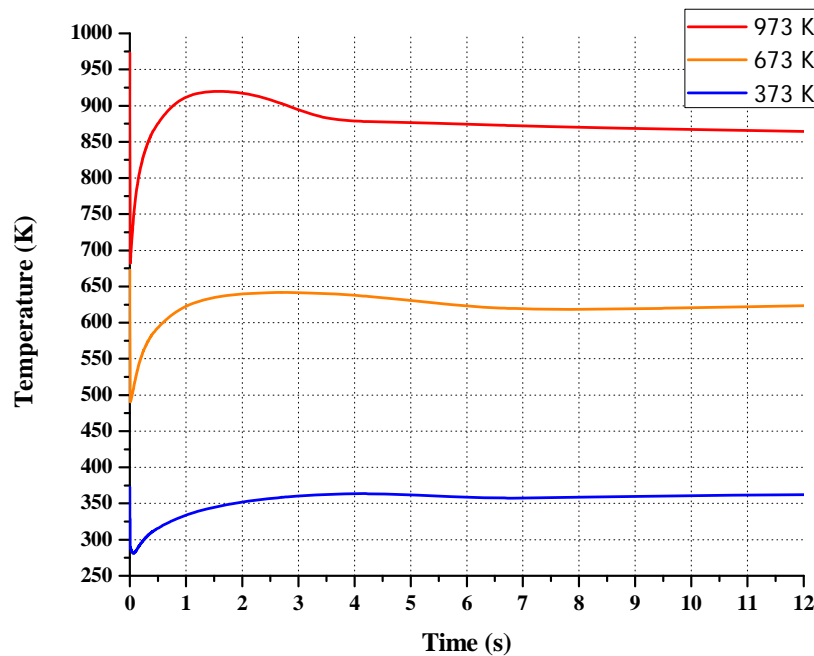

Figure 101. Overall average temperature changes in a vessel for experiment 35,58, and 82

115

After the temperature recovery, a slight temperature decrease can be found which is more dominant for the higher wall temperature case. Once density driven flow is initiated, the relatively cold fluid from containment enters through the vessel bottom. Before the plume reaches the end of the vessel, the Figure 102 (c) shows the plume is higher than the plume that reaches the end of the vessel. This is possibly due to the fact that the flow is not fully developed and stays in the vessel more time. After the plume reaches the vessel back and the circulation is established, the temperature maintains constant.

The streamline shows the flow circulation after the plume reaches the vessel end. However, the flow circulation does not reach to the top of the vessel. Instead, the level of the incoming air mixture gradually increases as shown in Figure 103.
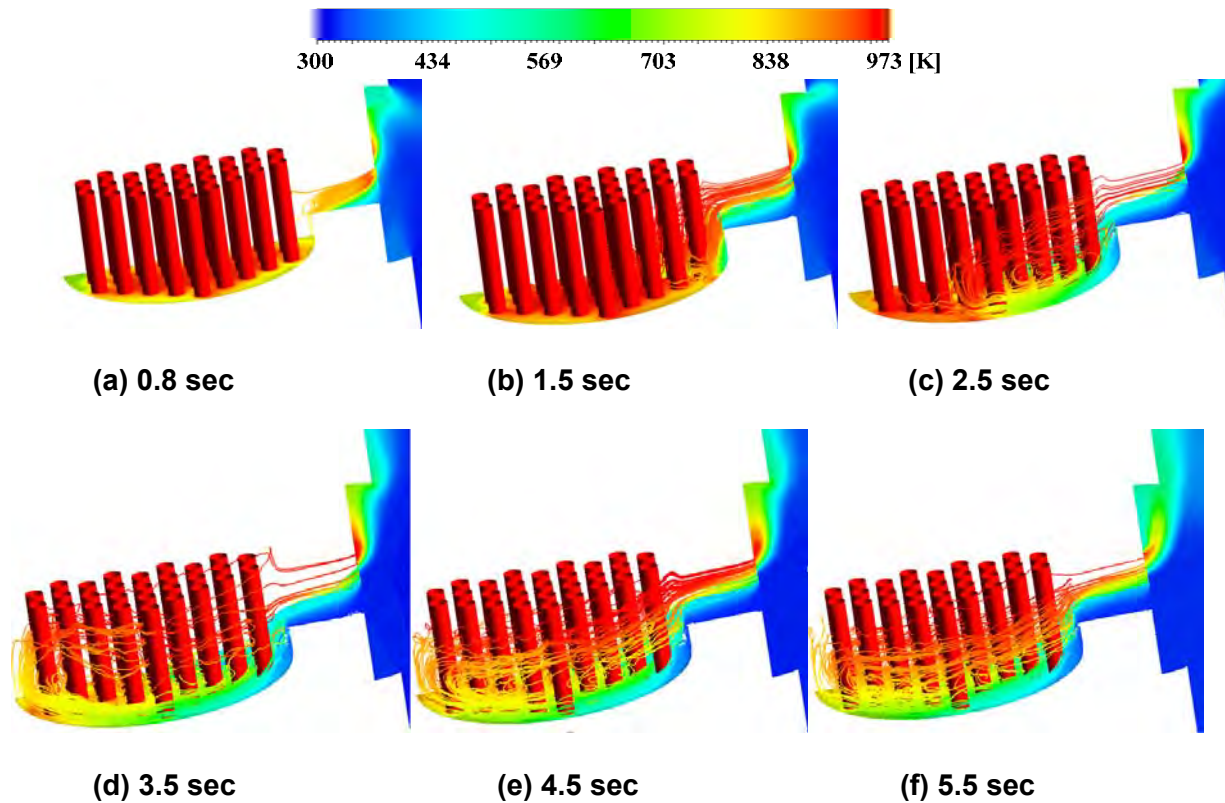

| (a) 0.8 sec | (b) 1.5 sec | (c) 2.5 sec |

| (d) 3.5 sec | (e) 4.5 sec | (f) 5.5 sec |

Figure 102. Variation of Streamlines according to time for 973 K initial vessel temperature
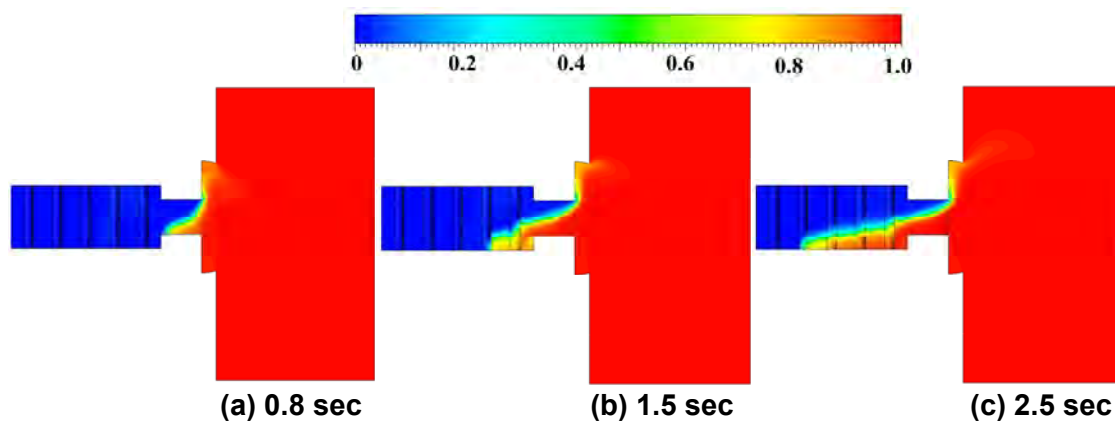
| (a) 0.8 sec | (b) 1.5 sec | (c) 2.5 sec |

Figure 103. Air mass fraction according time for 973 K initial vessel temperature

(e) 3.5 sec   **(f) 4.5 sec**   **(g) 6.5 sec**
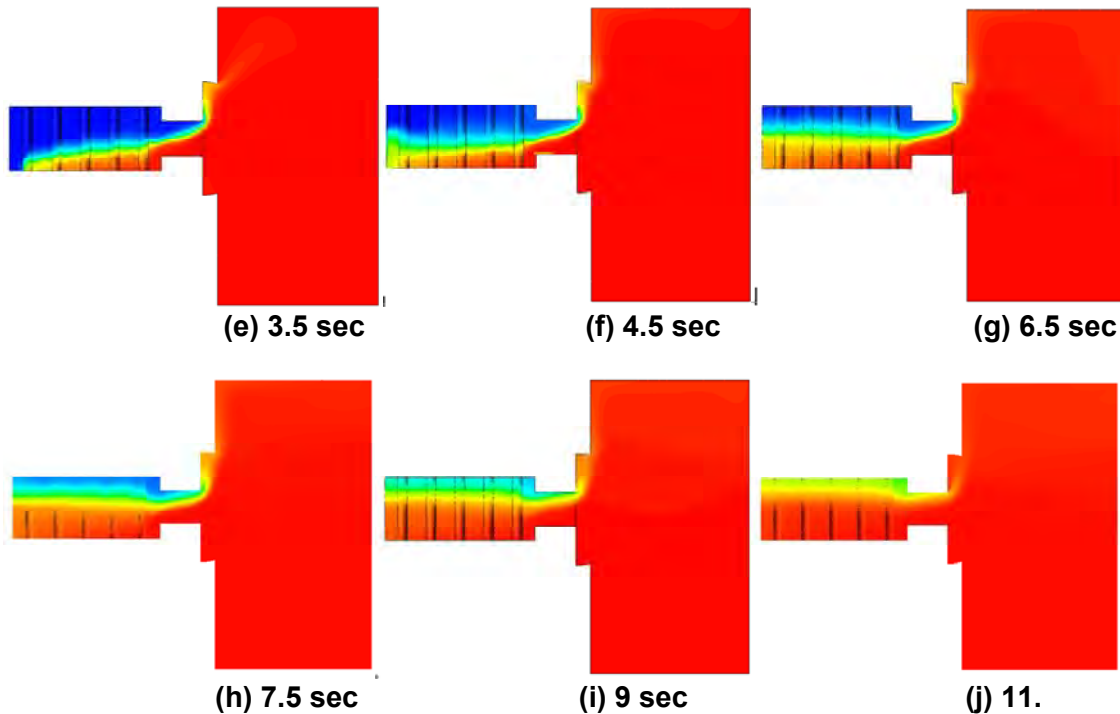
(h) 7.5 sec   **(i) 9 sec**   **(j) 11.**

Figure 103. Air mass fraction according time for 973 K initial vessel temperature (Continued)

Initiating an Experiment

One of the technical difficulties associated with running an air-ingress experiment is initiating the experiment. In this scaled-down facility, experiments are initiated with the assistance of an air pneumatic cylinder and a break plate cap. The air pneumatic cylinder with a 12" stroke can pull back the break plate cap at the same order of magnitude as the depressurization of the pressure vessel when it is pressurized to 30 psig. Below are two figures which show the air pneumatic cylinder with the break plate cap with respect to the entire setup. In the first figure (Figure 104), the break plate cap is set. In the second figure (Figure 105), the cap is pulled back into the fully-recessed position.
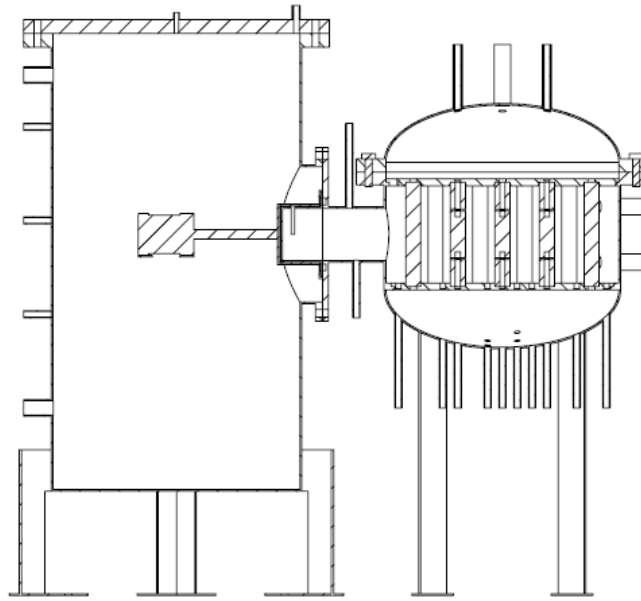
Figure 104. Scaled-down test facility with air piston stroke extended
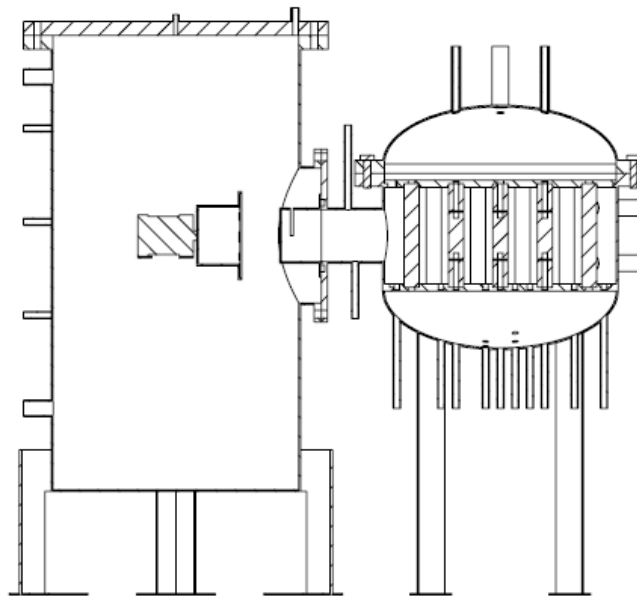
Figure 105. Scaled-down test facility with air piston stroke recessed

Update on Vessel Construction

The two pressure vessels which predominantly constitute the scaled-down test facility are nearing completion of the construction phase. To illustrate the progress that has been made in the construction of these vessels, pictures have been posted below with captions.

Figure 106. Side view of main test vessel

Figure 107. Inside of main test vessel as seen through the main side nozzle

Figure 108. View of top of the main test vessel

Figure 109. View of bottom of the main test vessel

Figure 110. Bottom surface of the bottom plate

Figure 111. Front view of containment vessel (Note: Vessel is on its side. It's designed to stand on its legs.)

Figure 112. View of inside of the containment vessel as seen from the top of the vessel

Figure 113. Back view of the containment vessel

Currently, the vessels are being assembled at OSU. In addition, other preparations are being made such as the setting up the data acquisition system; purchasing instrumentation, heaters, and wiring. The photos below show the current state of the scaled-down test facility at OSU.

Figure 114. Side View of the Scaled-down Test Facility

Figure 115. Angled view of Scaled-down Test Facility

Figure 116. Angled view of scaled-down test facility

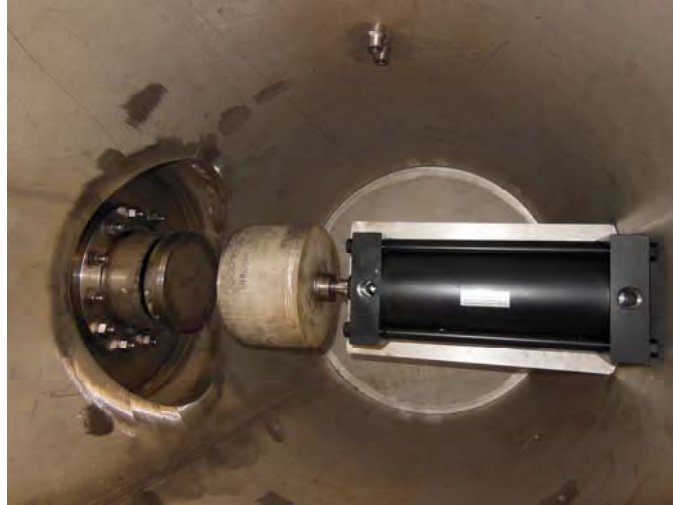Figure 117. Air piston extended in containment vessel

Figure 118. Air piston retracted from circumferential break top hat break plate

References

1. C.H. Oh, and E.S. Kim, R. Schultz, and D. Petti, " Implication of Air Ingress Induced by Density-Difference Driven Stratified Flow", ICAPP 08, 2008
2. C.H. Oh, and E.S. Kim, "Validations of CFD Code for Density-Gradient Driven Air Ingress Stratified Flow," INL/CON-10-17629, Idaho National Laboratory Report, May 2010
3. H.P. Grobelbauer, T. K. Fannelop and R. E. Britter, " The propagation of intrusion front of high density ratios", Journal of fluid Mechnics, **250**, 669 (1993)
4. J.O. Shin, S. B. Dalziel and P. F. Linden, "Gravity Current Produced by Lock Exchange", Journal of Fluid Mechanics, **521,** 1 (2004)
5. T.B. Benjamin, "Gravity Currents and Related Phenomena", Journal of Fluid Mechanics, **31**,209 (2004)
6. Thurber, M.C. and Hanson, R.K. "Simultaneous imaging of temperature and mole fraction using acetone planar laser-induced fluorescence," Experiments in Fluids, **30**, 93 (2001)
7. Thurber, M.C. Grisch. F. and Hanson, R.K. " Temperature imaging with single- and dual-wavelength acetone planar laser-induced fluorescence," Optics Letters, , **22**, 251 (1997)
8. Thurber, M.C. and Hanson, R.K. "Pressure and composition dependences of acetone laser-induced fluorescence with excitation at 248, 266, and 308 nm," Applied Physics B,**69**, 229 (1999)
9. J.N. Reyes Jr., J.T. Groome, B.G. Woods, B. Jackson and T.D. Marshall, "Scaling analysis for the high temperature Gas Reactor Test Section (GRTS)," *Nuclear Engineering and Design*, **240**, 397 (2010)
10. C.H. Oh, E.S. Kim, "Air-ingress analysis: Part 1 Theoretical approach," *Nuclear Engineering and Design*, **241**, 203 (2010)
11. C.H. Oh, H.S. Kang, E.S. Kim, "Air-ingress analysis: Part 2-Computational fluid dynamic models," *Nuclear Engineering and Design*, **241**, 213 (2010)
12. A. Banerjee and M. Andrews, "A Convection Heat Transfer Correlation for a Binary Air-Helium Mixture at Reynolds Number," *Journal of Heat Transfer*, **129**, 1494 (2007)
13. T. Maruyama, T. Kaito, S. Onose, I. Shibahara, "Change in physical properties of high density isotropic graphites irradiated in the "JOYO" fast reactor," *Journal of Nuclear Materials*, **225**, 267 (1995)
14. E.S. Kim, C.H. Oh, R. Schultz, and D. Petti, "Analysis on the Density Driven Air-Ingress Accident in VHTRs," *Transactions of the American Nuclear Society*, Vol. 99, 2008

15. World Nuclear Association, http://www.world-nuclear.org/ sym/2003/ fig-htm/labf2-h.htm
16. "GT-MHR Conceptual Design Description Report," GA-A910720, General Atomics, 1996
17. D. Arcilesi, T. Ham, X. Sun, R.N. Christensen, and C. Oh, "Density Driven Air Ingress and Hot Plenum Natural Circulation for a VHTR," *Transactions of the American Nuclear Society*, Vol. 105, ANS 2011 Winter Meeting, Washington, DC, Oct. 30 – Nov. 3, 2011, pp. 990-992
18. J.P. Abraham, E.M. Sparrow, W.J. Minkowycz, "Internal-flow Nusselt numbers for the low-Reynolds-number end of the laminar-to-turbulent transition regime," *International Journal of Heat and Mass Transfer*, **54**, 584 (2011)
19. N.E. Todreas and M.S. Kazimi (1989), "Nuclear Systems I: Thermal Hydraulic Fundamentals", Taylor &Francis
20. J.P. Holman (2001) , "Heat Transfer", McGraw-Hill
21. I.E. Idelchik, "Handbook of Hydraulic Resistance", Second Edition, Hemisphere Publishing Corporation
22. X.L. Yan, T. Takeda, T. Nishihara, K. Ohashi, and K. Kunitomi, "A study of Air Ingress and Its Prevention in HTGR," Nuclear Technology, 163, pp. 401-415, 2007
23. C.H. Oh and E.S. Kim, "Conceptual Study on Air Ingress Mitigation for VHTRs," Nuclear Engineering and Design, 250, pp. 448-464, 2012
24. http://www.atimetals.com/Documents/ati_316_tds_en.pdf, pp. 15
25. Moormann, R., "Phenomenology of Graphite Burning in Air Ingress Accidents of HTRs," *Science and Technology of Nuclear Installations*, 2011
26. Kim, E.S., No, H.C., "Experimental study on the oxidation of nuclear graphite and development of an oxidation model," *Journal of Nuclear Materials,* **349**, (2006) 182-194
27. Xiaowei, L., Jean-Charles, R., Suyuan, Y., "Effect of temperature on graphite oxidation behavior," *Nuclear Engineering and Design*, **227**, (2004) 273-280
28. Maruyama, T., Kaito, T., Onose, I., Shibahara, I., "Change in physical properties of high density isotropic graphites irradiated in the "JOYO""fast reactor," *Journal of Nuclear Materials*, **225**, (1995) 267-272
29. "Enthalpies and Heat Capacities of Stainless Steel (316), Zirconium, and Lithium at Elevated Temperatures," Oak Ridge National Laboratory – Central Research Library, ORNL - 1342

Student:

Name	Citizenship	Major	Remark
David Arcilesi	U.S.	Nuclear Engineering, Ph.D.	Passed Candidacy Exam
Tae Kyu Ham	The Republic of Korea (South Korea)	Nuclear Engineering, Ph.D.	Passed Candidacy Exam

Budget Data

			Approved Spending Plan		Actual Spending	
	From	**To**	**Quarter**	**Cumulative**	**Quarter**	**Total to Date**
Year 1: Q1	10/01/2009	12/31/2009	41,054	41,054	9,117	9,117
Year 1: Q2	1/1/2010	3/31/2010	41,054	82,108	12,605	21,722
Year 1: Q3	4/1/2010	6/30/2010	41,054	123,162	8,442	30,164
Year 1: Q4	7/1/2010	9/30/2010	41,053	164,215	13,072	43,236
Year 2: Q1	10/01/2010	12/31/2010	38,521	202,736	25,203	68,439
Year 2: Q2	1/1/2011	3/31/2011	38,521	241,257	28,793	97,232
Year 2: Q3	4/1/2011	6/30/2011	38,521	279,778	27,554	124,786
Year 2: Q4	7/1/2011	9/30/2011	38,520	318,298	36,795	161,581
Year 3: Q1	10/01/2011	12/31/2011	32,301	350,599	21,540	183,121
Year 3: Q2	1/1/2012	3/31/2012	32,301	382,900	29,973	213,094
Year 3: Q3	4/1/2012	6/30/2012	32,300	415,200	41,739	254,833
Year 3: Q4	7/1/2012	9/30/2012	32,300	447,500	42,098	296,931
Year 4: Q1	10/01/2012	12/31/2012			16,903	313,834
Year 4: Q2	1/1/2013	3/31/2013			16,157	329,991
Year 4: Q3	4/1/2013	6/30/2013			3,019	333,010
Year 4: Q4	7/1/2013	9/30/2013			114,490	447,500
		Totals	447,500	447,500		